INFORMATION TO USERS

This manuscript has been reproduced from the microfilm master. UMI films the text directly from the original or copy submitted. Thus, some thesis and dissertation copies are in typewriter face, while others may be from any type of computer printer.

The quality of this reproduction is dependent upon the quality of the copy submitted. Broken or indistinct print, colored or poor quality illustrations and photographs, print bleedthrough, substandard margins, and improper alignment can adversely affect reproduction.

In the unlikely event that the author did not send UMI a complete manuscript and there are missing pages, these will be noted. Also, if unauthorized copyright material had to be removed, a note will indicate the deletion.

Oversize materials (e.g., maps, drawings, charts) are reproduced by sectioning the original, beginning at the upper left-hand corner and continuing from left to right in equal sections with small overlaps.

SIMULATION OF CRACK PROPAGATION IN STEEL PLATE WITH STRAIN SOFTENING MODEL

by

On Bon Chan ©

A thesis

submitted to the Faculty of Graduate Studies and Research in partial fulfilment of the

requirements for the degree of Master of Science

in

Structural Engineering

Department of Civil and Environmental Engineering
Edmonton, Alberta

Spring 2005

Canada

ABSTRACT

The objective of this research program is to develop a new material model to simulate the fracture behaviour of structural steel with strain softening elements. Softening elements were used to simulate a material crack in the steel structure in this report. Load versus displacement and load versus clip-gauge displacement curves are compared between experimental and numerical results. Finite element analysis was employed to simulate the fracture behaviour of three-points bending specimens in order to achieve fracture strain for calibration. The material model successfully predicted 90% of load and stress intensity factor at fracture initiation.

The calibrated numerical model is employed on the BE 365 electric shovel boom to simulate the fracture behaviour. The strain softening model can reduce the stiffness of the boom when the softening element reaches the yield strength limit at fracture initiation. No priori is required for this analysis.

Acknowledgements

Table of Contents

List of Tables

List of Figures

List of Symbols

a, a_0	-	initial crack length
A_0	-	initial cross section area
A_f	-	cross section area at rupture
A_g	-	cross section area at maximum load
B	-	thickness of the notched beam
d_0	-	initial diameter of the specimen
d_m	-	diameter belonging to maximum load at the test
d_u	-	smallest diameter measured after the rupture of the specimen
D	-	stage of damage
D_c	-	critical damage limit
D_n	-	damage parameter
D_0	-	initial damage at very small strain
E	-	modulus of elasticity
f_t'	-	tensile strength of the material
G	-	elastic energy release rate
G_c	-	post-cracked shear modulus
G_f	-	fracture energy density
G_{uc}	-	uncracked shear modulus
h	-	slope of strain softening
K_{Ic}	-	stress intensity factor limit for Mode I
p	-	power of softening curve
$(\delta R/R)_c$	-	critical cavity radius rate
s	-	a parameter that governs the damage rate
S	-	overall cross-section area of a surface and
$\tilde{S}$	-	solid matrix area within S
U_f	-	specific fracture energy
U_m	-	area under true stress-true strain curve before strain $\ln(1+A_g)$

U_{nf}	-	area under true stress-true strain curve between strain $\ln(1+A_g)$ and $\ln(A_0/A_f)$
W	-	width of the notched beam
W_c	-	critical strain energy density
W_{dc}	-	critical damage work
W_e	-	elastic strain energy density
W_p	-	plastic strain energy density
y	-	damage strain energy release rate
Z	-	standard reduction of area of specimen = $(A_0\text{-}A_f)/A_0$
γ_s	-	specific surface energy
γ_p	-	plastic deformation energy
ε_{bf}	-	brittle fracture strain
ε_{df}	-	ductile fracture strain
ε_{eq}	-	equivalent plastic strain
ε_f	-	fracture strain
$\varepsilon_{f(max)}$	-	maximum crack opening strain
ε_{norm}	-	nominal strain
ε_p	-	plastic strain
ε_u	-	strain at peak stress
ε_y	-	strain at yield strength
e_{nn}^{ck}	-	crack opening strain
ε_{max}^{ck}	-	maximum shear crack opening strain
ε_{true}^{p}	-	true plastic strain
$\rho(e_{nn}^{ck})$	-	shear retention factor
σ	-	stress
σ_{eq}	-	equivalent stresses
σ_H	-	hydrostatic stresses
σ_m	-	maximum engineering stress
σ_{norm}	-	nominal stress

σ_{true}	-	true stress
σ_u	-	ultimate tensile stress
σ_u'	-	true stress at rupture
σ_y	-	yield stress
$\tilde{\sigma}$	-	effective stress
υ	-	Poisson's ratio
φ^*	-	potential for dissipation

List of Nomenclature

ASPEF	-	absorbed energy up to fracture
ASTM	-	American society for testing and materials
CDM	-	continuum damage mechanics
CGM	-	cavity growth model
CTOD	-	crack tip opening displacement
EPFM	-	elastic-plastic fracture mechanics
LEFM	-	linear elastic fracture mechanics
VGM	-	void growth model

1. INTRODUCTION

Ductile Fracture is a popular topic in Fracture Mechanics. Many researchers have carried out experimental or modelling studies to investigate the fracture phenomenon on different materials, such as steel, concrete, polymers and other advanced materials. From large scale battleships to tiny mechanical components in any machinery, fracture mechanics plays an essential role to predict the life expectancy and failure modes of the materials. "Professor Irwin" was named as "father" of fracture mechanics to propose the fundamental theory and his work still has great impact on recent researches. Others such as Freudenthal (1950), Kachannov (1958), Rice and Tracey (1969), Sih (1973), Gillemot (1976), and Gurson (1977) proposed different fracture criteria and constitutive models to study fracture problems.

Linear elastic fracture mechanics is a well developed subject and most of the recent works focus on elastic-plastic fracture. In linear elastic fracture mechanics, engineers can design a structure with the application of stress intensity factors corresponding to different fracture modes. However, the stress intensity factor does not represent the true fracture mode beyond the elastic region. Therefore, two parameters, CTOD and J-integral, were developed to understand and solve the non-linear fracture problems in late 70s.

For a structural analysis, the geometry and boundary conditions define the problem. On the other hand, constitutive models represent the material behaviour. These are the two components used in computational solutions for the stress, strain and energy density fields. The critical locations in the structures are identified from the computational simulation and the load or time to failure is determined from the local stress, strain and energy density histories. This report will present a material model intended to describe the cracking behaviour in steel structures.

1

1.1 Objective of the Thesis and Methodology Used in the Research

The key idea of this paper is to establish a material model to simulate the crack initiation with application of the fracture energy density and the strain-softening model. This material model is needed to predict the moment of crack initiation. When the structure reaches its peak load, a material crack initiates on the structure. This material crack is a non-physical crack, i.e., the material is not broken apart, but the structure will show unloading because of it. Material cracks are combinations of different material properties at the desired location and have the same function as a physical crack. This approach avoids remeshing and singularities and allows large deformation analysis at low computational cost.

Freudenthal (1950) concluded that energy concept plays an important role to determine the state of damage of the material. Specifically energy dissipation per unit volume is a better indicator than energy dissipation per unit area to describe the damage as it is scale independent.

The tension-softening phenomenon shows in various materials such as metals, polymers, soils, and concrete. These materials show a reduction of the load-carrying capacity in a tension test accompanied by increasing localised deformations after reaching the limit load, i.e., the load-displacement curve exhibits a descending branch. Stress-strain relations can be derived from the measured load-displacement relation as stress and strain are quotients of the original cross-section and length of the specimen, respectively. A negative slope is shown in the stress-strain diagram and is commonly called strain softening. This, of course, is a structural property and not a material property.

The entire fracture process, including crack initiation and propagation, is controlled by a fracture strain. Fracture initiation can be revealed at the peak load from the load-line displacement curve. It is known that continuous void coalescence reduces the load carrying capacity of the structure (Khoo et al., 2000). Therefore, a similar

2

unloading behaviour (strain-softening) can be a possible way to simulate the fracture of structures.

When fracture initiation is due to extremely localized strain concentrations, as a result of strain-softening, its development is simply a continuation of its initiation.

1.2 Organization of the Thesis

Chapter 2 presents a literature review on the fracture of metals. The review includes a brief discussion of fracture mechanics. In addition, various constitutive and failure models by other researchers for predicting fracture are presented.

In Chapter 3 the methodology of the proposed material model is illustrated. Two approaches – absorbed energy up to fracture (ASPEF) and strain softening model – are presented and their workability under certain situations and constraints are discussed. A material model is proposed and will be applied on analyses in next chapters.

The proposed material model is discussed in Chapter 4. The development of the model and a description of its implementation through ABAQUS are illustrated. Results from a test program carried out on a variety of models are reviewed and are compared to the numerical solutions determined by the proposed material model. Procedures for calibrating the material properties and parameters for carrying out the analyses are also presented and material parameters for calibration are achieved. Load-displacement and stress-strain curves are shown for comparison.

The application of the proposed material model to a significant structure is demonstrated in Chapter 5. A brief history of investigation on cracking issues on an electric shovel boom is presented and its structure is described. Analysis procedures and the implementation of material model are presented. Finally, comparisons are made between the test and analytical results of the shovel boom.

Chapter 6 presents a summary, conclusions and recommendation.

3

2. LITERATURE REVIEW

2.1 General

This review of the constitutive model of fracture covers experimental and theoretical studies from the past and present. The focus is primarily on the constitutive relations and fracture criteria to represent the fracture problem.

2.2 Classical Fracture Mechanics

A quantitative relation for the fracture of cracked solids was first introduced by Griffith (1921). He proposed that the equilibrium condition at which the energy released by the crack growth is equal to the energy required to create the new surface. For a plane strain state is given by

$$\sigma = \sqrt{\frac{2E\gamma_s}{\pi b}} \qquad (2.1)$$

E = modulus of elasticity,

σ = applied stress,

γ_s = specific surface energy and

b = one-half crack width.

The elastic energy release rate per crack tip is defined as

$$G = \frac{\sigma^2 \pi b}{E}. \qquad (2.2)$$

where G is the energy per unit plate thickness and per unit crack extension. However, his finding was based on brittle cracking and did not consider the plastic deformation associated with crack growth. Irwin (1947) modified Griffith's equation to include plasticity at the crack tip. Irwin introduced plasticity at the crack tip by adding an additional term γ_p and extended Equation (2.1) to:

4

$$\sigma = \sqrt{\frac{2E(\gamma_s + \gamma_p)}{\pi b}} \qquad (2.3)$$

where γ_p is the plastic deformation energy. The energy release rate G is the driving force for the crack growth. Unstable crack propagation takes place when the energy release rate exceeds the energy required for a stable crack extension. The state of cracked solids can be quantified by the energy release rate approach for engineering application.

2.3 Fracture Toughness Measurement

There are three common fracture toughness measurements for linear and non-linear fracture mechanics. These measurements are established in dealing with fracture of cracked solids: linear elastic fracture mechanics (LEFM), which uses the stress intensity factor K, elastic-plastic fracture mechanics (EPFM), which uses the J-Integral, and the crack tip opening displacement (CTOD) method. These measurements of fracture toughness are described in the following sections.

2.3.1 Stress Intensity Factor K

The stress intensity factor, K, describes the stress field in front of a crack tip, which is a function of geometry and loading. Unstable fracture occurs when the stress-intensity factor at the crack tip reaches a critical value, K_c. The stress intensity factor limit for Mode I, denoted as K_{Ic}, represents the inherent ability of a material to withstand a given stress-field intensity at the tip of a crack and to resist progressive tensile crack extension under plane-strain conditions (Rolfe et al., 1977). In LEFM for plane strain conditions, the stress intensity factor K is related to the energy release rate through

$$G = \frac{(1-\upsilon^2)K^2}{E} \qquad (2.4)$$

with $\upsilon = $ Poisson's ratio

This relationship only applies to the situation where there is little or essentially no crack tip plasticity. Mode I (tensile) fracture is the mode most often encountered in engineering applications and the stress intensity factor in this mode can be calculated refer to ASTM E1820-99a.

2.3.2 Crack tip opening Displacement (CTOD)

Crack tip opening displacement (CTOD) method, proposed by Wells in 1961, is a strain-based measurement of the opening of the crack faces to describe the fracture behaviour in the vicinity of a sharp crack. Furthermore, he showed that the concept of crack-opening displacement was analogous to the concept of critical crack extension energy release rate (G_c), and thus the CTOD values could be related to the plane-strain fracture toughness, K_{Ic}.

This method is valid for both elastic and elastic-plastic conditions. CTOD is composed of two components – elastic and plastic. The elastic part is derived from the stress intensity factor K. The plastic part is derived from the crack mouth opening displacement measured by a clip gauge. Because the CTOD test is usually conducted on materials that behave in an elastic-plastic manner, linear load-displacement records to failure are rarely obtained.

The advantage of CTOD approach is that CTOD values can be measured throughout the entire plane-strain, elastic-plastic, and fully plastic behaviour regions, whereas K_{IC} values can be measured only in the plane-strain region or approximated in the early portions of the elastic-plastic region.

2.3.3 J-Integral

J-integral is an energy-based measure, which is also separated into elastic and plastic components. As with CTOD, the elastic component is based on K, while the plastic component is derived from the plastic area under the load-displacement curve. It is

6

applicable to elastic-plastic fracture mechanics. The relationship between K_{Ic} and J_{Ic} can be expressed as:

$$J_{Ic} = \frac{(1 - \upsilon^2)K_{Ic}^2}{E}.$$

(2.5)

Also, the size requirement for the test specimen to obtain a valid J_{Ic} value is much smaller than for K_{Ic}. It is most commonly used to represent the fracture toughness in non-linear fracture mechanics. It is clearly the same as G.

2.4   Recent Research on Crack Initiation

Brittle fracture is a sudden breakage with negligible amount of permanent deformation and associated with materials that behave linearly elastic under slow and monotonic loading condition. By altering the loading rate, specimen size or temperature, the same material can behave in a very ductile manner. Ductile fracture is the consequence of nucleation, growth and coalescence of cavities (microvoids) (Dodd et al., 1987). The microvoids are present before the stress is applied. Microvoids in the virgin material grow when the material undergoes plastic deformation. When these cavities continue to grow and coincide with each other, fracture initiation occurs and further ruptures.

The stress triaxiality ratio (σ_H / σ_{eq}), where σ_H and σ_{eq} are respectively the hydrostatic and equivalent shear stresses, plays an important role in constitutive damage model especially continuum damage models. Ductility increases with increasing compressive hydrostatic stresses for most metals (Dodd et al., 1987). In some well developed models, better prediction of structural behaviour can be obtained with consideration of the state of hydrostatic stress.

In current researches on crack initiation, researchers focus on three major approaches to deal with the problems: Continuum Damage Model (CDM), Cavity Growth Model (CGM), Smeared Crack approach and Absorbed Energy up to Fracture

7

(ASPEF). The last approach is considered to be most successful because the energy density is shown constant through the analysis, and a strain energy density failure criterion is used.

2.4.1 Continuum Damage Mechanics (CDM)

Lemaitre (1985) proposed Continuum Damage Mechanics to model ductile fracture. A damage parameter, D_n, is the ratio of virgin matrix area lost over the overall cross-section area to represent the degree of damage state, which is defined by

$$D_n = \frac{S - \tilde{S}}{S},$$ (2.6)

where S is the overall cross-section area of a surface and $\tilde{S}$ is the solid matrix area within S. The value of D_n is between zero (undamaged state) and one (rupture of the element into two parts). A critical value D_c within the range shows the initiation of crack in the model. With the application of the damage parameter, the effective stress and strain are increased due to the reduction of effective area so that:

$$\tilde{\sigma} = \frac{\sigma_{nom}}{1 - D},$$ (2.7)

where σ_{nom} is the nominal stress and $\tilde{\sigma}$ is the effective stress. The material response at the marco level is thus softened by the parameter D. The constitutive equation for isotropic damage is modified as follows:

$$\varepsilon = \frac{\sigma}{(1 - D)E}$$ (2.8)

where E is the the modulus of elasticity and ε is the strain. The corresponding Ramberg-Osgood equation for strain-hardening is

$$\varepsilon^P = \left[\frac{\sigma}{(1 - D)K} \right]^M$$ (2.9)

8

where ε^p is the plastic strain and K and M are the material constants. For isotropic damage, the evolution of D is described by the potential for dissipation φ^*, which is a function of the elastic and plastic strains, the elastic and plastic rates of changes and other factors.

The critical damage state D_c is a material constant. Lemaitre (1989) discussed how continuum damage mechanics can be used to model brittle fracture, fatigue fracture, and anisotropic damage. However, the proposed continuum damage mechanics approach does not consider the volume change associated with the void growth observed in ductile fracture.

2.4.2 Cavity/ Void Growth Model (CGM/ VGM)

Rice and Tracey (1969) developed a cavity growth function as a damage criterion. Their function relates the cavity radius rate and the stress-strain field. When cavity radius rate reaches a critical value, $(\delta R/R)_c$, crack initiation is considered to occur. The void growth function used is

$$\left(\frac{\delta R}{R}\right) = \alpha \exp\left(\frac{3}{2}\frac{\sigma_H}{\sigma_{eq}}\right)\delta\varepsilon_{eq} \tag{2.10}$$

where R is the cavity radius, $\delta\varepsilon_{eq}$ is the equivalent plastic strain increment, σ_H is the hydrostatic stress, and σ_{eq} is the equivalent shear stress. A constant factor, α, was originally proposed at 0.283 and was later modified to 0.427. Marini et al. (1985) has shown that α is actually proportional to the volume fraction of second phase particles and this proportional parameter can be fitted by experiments. From his numerical results, fracture initiation starts when the damage work reaches its constant critical value, W_{dc}, for the type of steel under consideration.

The void growth model (VGM) treats the damaged material as a composite of void and matrix material. The matrix material can be treated as a damage-free material,

9

which has the same physical meaning as the virgin material in CDM. Thus, both CDM and VGM employ the same viewpoint that the macroscopic damage or void developments are due to the plastic deformation of damage-free virgin material, or matrix material, in mesoscale (damage or void-size scale).

2.4.3 Modified continuum damage model

Khoo (2000) improved Lemaitre's continuum damage model and set up a modified continuum damage model. His model considered material dilation due to void growth and hydrostatic tension stress during fracture. A simple relationship was established between the state of stress and the critical damage limit at which point fracture occurs. In linear elastic fracture mechanics, the flaws were treated as the state of damage. The state of damage for crack initiation and propagation was assumed to vary inversely with some measure of the state of stress.

Voids in his model were spherical and uniformly distributed. Similar to Lemaitre's proposal, damage is only initiated when the equivalent plastic strain ε_{eq}^{p} exceeds a certain value. The change in the damage variable D is defined as

$$dD = \left(\frac{y}{s}\right)^{n} d\varepsilon_{eq}^{p} \qquad \varepsilon_{eq}^{p} > \varepsilon_{eqc}^{p} \text{ and } \tilde{\sigma}_{ii} \geq 0, \text{ and} \qquad (2.11a)$$

$$dD = 0 \qquad \varepsilon_{eq}^{p} \leq \varepsilon_{eqc}^{p} \text{ and } \tilde{\sigma}_{ii} < 0. \qquad (2.11b)$$

A simple relationship was developed for the critical damage limit where

$$D_{c} = \frac{D_{o}}{(\sigma_{H})^{m}} \leq 0.7854 \qquad \sigma_{H} > 0 \qquad (2.12a)$$

$$D_{c} = 0.7854 \qquad \sigma_{H} \leq 0. \qquad (2.12b)$$

D_{o} is a material constants that needs to be calibrated from the numerical simulation of the material test, the value of 0.7854 is the damage level at which two adjacent voids touch each other and m is a constant. Compared to models by Lemaitre (1985) and Matic et al.

10

(1987), this modified model can achieve more accurate prediction of tension bar's deformation at fracture.

2.4.4 Absorbed Energy up to Fracture (ASPEF)

Gillemot (1976) and Czoloby (1980) proposed the absorbed strain energy density to fracture as a parameter to determine crack initiation or propagation. The total energy density has three components based on − elastic deformation, plastic deformation and crack propagation. The critical strain energy density, W_c, can be determined by the area under the true stress-true strain curve:

$$W_c = \int_0^{\varepsilon_f} \sigma_{ij} d\varepsilon_{ij}$$

(2.13)

From Gillemot's experience, a spreading crack would immediately appear after the material has absorbed the critical value of energy. Gillemot proposed a formulation of W_c:

$$W_c = \frac{\sigma_y + 2\sigma_u}{3}\left(\frac{d_0^2}{d_m^2} - 1\right) + \left(\sigma_u \frac{d_0^2}{d_m^2} + \sigma_u'\right)\ln\frac{d_m}{d_u} \qquad [\text{MJ}/\text{m}^3]$$

(2.14)

where σ_y = yield point

σ_u = ultimate tensile stress

σ_u' = true stress at rupture

d_0 = initial diameter of the specimen

d_m = diameter at maximum test load

d_u = the smallest diameter measured after the rupture of the specimen

Schindler (2001) proposed another equation to determine the fracture energy density. With the aid of critical strain energy, the effect of crack-tip constraints, finite notch root radius, and mixed mode loading on the fracture behaviour could be predicted precisely. The fracture energy density is based on the area under the true stress − true strain curve for the material (Figure 2-3):

11

$$U_f = U_m + U_{nf} \qquad\qquad (2.15a)$$

$$U_m = \frac{\sigma_m \cdot (1 + A_g) \cdot n}{n+1} \qquad\qquad (2.15b)$$

$$U_{nf} = \frac{\sigma_m}{2} \left[\frac{1 + (1 + A_g) \cdot \ln(1-Z) - n)}{\ln(1-Z) - n} \right] \qquad\qquad (2.15c)$$

where U_f = the specific fracture energy

U_m = the area under true stress-true strain curve before strain $\ln(1+A_g)$

U_{nf} = the area under true stress-true strain curve between strain $\ln(1+A_g)$ and $\ln(A_0/A_f)$

σ_m = maximum engineering stress

σ_u = true stress at rupture

A_0 = initial cross section area

A_f = cross section area at rupture

A_g = cross section area at ultimate load

n = $\ln(1+A_g)$

Z = standard reduction of area of specimen = $(A_0-A_f)/A_0$

Czoboly et al. (1980) claimed that fracture energy was more reliable than stress or strain as the fracture criterion of plastic materials. This material property could be determined simply from a static tensile test and is independent of the size of the specimen. Effect of testing conditions such as stress concentration, temperature, loading rate, etc. can be examined by this method. Moreover, specific fracture energy could be converted to fracture toughness. Thus, reliable determination of fracture mechanics parameters is possible with small specimens.

DeGiorgi et al. (1989) applied the ASPEF concept to model a compact specimen of HY-100 steel. Two- and three-dimensional nonlinear finite element analyses were conducted to simulate a cracked specimen. These models employed paired nodes at a predefined crack path location. The nodes debonded when the cracking criterion was

12

satisfied. Experimental and nonlinear two-dimensional finite element analysis agreed with each other to approximately 80% of fracture initiation load. Three-dimensional results do not improve too much compared with two-dimensional one. Classical fracture initiation toughness parameters were determined from the analysis and demonstrated that these fracture measures were not fundamental material parameters. Application of the continuum toughness concept has an advantage that no a priori assumption as to the location or mode of failure is required. The loads at which the crack-tip nodes debonded were known a priori.

Chaouadi et al. (1994) evaluated the Rice and Tracey cavity growth model and damage work model. They tested notched tensile specimens with different notch radius and found that the critical plastic strain work (critical strain energy density) was almost constant for the same material composition.

Both models could predict the crack initiation well when these models reached a relatively constant critical value. Chaouadi also claimed that damage work model had an advantage over the cavity model that damage work model was independent from the decohesion strain; therefore, damage could start whenever the plastic deformation began.

2.5 Smeared Cracking Approach

There are two commonly used crack modelling: discrete crack and smeared crack approaches. Discrete crack approach, also named cohesive crack approach, was introduced by Barenblatt (1962) and Dugdale (1960) to model different nonlinear processes located at the front of a pre-existent crack. A fictitious crack is represented as a separation of elements with introduction of cohesive forces to allow transfer of stresses through the fracture zone. When the stresses at the boundary of elements across a crack reach a critical value, the cohesive forces are eliminated and the fictitious crack is developed into a real crack and follows a predefined crack path, as shown in Figure 2-4. The original nodes A and A', which share the same coordinate, are separated after the element reaches the tensile strength limit.

The counterpart of discrete crack approach is the smeared crack approach. The concept of smeared cracking introduced by Rashid (1968) is widely used in finite element analysis of concrete cracking. According to this concept, the tensile strength of the material, f_t', limits the stress that a finite element can carry in tension. Beyond the strength limit, the tensile stress could behave in a number of different ways depending on the constitutive relation employed.

Early constitutive concrete cracking representation employed tension cut off criteria. Later the phenomenon of tension softening observed in stroke controlled tension tests of concrete specimens lead to a multitude of softening relations. Hillerborg (1983) explained the phenomenon in terms of energy of fracture density and the crack spacing. In finite element smeared crack constitutive representation, the crack spacing is analogous to mesh size; more accurately the spacing of integration points in an element. Thus, most concrete cracking models – post 1983 – employed a smeared cracking approach with some form of strain-softening in tension by rendering the stress versus strain curve mesh dependent, the results dependency on the mesh is removed - post cracking – which is a function of the fracture energy density G_f in mode I cracking.

The effect of softening is to introduce a localization of deformation, which leads to a loss of strength across the crack, as shown in Figure 2-5. Note that the smeared cracking with strain softening could lead to certain theoretical difficulties such as localization instabilities and spurious mesh sensitivity to finite element calculations. However, these difficulties can be overcome by modification of the material model with some constraints which are generally called localization limiters.

14

2.6 Summary

A variety of models dealt with the fracture problems was described in this chapter. Absorbed energy up to fracture (ASPEF) is a unique material property and can serve as the fracture criteria of materials. The smeared crack approach can provide an alternative to model a crack in terms of strain softening, which saves plenty of efforts in remeshing. Both concepts lead to the development of the proposed material model and the model can be evaluated by abovementioned fracture toughness measurements.
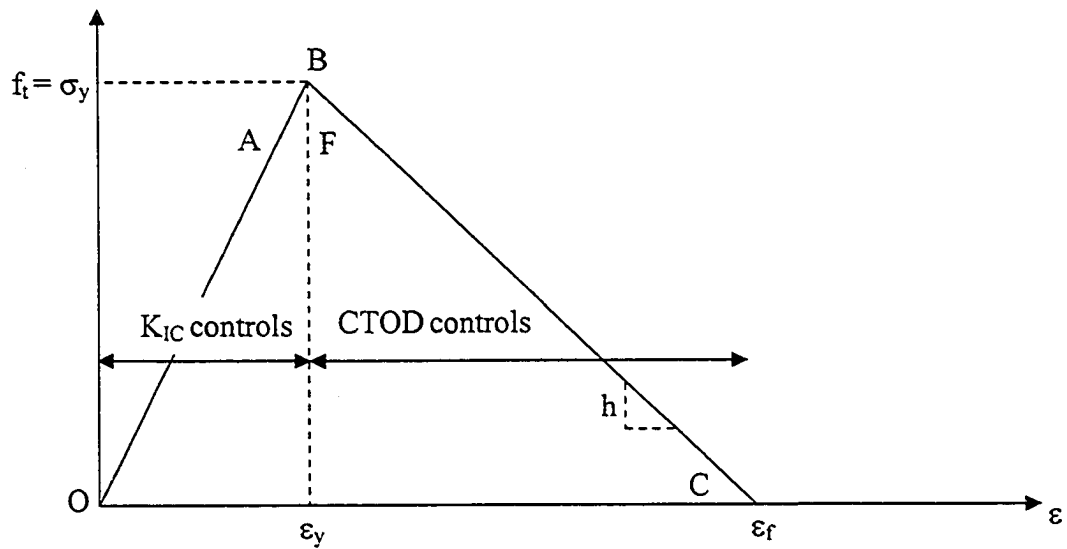
Figure 2-1 Relation between K_{IC} and CTOD Test Behaviour
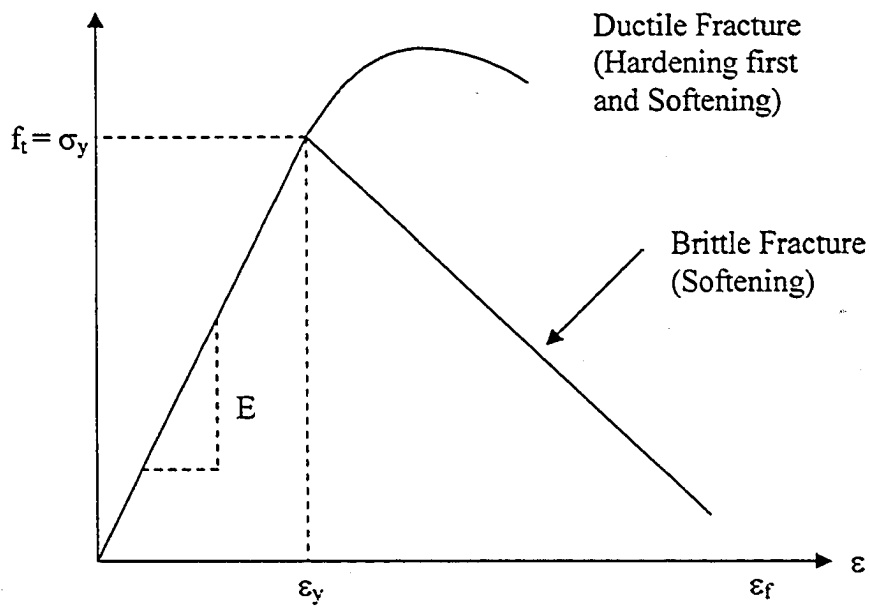
Figure 2-2 Ductile and Brittle Fracture

16
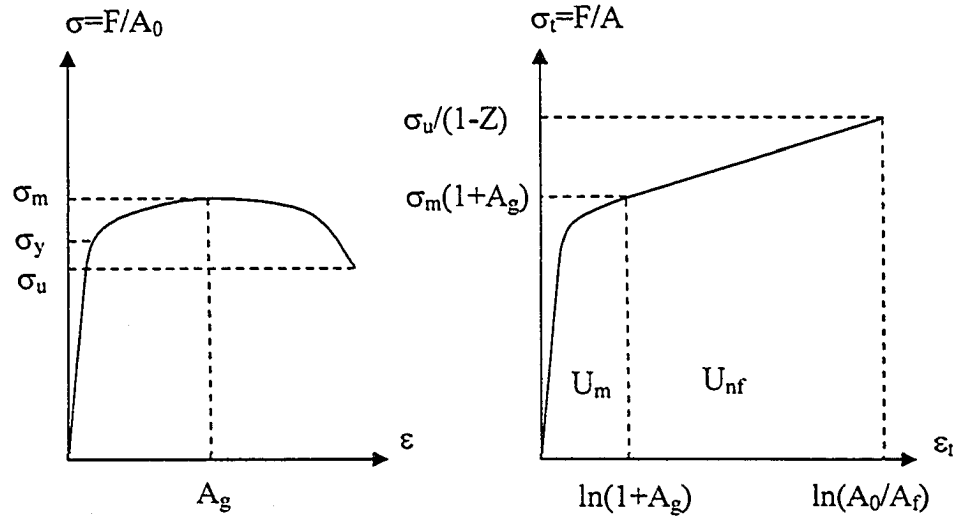
Figure 2-3 Determination of True Stress-strain Curve (right) from the Engineering Response (left) (Schindler, 2001)
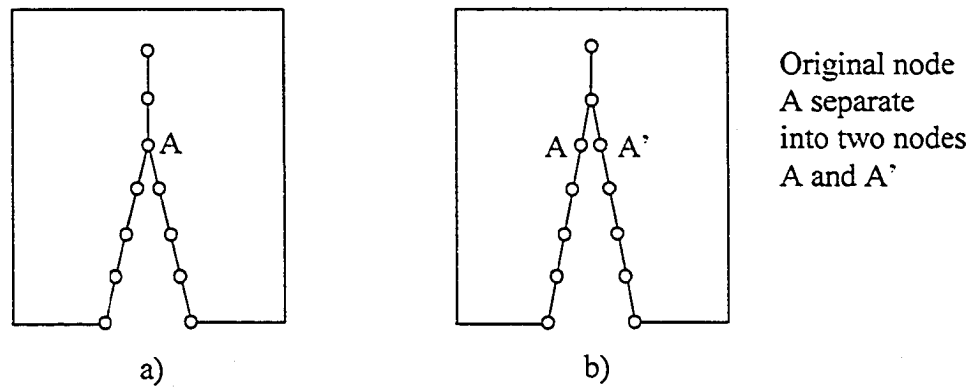
Figure 2-4 Discrete Crack Approach a) Crack Initiation at Node A; b) Crack Propagation and Separation of Node A

17
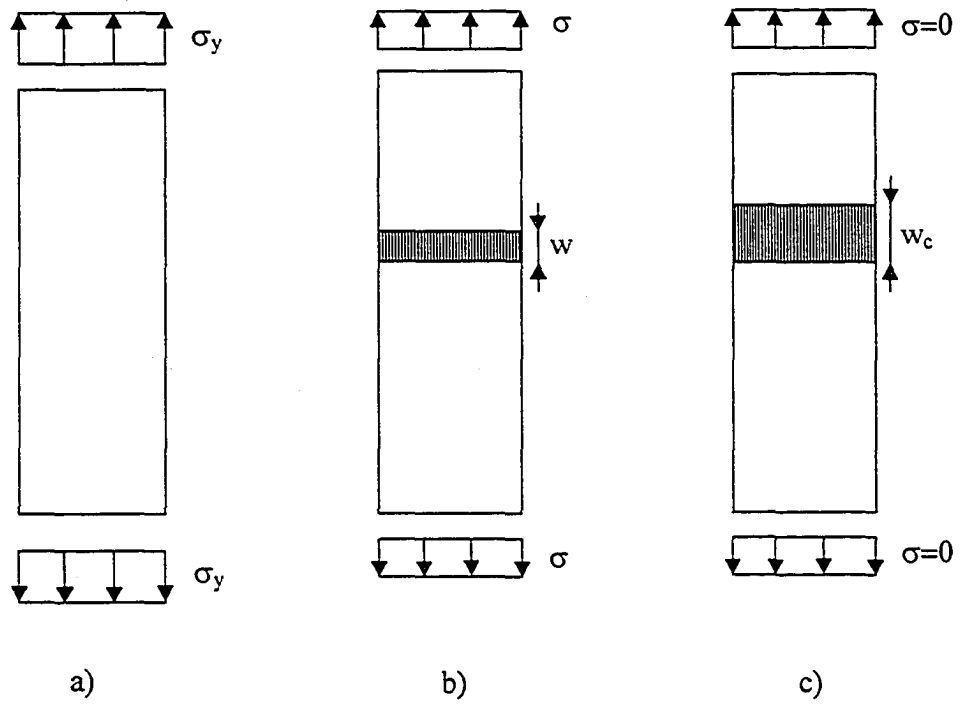
Figure 2-5 Stages of Smear Cracking Approach a) No Damage; b) Strain Localization; and c) Separation

3. PROPOSED NUMERICAL MODEL

In the previous chapter, a number of constitutive material models for representing cracking behaviour of steel plate were presented. The numerical model used in this thesis is based on the concept of fracture energy density of specific type of steel and strain-softening constitutive model. In the previous chapter, the absorbed energy up to fracture (ASPEF) approach is found to be a good fracture criterion for steel plate. On the other hand, strain softening constitutive relation is commonly used in modelling of cracking concrete structures employing the concepts of fracture mechanics but in a smeared cracking representation. However, this approach is not adopted in modelling cracks in steel structures because of high ductility. In this chapter, numerical cracking simulation in a smeared crack formulation is proposed with the applications of the ASPEF and strain softening model.

3.1 Basis of the Proposed Material Model

The finite element program ABAQUS (2002), version 6.3, was used to analyze and simulate the proposed material model response. Fracture energy density approach and strain-softening model mentioned before were adopted and modified to the proposed material model. A cracking model in ABAQUS was selected and modified for the numerical analysis to represent the material cracks in the steel plate structures in a smeared manner. Physical cracks (debonding between element and element) do not exist in the model but the steel plate structure is forced to lose its capacity and stiffness at the potential crack locations using strain softening elements. These strain softening elements function as smeared material cracks when the load at fracture initiation is reached. Thus, the stress picture around the crack area is modified, promoting a stress concentration at the crack tip zone and helping drive the crack function.

The concept is based on the smeared cracking approach but is applied on cracking analysis of steel structures. The stress level in every softening element is limited by the yield strength of the material, σ_y. After the yield strength is reached, the stress in this

19

finite element must decrease. In this proposed model, the stress decrement is assumed to be linear. The schematic description of the material model is shown graphically in Figure 3-4. Two assumptions were made for this model:

1) Strain softening only occurs in localized tension at locations of flaws.
2) Strain hardening can occur in either compression or tension in the absence of flaws.

It is important that the material around the edge of the plastic zone undergoes strain-hardening to act as a constraint on flow. However, hardening behaviour does not last for a large increment of plastic strain due to the unloading of the adjacent strain softening portion. A material crack, which has the same influence (unloading) of a physical crack, is then simulated by the combination of these material properties.

This finite element analysis can simulate the load versus displacement and load versus clip-gauge displacement curves by controlling two parameters yield strength, σ_y, and fracture strain, ε_f, in the model. Fracture strain is the ultimate strain when the stress level of an element vanishes, which means that the element loses its capacity completely. These two curves are used to determine the fracture toughness in elastic and elastic-plastic stages. For elastic stage, mode I stress intensity factor can be determined from the former curve. CTOD can be determined from the latter curve and provide better and more accurate prediction than that determined by linear fracture mechanics during the crack propagation stage.

Rashid (1968) introduced a powerful approach Smeared Cracking to finite element analysis of concrete cracking. According to this concept, the stress in a finite element is limited by the tensile strength of the material, f_t', as shown in Figure 3-3. In the early development of this approach, the stress was assumed to drop suddenly to zero. Nevertheless, more realistic results obtained from direct tension tests under stoke control showed that in a given gauge length a crack process zone with a limited length (crack width) forms (Shah et al., 1986). As the direct tension test progresses, the length of the

20

crack process zone increases, while the nominal stress in the specimen decreases. The average strain over the full gauge length appears to increase with a decrease in the stress giving the illusion of a strain softening stress strain relation (Hillerborg, 1983).

Hillerborg (1983) has shown that for concrete crack type I, the area under the stress-displacement response from a direct tension test is the energy of fracture per unit area for concrete. Subsequent works by innumerable researches in finite element analysis of concrete cracking have combined the concept of smeared cracking representation with the concepts of energy of fracture and strain softening. However, the gauge length was taken to be the distance between integration points in a single element, since in a smeared crack representation, cracks are only detected at the integration points.

The strain softening model is suitable to simulate the brittle fracture of material under slow and monotonic loading condition. This kind of failure can be governed by the loading rate, specimen size and temperature. Before a brittle fracture failure can occur, a combination of tensile stress, low temperature, thick material or rapid change of stress must be present. The yield stress is usually considered as the tensile strength. It is because when the yield stress has been reached, the deformations make the structure unacceptable.

Even though the smeared cracking concept has been widely applied, this concept is a mesh sensitive approach (Hillerborg, 1983). Thus, the degree of softening and size of the softening portion are two important issues in this model. The width of strain-softening portion is critical to the result. If the width of the strain-softening region is sufficiently small, unloading may not be taken into consideration during the analysis. Softening elements in different mesh sizes are used for conducting the analyses. If the mesh size is large especially around the notch tip, the structure appears to be stiffer than expected. Since the effect of mesh size is not the issue of investigation, no further work on effect of mesh size is conducted. However, it is found that the mesh size 0.5 mm × 0.5 mm is fair enough for numerical simulation of fracture toughness tests to provide a good prediction of fracture initiation.

21

The degree of the softening can be quantified by the strain-softening slope. In this model, softening is assumed to be linear. Thus, as shown in Figure 3-3, the strain-softening slope can be expressed as follow:

$$h = -\frac{\sigma_y}{\varepsilon_f - \varepsilon_y} \tag{3.1}$$

$$\sigma = \begin{cases} E\varepsilon & \text{for } \varepsilon \leq \varepsilon_y \\ \sigma_y + h(\varepsilon_f - \varepsilon) & \text{for } \varepsilon > \varepsilon_y \end{cases} \tag{3.2}$$

where h = the slope of strain softening

σ_y = the yield stress

ε_y = the yield strain

ε_f = the fracture strain

The slope of strain-softening for all softening elements is assumed to be the same but may be a function of element size to obtain better accuracy.

As mentioned earlier, the proposed material model is governed by the yield strength and the fracture strain. The yield strength can be simply obtained from tension coupon tests. The fracture strain, ε_f, can be obtained either by a) absorbed energy up to fracture (ASPEF) or b) trial and error method. The two approaches are presented and discussed following.

3.2   Absorbed Energy up to Fracture Approach (ASPEF)

Absorbed Energy up to Fracture approach (ASPEF), which is also named fracture energy density here, is considered as an essential parameter to describe the fracture behaviour of steel. Fracture energy density per unit volume at fracture can be determined by the integrated area under the true stress versus true strain curve. It consists of two components; elastic and plastic parts:

22

$$W_c = \int_0^{\varepsilon_f} \sigma_{ij} d\varepsilon_{ij} \tag{3.3}$$

$$W_c = W_e + W_p. \qquad\qquad W_e \ll W_p \tag{3.4}$$

where W_e = elastic strain energy density

W_p = plastic strain energy density

Fracture initiation takes place when the material reaches the critical fracture energy density. Fracture energy density is a fundamental material property and is almost constant for ductile metals because the material density varies only slightly, even over large deformation (DeGiorgi et al., 1989). Therefore, it is considered as an indicator of fracture initiation in the material.

The stress-strain profiles determined by tension coupon tests are greatly influenced by the temperature. These tests are usually conducted at room temperature. It is well known that the fracture energy density is dependent on test temperature. The fracture energy density achieved under high temperature is usually larger than that under low temperature, as shown in Figure 3-1. However, the energy density remains constant even the material has different mechanical treatment. Prior to the simulation of the crack initiation and propagation, it is necessary to consider the temperature effect on the fracture energy density in order to achieve the reasonable failure modes – ductile or brittle fracture.

Once the critical fracture energy density is reached, the stress versus strain curve will be converted to a softening stress versus strain curve, as shown in Figure 3-2. Softening curves will behave different according to the expected failure mode. For brittle fracture, a linear softening curve is used. It is very similar to the strain softening model discussed in the next section. For ductile fracture, a bilinear softening curve is assumed. The softening curve for ductile case is controlled by five parameters – yield strength,

23

yield strain, peak stress and strain at the peak stress, and the fracture strain. The peak stress for brittle fracture in the model is yield strength. Thus, the curve for brittle case is controlled by yield stress and fracture strain. Fracture strains for both scenarios can be determined in the following providing that the critical fracture energy density is achieved:

$$\varepsilon_{bf} = 2W_c / \sigma_y \qquad \text{for brittle fracture} \qquad (3.5)$$

$$\varepsilon_{df} = (2W_c + \varepsilon_u\sigma_u - \varepsilon_u\sigma_y - \varepsilon_y\sigma_y)/ \sigma_y \qquad \text{for ductile fracture} \qquad (3.6)$$

where ε_{bf} = the brittle fracture strain

ε_{df} = the ductile fracture strain

W_c = the fracture energy density

σ_y = the yield strength

σ_u = the peak stress

ε_y = the strain at yield strength

ε_u = the strain at peak stress

Gillemot (1976) showed that fracture energy densities for tension and compression cases were different. The energy density in compression is higher than that for tension. However, the energy density was greatly reduced when the specimen was loaded under compression followed by tension. Therefore, the loading histories of the material can influence the value of fracture energy density for specific material.

Softening elements have to be paired with the hardening elements on the structure. For instance, softening elements are applied on a thin zone (the flawed zone) to promote fracture initiation. Hardening elements have to be adjacent to the softening elements, as shown in Figure 3-5. The situation is similar to the crack initiation at the notch tip, as shown in Figure 3-6. In Figure 3-6, two nodes share the same coordinate. The material at the notch tip reaches the critical fracture energy density, W_c, and is broken apart. The material around the notch tip (hardening element) hardens. At the same time, the crack breaks the bonding of material and the tip opening becomes larger. The proposed material model replaces the crack in Figure 3-6b with softening elements in Figure 3-7b. These

24

elements soften the material at the notch tip without debonding of material and serve the same function as a crack does, i.e., reduction of loading capacities.

In material failure analysis, a strain energy density failure criterion is used to describe the material failure initiation. In failure propagation analyses (elastic-plastic fracture mechanics), the fracture toughness with an energy balance method is adopted.

3.3   Analysis Procedures

In the first phase, a finite element model was developed to predict the behaviour of a notched beam under slow and monotonic loading. In the second phase of the investigation, the finite element model was used to predict the crack initiation and propagation on a complex structure; the boom of a major shovel used for the sand excavation. This chapter focuses on the development of the constitutive model used in the first phase of the investigation. The validation of this model will be presented and discussed further in next chapter. The basic steps involved in the first phase of the investigation were as follow:

1)   A linear elastic mesh study of a notch beam was performed to determine the level of mesh refinement required to ensure convergence.

2)   An isotropic hardening mesh study of a notch beam was performed.

3)   An isotropic hardening mesh study of a notch beam including strain-softening elements was performed.

The cracking model for concrete in ABAQUS/Explicit code (Hibbitt et al., 2002) was employed to conduct all analysis in this chapter. The post failure behaviour of direct tension across cracks was modelled with the brittle cracking (*BRITTLE CRACKING) option. This option required the percentage of peak stress and corresponding direct cracking strain as input in tabular form, starting with the peak stress and zero plastic strain. ABAQUS/Explicit offers a shear retention model in which the postcracked shear modulus, G_c, is defined as a function of the opening strain across the crack. Shear

25

retention can be defined in a power law form by using the TYPE=POWER LAW parameter with the *BRITTLE SHEAR option:

$$G_c = \rho(e_{nn}^{ck})G_{uc},$$ (3.7a)

$$\rho(e_{nn}^{ck}) = \left(1 - \frac{e_{nn}^{ck}}{e_{max}^{ck}}\right)^p,$$ (3.7b)

where G_{uc} = the uncracked shear modulus

G_c = the post-cracked shear modulus

$\rho(e_{nn}^{ck})$ = the shear retention factor

p = the power of the softening curve

e_{max}^{ck} = the maximum shear crack opening strain

Since linear strain softening is assumed in this model, the power of the softening curve, p, equals to 1.0.

The parameter ε_{nn}^{ck} used in the numerical analysis was calibrated either by a) Absorbed Energy up to Fracture approach (ASPEF) or b) trial and error method to reproduce the load versus displacement and load versus clip-gauge displacement response observed from the literature. It is recommended to achieve the fracture strain with the ASPEF method first. If the numerical simulation with the fracture strain achieved by ASPEF approach is not reasonable compared with the experimental results, the fracture strain has to be obtained from the trial and error approach. The parameter ε_{max}^{ck}, which influences the strain softening slope, must be obtained by trial and error. The range is generally between 0.03 and 0.1. In this study, these two parameters were adjusted so that two conditions were satisfied. The first condition is that the predicted load at fracture initiation be within 10% of the measured load at fracture initiation. The second condition is that the tolerance between the predicted strain at fracture initiation and experimental strain were also within the expected tolerance.

3.4   Preliminary Analysis

3.4.1   Linear Elastic Mesh Study

The main purpose of the linear elastic mesh study was to determine the level of mesh refinement required to ensure convergence. Geometry, material constitutive relationship and boundary conditions are three essential aspects of any finite element analysis. The notched beam was discretized using four-node bilinear, plane stress elements with reduced integration and hourglass control.

3.4.2   Boundary Conditions

The boundary conditions of the model were described as shown in Figure 3-8. The black nodes with arrows show the degrees of freedom at. The translational degree of freedom at the top of the midspan, was restrained in the horizontal direction so that the model can maintain symmetry. Two nodes, a distance R from the edge of the beam, were restrained in the vertical direction to represent roller supports. The nominal distance between the roller supports was four times the width, W. A reference node, which moves in the vertical direction with linear velocity, is connected to several nodes on the top surface with rigid beam elements in order to apply load at the midspan of the model. The magnitude of the applied load on the model is determined by the reaction force (RF2) at two roller supports. The finite element mesh is more refined in the region surrounding the crack tip than in the rest of the model.

3.4.3   Procedure

Before running the analysis, the program required initial time, total time, and minimum and maximum time increments. All of them, except the total time, are not important to the explicit analysis. The total time is decided by the expected vertical displacement of the midspan in this analysis. A linear amplitude curve of velocity was used. The total time can be calculated and equals to two times the expected displacement

27

over the assigned velocity. The velocity of 1 mm/ s was used in this and the following analyses. Thus, the total time was taken as two times the expected displacement.

3.4.4 Target Stage

For this portion of the analysis, the nonlinear material model proposed above *was* taken into consideration so that the behaviour of the notched beam could be investigated beyond the elastic range. The entire plate is divided into three different material regions – linear-elastic (LE), isotropic hardening (IH) and softening (S). Isotropic strain hardening material models are developed based on the results of tension coupon tests. The mean static yield stress, true stress, σ_{true}, and corresponding plastic strain, ε^p_{true}, are required as input by ABAQUS. Therefore, engineering stress and strain values, tension coupon test data, must be converted using the equations:

$$\sigma_{true} = \sigma_{norm}(1 + \varepsilon_{norm}),$$ (3.8a)

$$\varepsilon^p_{true} = \ln(1 + \varepsilon_{norm}) - \left(\frac{\sigma_{true}}{E}\right)$$ (3.8b)

where σ_{norm} and ε_{norm} are the engineering stress and strain, respectively.

In the isotropic hardening region, the elements yield and harden. The hardening curve is based on tension coupon test results. To model the stress-strain response of steel after ultimate in the material model, a material stiffness (i.e., slope of the true stress versus true strain curve) after ultimate was assumed. A tangent line is approximately fitted to the stress-strain curve in the post yield region and is extrapolated to 100% strain. For uniaxial material test, the true stress versus true strain curve developed from the specimen load-displacement response may not be a precise description of the material constitutive responses for large deformations leading to fracture. However, large deformation is not expected in this analysis, and the curve adopted for this analysis is considered to be adequate.

28

In the softening region, the stresses decrease linearly to low values (close to zero) after reaching the yield strength. The modulus of elasticity, Poisson's ratio, the fracture strain, ε_f, and the maximum shear fracture strain, ε_{max}^{ck}, are critical material parameters to control the degree of softening. A bilinear softening curve is adopted. The stresses of elements drop to 5% of yield strength at the fracture strain, ε_f, and drop further to 1% at 100% strain. Fracture strain was considered as the first crack opening strain after zero plastic strain and the maximum crack opening strain, as shown in Figure 3-9.

The inelastic analysis used the same geometry of the notched beam used as the elastic analysis described in section 3.4.1. The boundary conditions described in section 3.4.2 before were applied on the model to maintain the symmetry. Magnitude of loading and deflection can be obtained from the reaction force at the supports and the displacement between the notch opening nodes, respectively. The explicit analysis procedure used the same velocity control function employed in the elastic preliminary analysis.

3.4.5 Effect of Element Types

Generally, the two-dimensional inelastic analysis presented in the former section was sufficient to provide a good prediction. The following section investigates if the effect of element types and three-dimensional analysis can improve the numerical prediction.

Generally, the study is aimed towards plate structures. All preliminary work employed the continuum element CPS4R. Element CPS4R is 4-node bilinear plane stress element with a reduced integration and hourglass control. Element S4R is a four node finite strain shell element involving contact, plasticity and large deformations. Same geometrical layout, material model and boundary conditions are interchanged for both shell and continuum elements. The shell element can model components of out-of-plane shear stress while the two-dimensional continuum cannot. However, ABAQUS does not include this component in the constitutive relationship, thus there is no difference

29

between the two elements. Analysis presented out in chapters 4 and 5 rely on the S4R shell element.

3.5 Summary

The methodology of the absorbed energy to fracture (ASPEF), strain-softening and the proposed material model were presented and explained. In the first phase of investigation, the proposed analysis was carried out to model fracture toughness tests. A non-linear material model based on tension coupon tests data was created to represent the elastic-plastic-hardening and softening behaviour of structural steel. Calibration is required for the two critical parameters - fracture strain and maximum shear crack opening strain – for the material model in order to predict the fracture behaviour precisely. The analytical procedures were illustrated in detail. After achieving a convergence of the mesh model using linear elastic analysis, the inelastic analysis could be executed. Moreover, effects of element type and three dimensional versus two dimensional analysis are investigated. The numerical results will be presented and discussed in the next chapter.
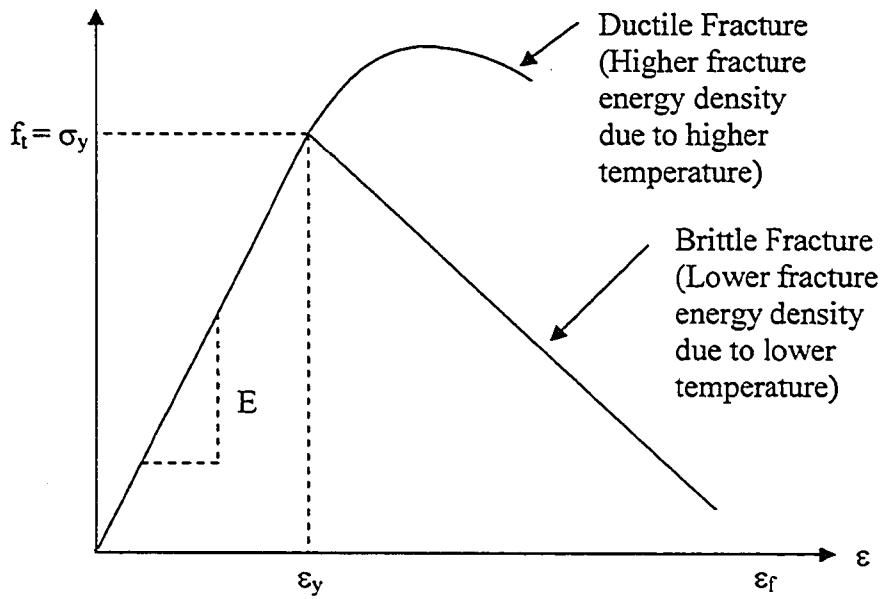
Figure 3-1 Temperature Effect on Fracture Energy Density
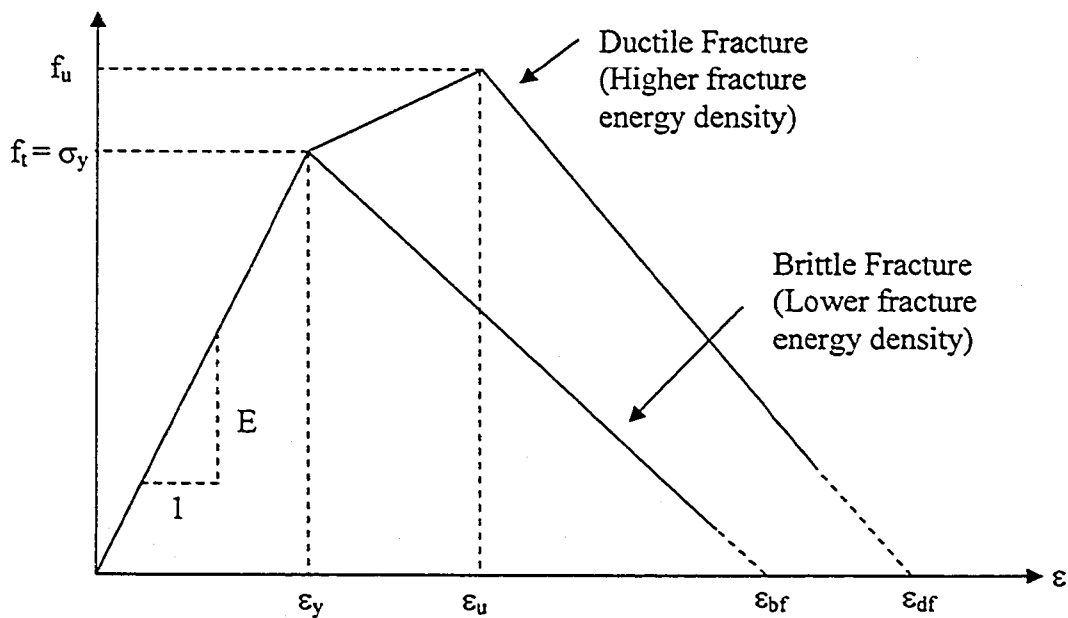
Figure 3-2 Proposed Softening Curve for Fracture Energy Density Approach

31
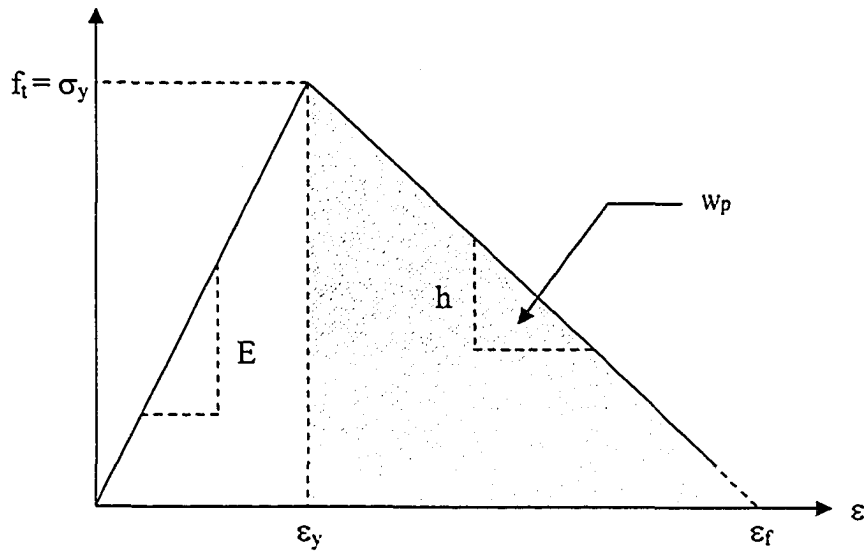
Figure 3-3 Strain-softening Modulus
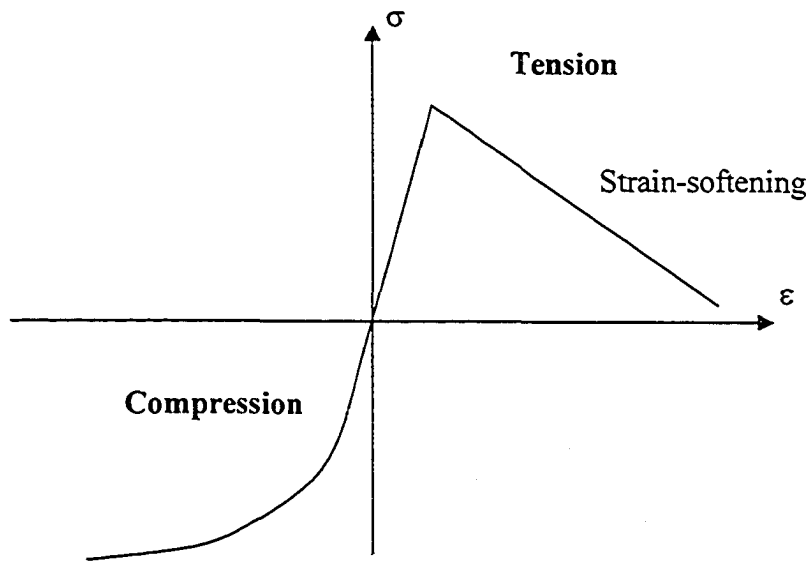
Figure 3-4 Schematic Description of Material Behaviour at Crack Location

32

Strain-hardening
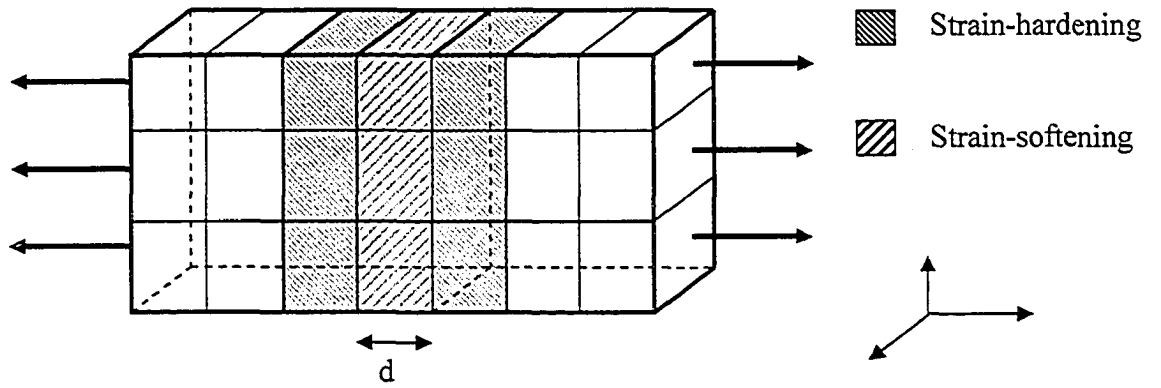
Strain-softening

Figure 3-5 Model of Thin Steel Sheet

a) Before Crack Initiation   b) After Crack Initiation
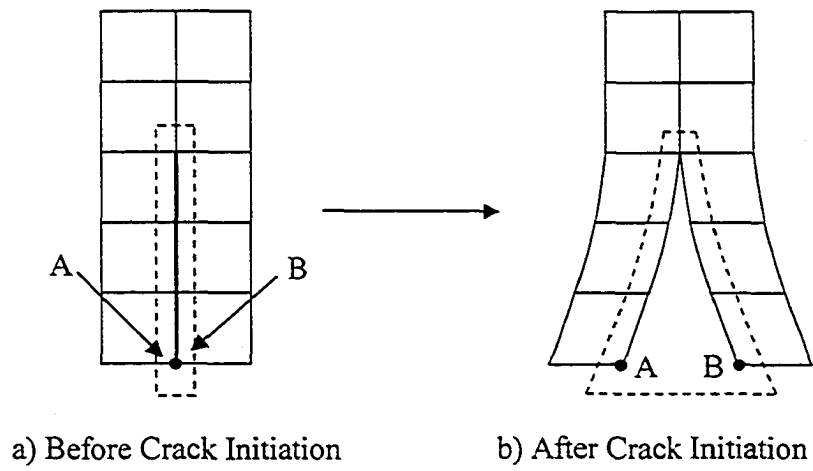
Figure 3-6 Material at the Notch Tip

a) Before Crack Initiation   b) After Crack Initiation
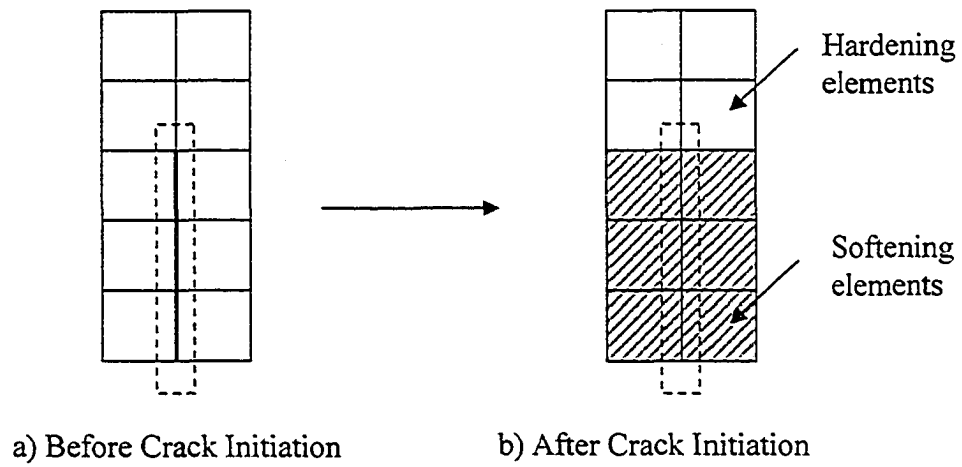
Figure 3-7 Material at the Notch Tip in terms of Softening Elements
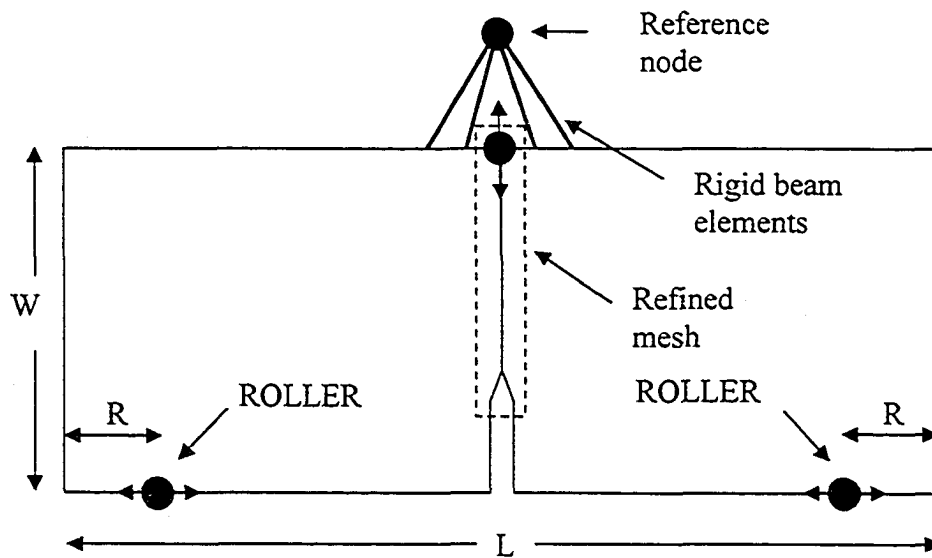
Figure 3-8 Boundary Condition for Numerical Analysis on Notched Beam

34
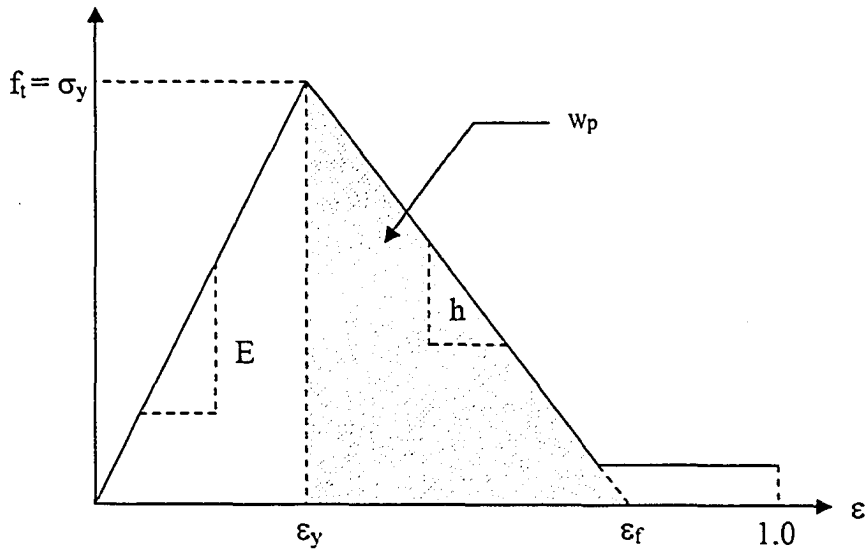
Figure 3-9 Strain-softening Model for ABAQUS/Explicit

35

4. APPLICATION TO TEST RESULTS

It is necessary to verify the proposed model against the results from the literature. Therefore, several fracture toughness tests were chosen to verify the numerical model. Several specimens were used to obtain consistent result to reduce the inaccuracy. Load versus load line displacement and load versus clip-gauge displacement plots are also presented. A discussion of the test results and comparison with the numerical model is presented later in this chapter.

4.1 Coupon Test Specimens

All tension coupons and fracture toughness tests were conducted at the University of Alberta (Yin et al., 2004) as part of a study, which investigates crack propagation in the boom of a major shovel used in tarsand extraction by Syncrude Canada. Each tension coupon was 500 mm long, 40 mm wide and 38 mm thick, as shown in Figure 4-1. All coupons were made of 350W steel. Data collected for the study include the applied load (MTS load reading), the deflection, and the clip-gauge displacement. Furthermore, the constitutive model requires the true stress versus true strain curve of the material in order to carry out the numerical analysis. In a tension coupon test, necking and strain localization start after the maximum load is reached. Thus, a profile of the true stress versus true plastic strain can be calculated directly from the engineering stress versus engineering strain curve before reaching the maximum load. The engineering stress versus engineering strain curve of the material can be measured using an extensometer during the test, up to the point of maximum load.

4.2 Material Properties

Tension coupon tests were conducted to obtain the modulus of elasticity and yield strength. Three coupons were fabricated and tested according to ASTM Standard A370 (ASTM, 1997). Engineering stresses were calculated as the MTS load reading divided by the initial area of the coupons, while engineering strains were measured by an

extensometer with a 50 mm gauge length. Static readings were taken on the yield plateau, along the hardening curve, and at the ultimate tensile strength.

A summary of test results is shown in Table 4-1. The elastic modulus was determined by applying linear regression analysis to the elastic portion of the test data. Two to four static readings were taken along the yield plateau to determine the mean of these values as the static yield stress. The static ultimate stress is taken from the static reading of stress near the ultimate load. The strain at the end of the linear elastic portion of the stress versus strain curve and that at fracture are shown as the Yield Strain and Failure Strain, respectively.

4.3 Test Setup and Instrumentation of Three-Points Bending

The three-point bend test specimen was used to determine the fracture toughness of steel, as shown in Figure 4-2. A total of four bending test specimens were tested. Dimension of the specimen are $B = 38.1$ mm, $W = 76.2$ mm and $a/W = 0.5$; where B, W and a are the specimen thickness, width and crack length, respectively. All specimens are 350W steel. The specimens were preloaded cyclically until initiation of a fatigue crack from a machined notch. The initial crack length was about 4 mm.

Tests were carried out using a MTS universal testing machine. All stroke, extensometer, and loading readings were recorded with a data acquisition system. During the test, the load versus deflection response was constantly plotted. Stroke control was employed in all the tests. The specimens were tested to fracture. In order to minimize the influence of the loading rate on the result, the specimens were loaded at an appropriate rate and static stress values were obtained at regular intervals.

Two roller supports were about 20 mm apart. Clip-gauge was instrumented at the notch to read the clip-gauge displacement. The distance between supports has to satisfy the requirement in ASTM E-1820. One out of four specimens was loaded at room temperature while the rest of them at -50°C. A sealed box with dry ice covered the

37

specimens to maintain the low temperature. The MTS machine applied the monotonic loading until the specimens fractured.

4.4 Test Results

Since the applied loading was stopped at regular intervals to allow the specimens to achieve equilibrium, there was some noise in the loading curves. Therefore, some static readings in the load versus displacement curve were filtered out to generate a clear monotonic loading curve without affecting the results.

Specimen 1, which was tested at room temperature, did not break apart before the clip gauge ran out of range. Also, load versus displacement curve from Test 2 did not show very reasonable and stable loading curve. Limited information on fracture failure was provided from these experiments. Therefore, results of Test 1 and 2 were considered as failure results. Possible causes of failure would be discussed later in this chapter.

Load versus displacement and load versus clip-gauge displacement plots for Tests 3 and 4 are presented in Figure 4-3 and Figure 4-4, respectively. Both specimens failed in a brittle manner with little ductility after reaching the peak load, as shown in Figure 4-3. In Test 3, fracture initiation occurred at 76 kN and the specimen started to unload. The specimen fractured when the load reading reached almost zero. The final displacement (deflection) is about 1.2 mm.

In Test 4, the fracture initiation occurred at 85 kN, which was higher than that in Test 3. The final displacement (deflection) was about 1.4 mm. Since the results from Tests 3 and 4 were slightly different, it was conservative to take the data from Test 3 as a basis of comparison with the numerical results.

4.5 Numerical Model

Geometry, material model and boundary conditions were required for the numerical simulation. The geometry of the notched beam model was drafted with software AUTOCAD, and half the model is shown in Figure 4-5. Full model was used during the analysis. The model employed 2D continuum elements CPS4R. Elements near midspan were finer than those away from the midspan. Transitional elements were used to reduce the number of fine elements. Figure 4-6 shows a enlargement of the notch area. The largest size of element was 10 mm by 10 mm while the smallest was 0.5 mm by 0.5 mm.

The mean modulus of elasticity and Poisson's ratio used as input for the linear elastic material model were 186300 MPa and 0.3, respectively, based on the results of tension coupon tests (see Table 4-1). A tangent line was approximately fitted to the stress-strain curve in the plastic region and was extrapolated to 100% strain to achieve corresponding true stress of 1114.6 MPa, as shown in Figure 4-7. The true stress-true strain profiles for hardening and softening elements are shown in Table 4-2 and Table 4-3, respectively.

The boundary conditions of the model were described in Chapter 3. The distance R from the edge of beam was 20 mm (twice the element width). The reference node would move at a velocity of 1 mm/s downward. The expected displacement (deflection) was 2 mm and the total time for the analysis was 4 seconds.

4.6 Two-dimensional and Three-dimensional Simulation

This analysis was carried out to investigate the improvement on prediction of global response by a three-dimensional analysis. An analysis was conducted to predict the load-displacement solution curve and compared with the two-dimensional one. Continuum elements (ABAQUS Element Type C3D8R) were 8-node linear brick element with a reduced integration and hourglass control. The same geometry from the two-dimensional analysis was employed but the thickness of beam was divided into several

39

equal layers. Nevertheless, more layers would slow down the analysis. Thus, three layers are considered to be reliable for the analysis after several trial and errors.

The three-dimensional analysis could simulate the out-of-plane movement while the two-dimensional one neglected it. Out-of-plane displacements and their effects on the stress and strain state within the three-points bending specimen could not be precisely modelled by a two-dimensional analysis. Since the three-dimensional analysis had high computation cost, it would not be used in further analysis unless the improvements were significant.

The analysis results predict closely the structure stiffness and load at fracture initiation, even though improvements were still required. The stress contours for the beam near the notch tip are shown in Figure 4-8. The load-displacement curves and load-clip-gauge displacement simulated by two- and three-dimensional analyses are shown in Figure 4-9 and Figure 4-11, respectively. The accuracy of these numerical curves can be verified by laboratory data in the same figures. It is seen that the numerical curve obtained from two-dimensional analysis shows a stiffer behaviour than that by three-dimensional one.

The fracture strain was determined by the absorbed energy up to fracture (ASPEF) approach at first. The fracture energy density obtained from the true stress-true strain curve is 69.8 MJ/mm^3 and the calculated fracture strain is 0.374 according to equation (3.5). However, the load versus displacement and load versus clip-gauge displacement curves generated by the material model with this value of fracture strain did not agree with the experimental results. The calculated fracture strain was much higher than the required fracture strain. Thus, the ASPEF approach could not successfully determine the required fracture strain for calibration.

Therefore, the crack opening strain e_{nn}^{ck} and maximum shear crack opening strain ε_{max}^{ck} used in the numerical analysis were calibrated by trial and error to reproduce the load versus displacement and load versus clip-gauge displacement. A good prediction

40

could be achieved by two-dimensional analysis with crack opening strain $e_{nn}^{ck} = 0.170$ but $e_{nn}^{ck} = 0.190$ for the three-dimensional analysis, as shown in Figure 4-10. The maximum shear crack opening strain was 0.05 for both cases. The comparison is shown in Figure 4-11. It was interesting that the ultimate strain was 0.160 from the true stress versus true strain curve of tension coupon tests, which was close to the predicted fracture strain. The ultimate strain obtained from tension coupon tests could probably be used as a fracture strain for the analysis. The loading curve from the three-dimensional analysis produced a better fit to the experimental result. However, it was more time consuming in computation. The result showed little improvement with three-dimensional analysis in load-line displacement curve.

The stress-strain relationships for strain-softening and hardening elements at the moment of fracture initiation are shown in Figure 4-12 and Figure 4-13, respectively. E designates an Element and 24XX stands for the element number in the figures. These elements were located along the vertical line from the notch tip. Softening elements show an increment of strain with decreasing stress. As shown in Figure 4-12, all 24XX elements reached the yield strength limit and then showed a reduction in stress. The strain in element 2434 was about 0.11 at the moment of fracture initiation. Elements in Figure 4-13 were hardening elements but they unloaded elastically because the adjacent softening elements developed a smeared crack. The hardening elements reached the yield strength limit and started to harden at first before unloading.

The effect of temperature and loading rate were not considered in the material model presented here. As mentioned in the literature review chapter, the temperature could have great impact on the load-displacement response when the structure fails in a brittle manner at low temperature. Therefore, the material model presented was only suitable for limited range of fracture circumstance. On the other hand, the loading rate could have impact on the response of fracture as well. Therefore, it is necessary to develop and to modify the material model with the consideration of both effects in the future.

41

4.7 Prediction of Fracture Initiation

Precise prediction of fracture initiation was essential for verification of the proposed material model. The notched beam was subjected to monotonically increasing load until fracture initiation. Fracture initiation occurs when the strain energy density at the crack tip reaches the local material toughness determined from the tensile specimens as described earlier.

Result from two-dimensional model analysis gave conservative result for fracture initiation, as shown through Table 4-4, Table 4-5 and Table 4-6. Fracture initiation by fracture toughness tests occurred at 78.69 kN, while it occurred at 75.95 kN by the finite element model. The error between experiment and FEM was 3.5%. Clip-gauge displacement during fracture initiation by toughness test and FEM were 0.445 mm and 0.462 mm, respectively. The error between these two was 3.7%.

It was interesting that the material model could predict well the experimental result after fracture initiation. The energy density versus displacement from the notch tip curves for both softening and hardening elements are shown in Figure 4-14. The energy density of softening elements remained constant when the element was away from the notch tip. At the same time, the energy density of hardening elements increased when the hardening element was away from the notch tip. The energy density of elements at the notch tip reached its critical value and fracture initiation took place. As mentioned in Chapter 2, the energy density approach was more proper to predict the elastic-plastic behaviour.

Stress versus displacement from the tip at different time was plotted in Figure 4-15. Each curve represents the stress state at specific time which refers to specific loading during the analysis. The peak stress is close to the yield strength and shifts away from the tip when the analysis continues, which indicates the crack propagation.

42

4.8   Prediction of Fracture Toughness

Fracture toughness serves an alternative to verify the material model. Classical fracture parameters are calculated from the load-displacement records and fracture initiation values predicted from the finite element simulation using the concepts discussed previously. Predicted fracture parameters, for instance, stress intensity factor and CTOD, were compared with the experimental values.

The experimental and numerical mode I stress intensity factor at fracture initiation, K_I, was determined in accordance with ASTM E-1820 specification. The predicted K_I value is 613.1 MPa-m$^{1/2}$ while the experimental value of K_I is 635.2 MPa-m$^{1/2}$. The analytical and experimental values differ by 3.6 %. It was considered to be acceptable.

The crack-tip opening displacement was determined in accordance with ASTM E-1820 as well. The predicted CTOD value is 0.737 mm while the experimental value of CTOD is 0.668 mm. The analytical and experimental values differ by 9%, which is somewhat high. As mentioned before, no priori opening was required for this analysis. Therefore, no bond separation between elements occurred. These elements at the notch tip experienced softening or probably little hardening before softening. No or little plastic deformation took place in these softening elements. Thus, there is doubt that the deformation at the notch tip experienced by these elements was not the same as that caused by the initial crack and further propagation.

The linear strain softening model might not accurately simulate the fracture behaviour of the notch beams. Bilinear or curvilinear strain softening models possibly predicted better behaviour after fracture initiation. However, for the simplification, the linear model was employed. The results of stress intensity factor in mode I could be well predicted within elastic and early elastic-plastic stages. Consequently, it was revealed that the material model could successfully predict the fracture response at and shortly after fracture initiation.

43

4.9 Summary

The proposed model employed softening elements to simulate the material crack. Behaviours of these elements were controlled by the yield strength, fracture strain and maximum shear crack opening strain. The fracture strain was critical to the prediction by the model. In order to achieve the value of fracture strain, the resulting load versus displacement and load versus clip-gauge displacement were compared to the experimental data. The fracture strain could be determined by two approaches – ASPEF or trial and error. The fracture strain could not be determined successfully by the first approach and thus the second approach was used. Moreover, fracture toughness could be determined according to the ASTM E-1820 from the load-displacement curve generated by the finite element program. Once a suitable fracture strain value was achieved within specified tolerance, the calibration of the material model was finalized.

One of the advantages with this analysis is the elimination of the remeshing process of elements. However, the deformation of the structure due to cracking could not be well predicted because no debonding between elements occurred. Also, the effect of temperature and loading rate were not considered in this model. The load versus displacement response of notched beam could not yet be predicted accurately in all respects by finite element analysis.

However, the finite element model provided a significant advancement toward the development of a cracking model for notched beams over those that have been described in the literature. Overall, the numerical simulation successfully fulfilled the purpose of this chapter with this material model and it could be applied on further analysis of electric shovel boom in the next chapter.

Table 4-1 Summary of Tension Coupon Tests

Test Number	Dimensions (mm)	Material Properties				Load	
		Modulus of Elasticity (MPa)	Yield Strength (MPa)	Ultimate Strength (MPa)	Rupture Strain	Ultimate Tensile Load (kN)	Rupture Load (kN)
1	500×40×38	183800	368.7	498	0.1544	766	725
2	500×40×38	183600	371.8	499	0.1620	764	760
3	500×40×38	191500	378.0	498	0.1717	764	745
Mean		186300	372.8	499			

Table 4-2 Material properties used in ABAQUS analysis (Isotropic Hardening)

Elasticity of Modulus, E = 186300 MPa	Poisson Ratio, υ = 0.3
True Stress (MPa)	True Strain
372.8	0.00000
418.6	0.02575
445.1	0.03369
473.0	0.04442
508.0	0.06259
541.4	0.09103
578.9	0.14117
1114.6	1.00000

Table 4-3 Material Properties used in ABAQUS analysis (Strain-softening)

Elasticity of Modulus, E = 186300 MPa	Poisson Ratio, υ = 0.3
Remaining Direct Stress	Direct Cracking Strain
1.00	0.000
0.05	0.170
0.01	1.000

Table 4-4 Test and Predicted Results on Maximum Capacity

Test	Measured Capacity (kN)	Finite Element Model	Ultimate Capacity (kN)	Test/ Predicted Ratio
3	78.69	CPS4R (2-D)	75.95	1.04
		S4R (2-D)	75.79	1.04
4	84.84		75.95	1.13

Table 4-5 Test and Predicted Results on Clip-gauge Displacement

Test	Measured Clip-gauge Displacement (mm)	Finite Element Model	Predicted Clip-gauge Displacement (mm)	Test/ Predicted Ratio
3	0.462	CPS4R (2-D)	0.445	1.04
		S4R (2-D)	0.444	1.04
4	0.500		0.445	1.12

46

Table 4-6 Test and Predicted Results on Displacement (Deflection)

Test	Displacement (Defelction) (mm)	Finite Element Model	Predicted Displacement (Defelction) (mm)	Test/ Predicted Ratio
3	0.684	CPS4R (2-D)	0.755	0.91
		S4R (2-D)	0.755	0.91
4	0.610		0.755	0.81

Table 4-7 Test and Predicted Results on Stress Intensity Factor K

Test	Measured Stress Intensity Factor K	Finite Element Model	Predicted Stress Intensity Factor K	Test/ Predicted Ratio
3	635.2	CPS4R (2-D)	613.1	1.04
		S4R (2-D)	613.1	1.04
4	684.8		613.1	1.12

Table 4-8 Test and Predicted Results on CTOD

Test	Measured CTOD	Finite Element Model	Predicted CTOD	Test/ Predicted Ratio
3	0.668	CPS4R (2-D)	0.737	0.91
		S4R (2-D)	0.737	0.91
4	0.597		0.737	0.81

47

Not to scale
(dimension in mm)
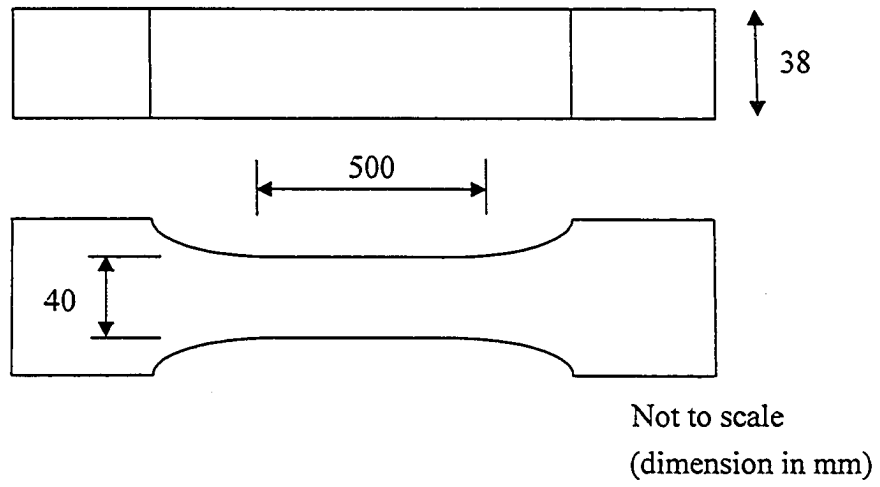
Figure 4-1 Dimension of Tension Coupons
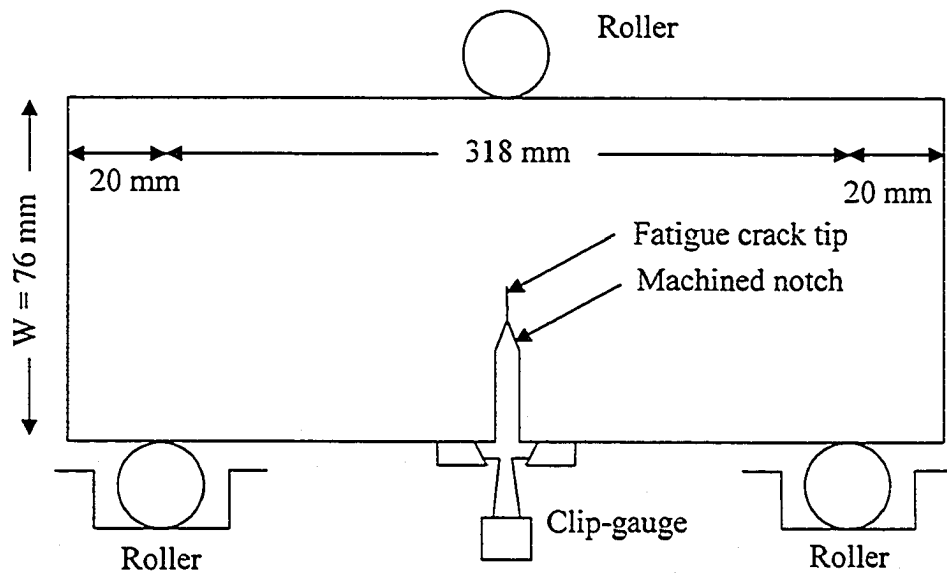
Figure 4-2 Test Setup for Three-point Bending Test
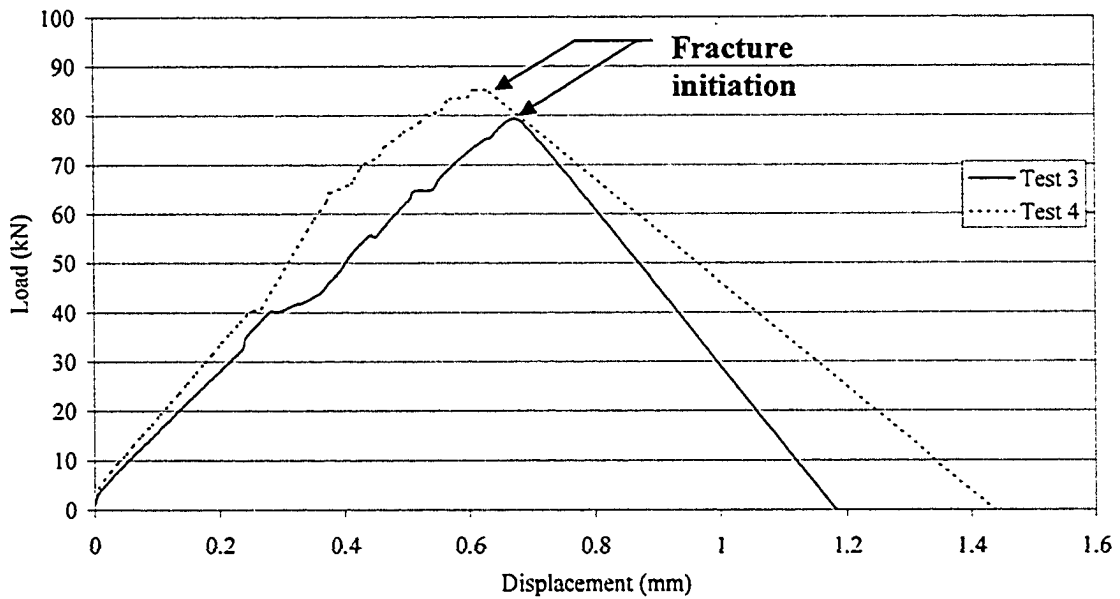
Figure 4-3 Load versus Displacement (Tests 3 and 4) for Fracture Toughness Tests 3 and 4 of Yin et al. (2004)
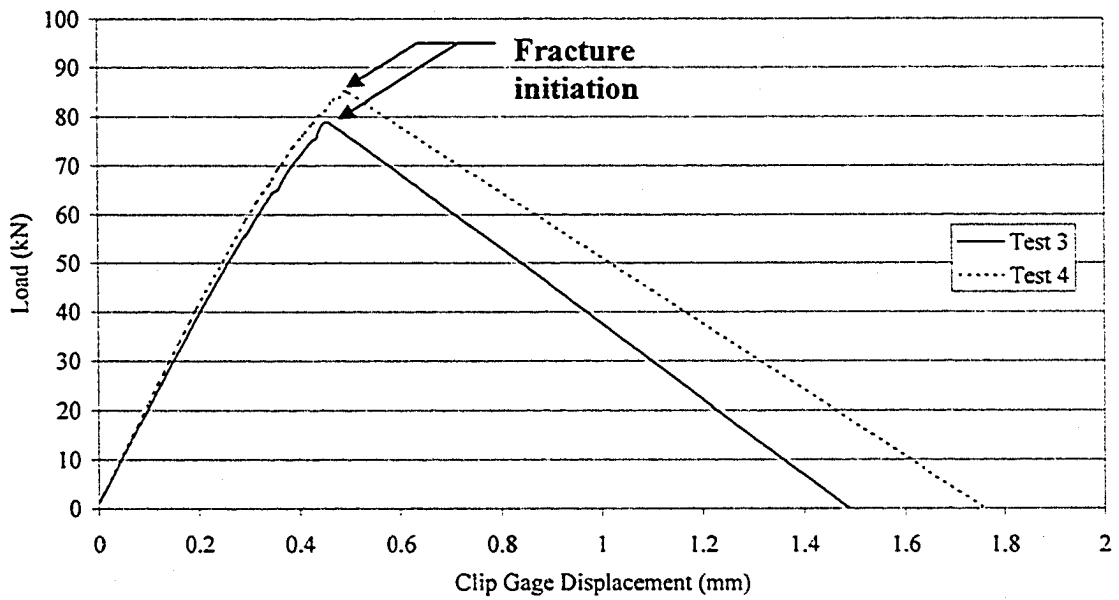
Figure 4-4 Load versus Clip-gauge Displacement (Tests 3 and 4) for Fracture Toughness Tests 3 and 4 of Yin et al. (2004)

49
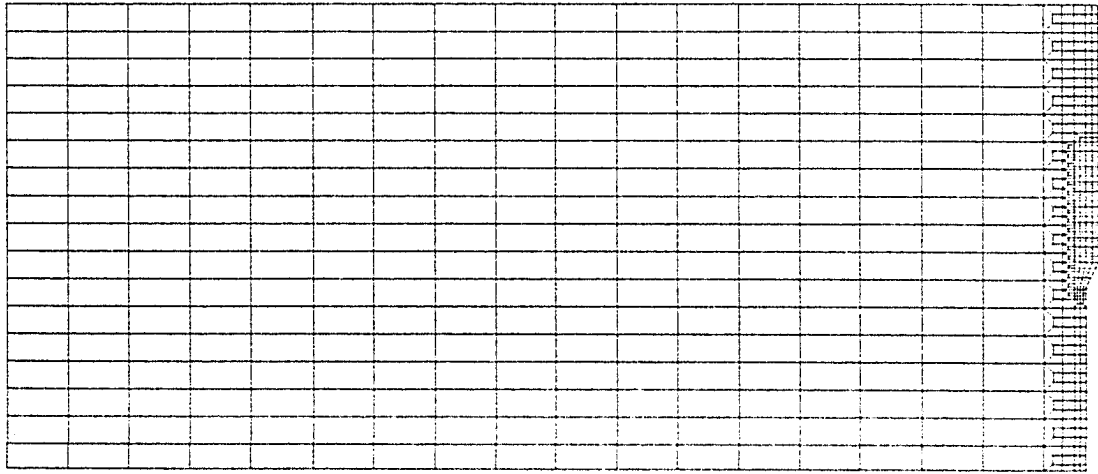
Figure 4-5 Notched Beam Geometry (Half portion)
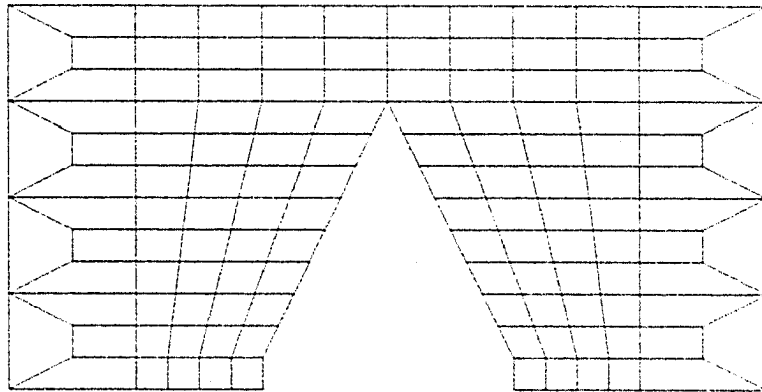
Figure 4-6 Mesh Refinement around the Notch Tip

50
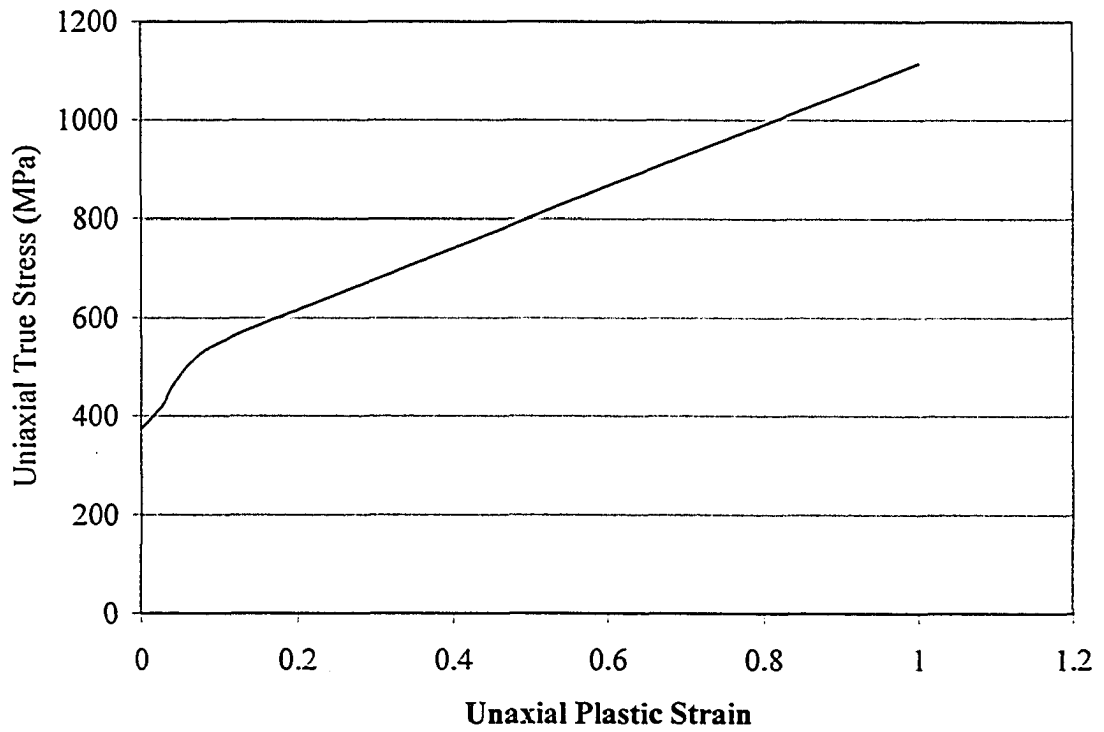
Figure 4-7 True Stress versus Plastic Strain Curve Used in the Model

51
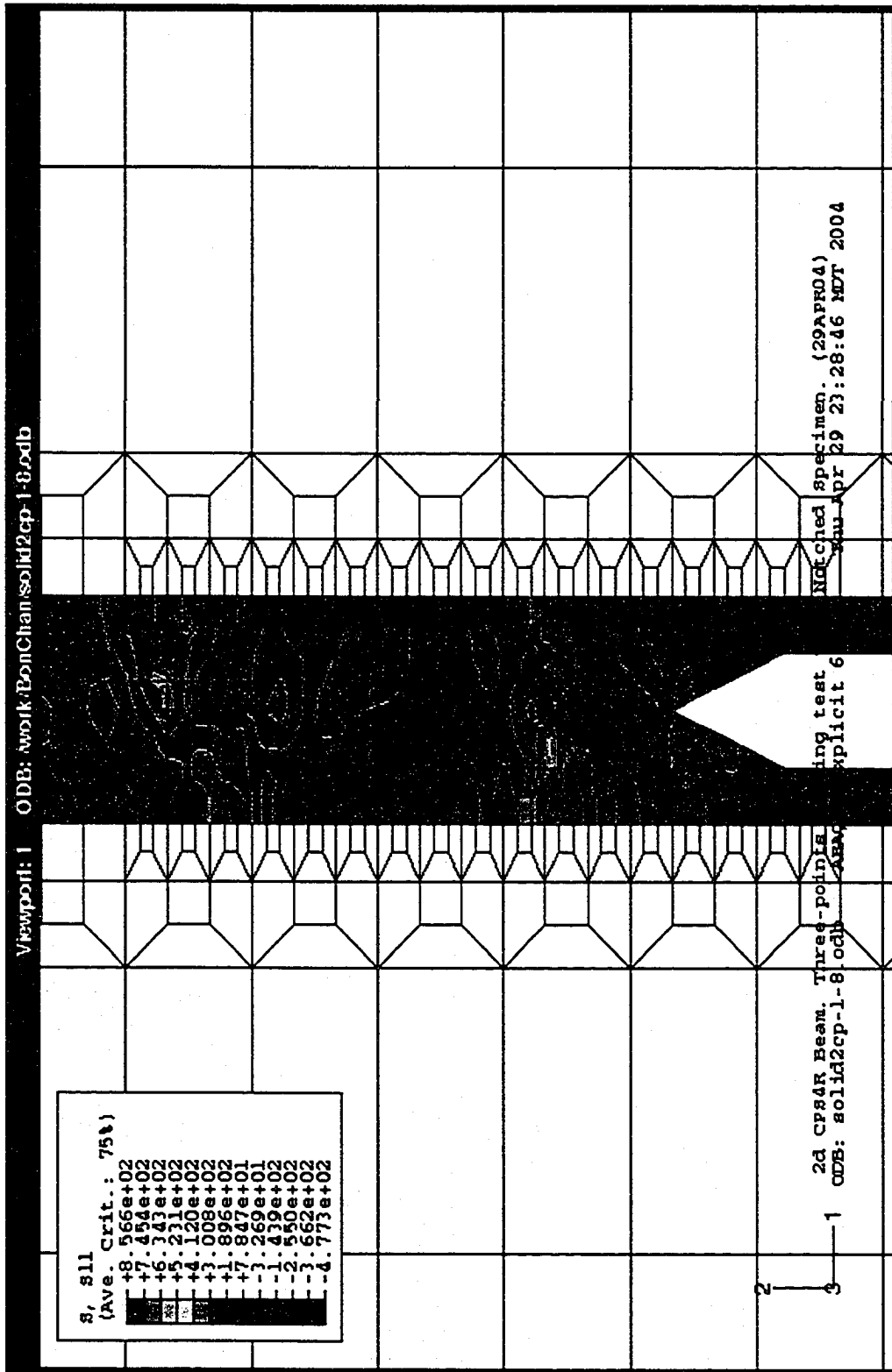
Figure 4-8 Stress Contour around the Notch Tip

52
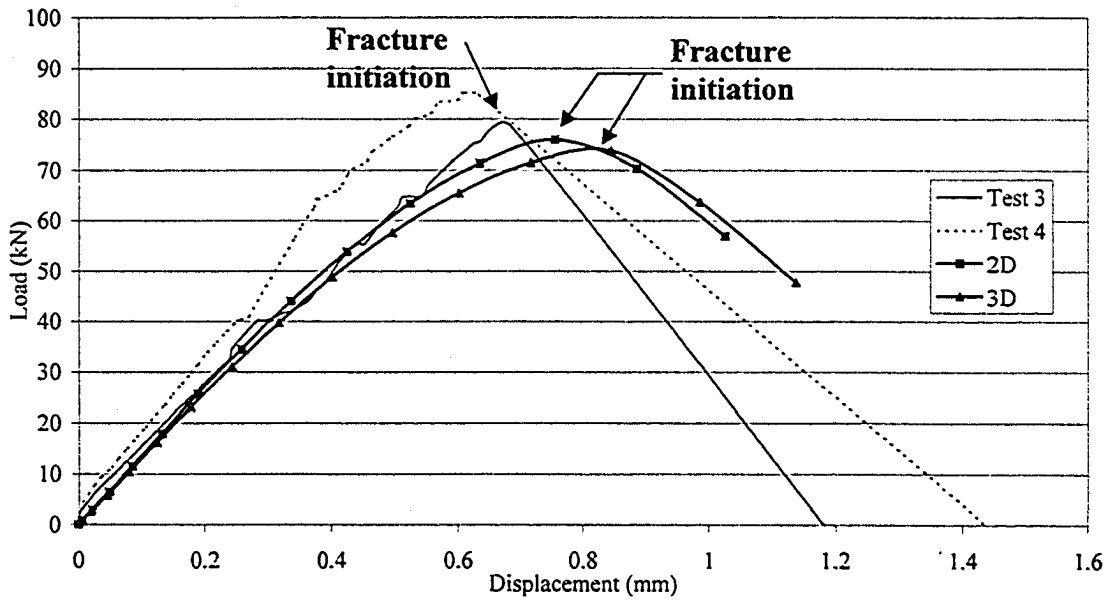
Figure 4-9 Comparison of Load versus Displacement Curve
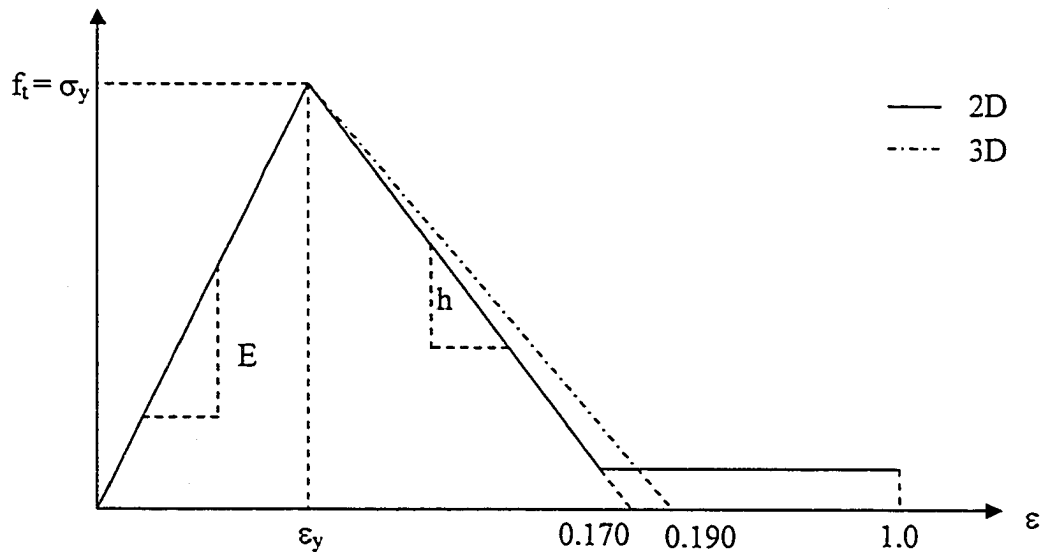
Figure 4-10 Strain-softening Model with Fracture Strain for 2D and 3D Analysis

53
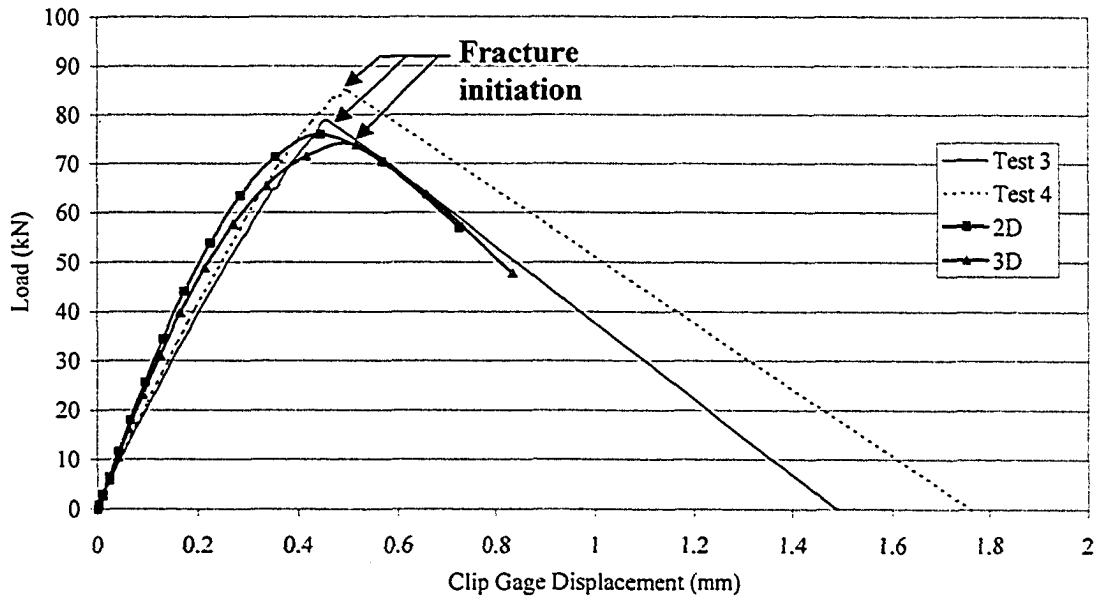
Figure 4-11 Comparison of Load versus clip-gauge displacement curve
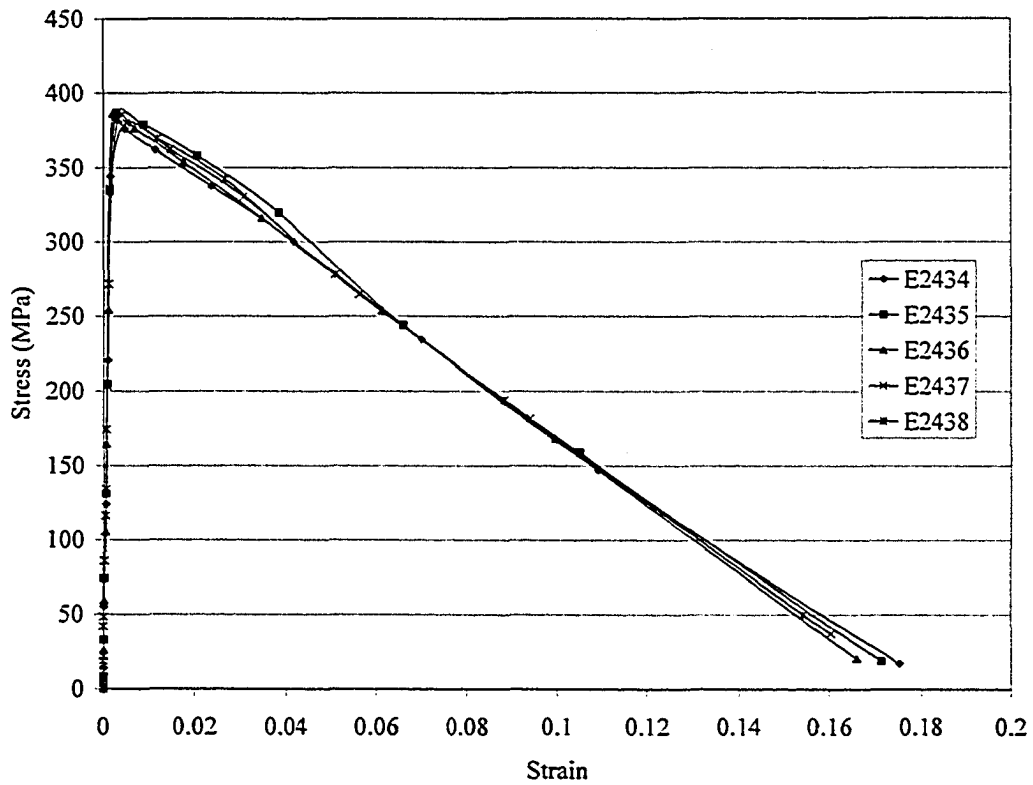
Figure 4-12 Stress-strain Curve of Softening Elements
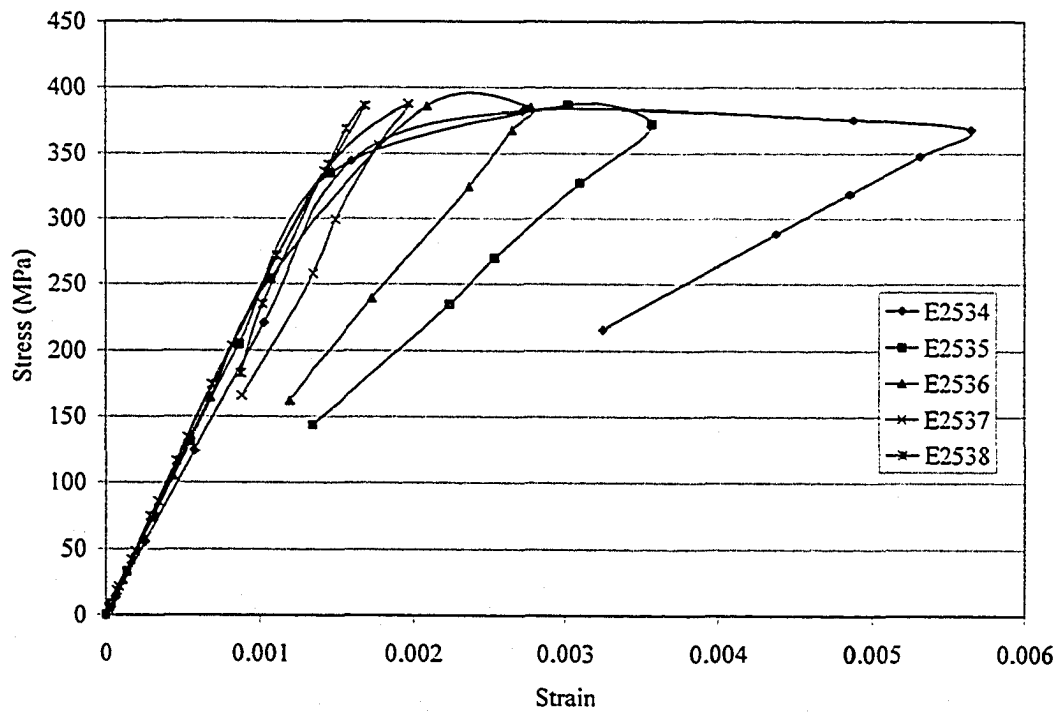
Figure 4-13 Stress-strain Curve of Hardening Elements

55
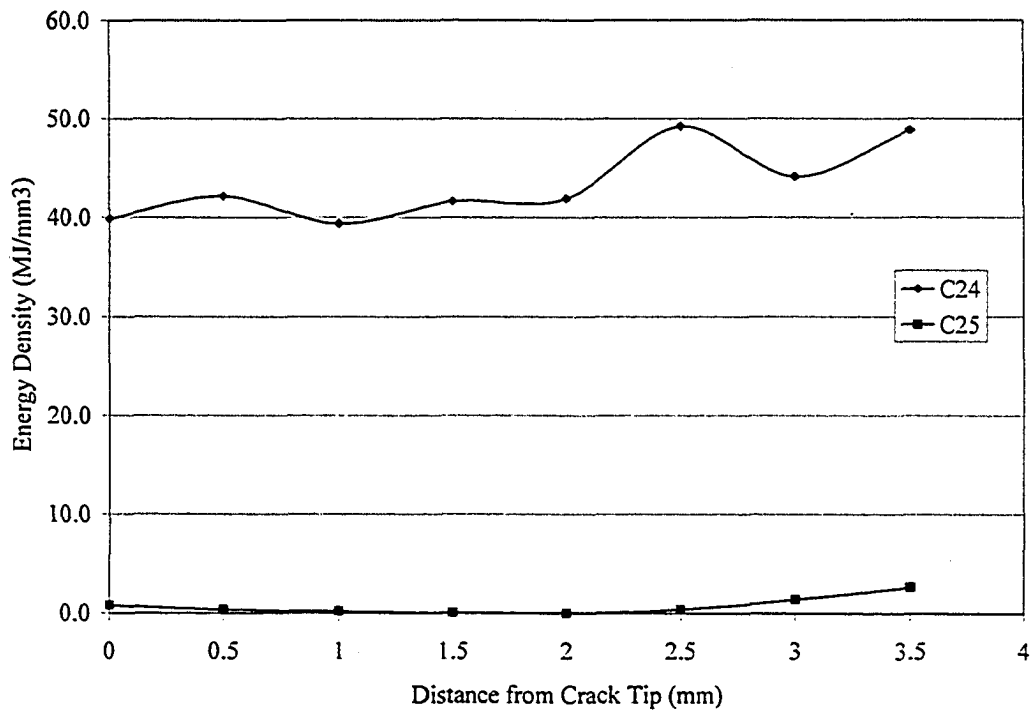
Figure 4-14 Energy Density versus Displacement from Notch Tip
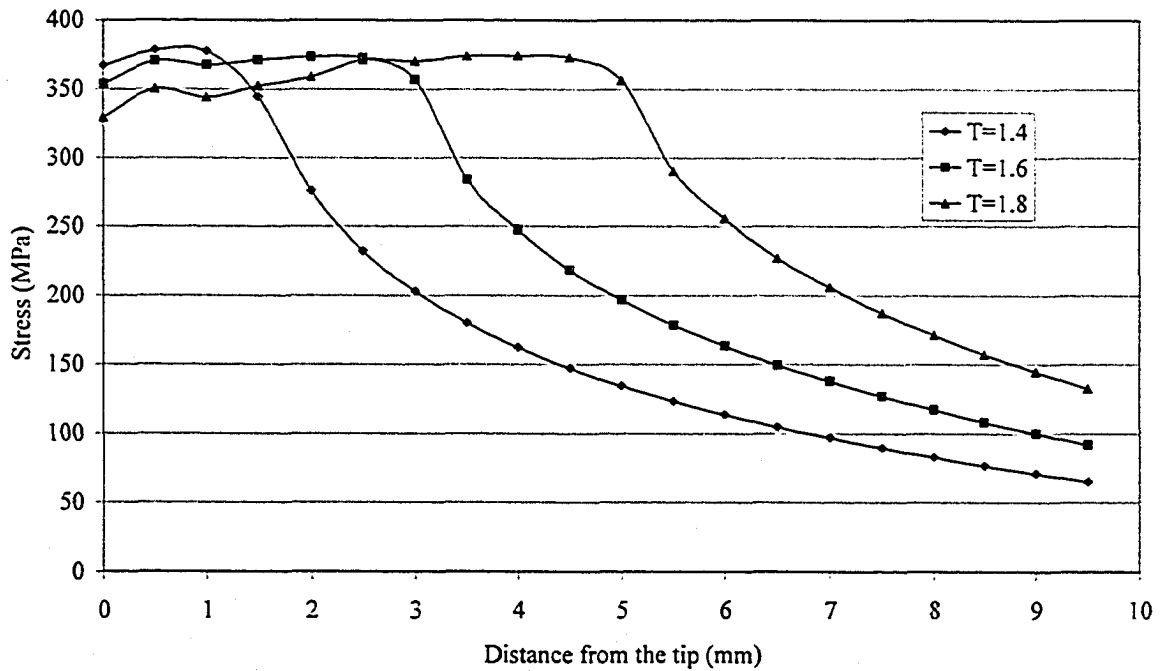
Figure 4-15 Stress versus Displacement from the Tip

56

5. APPLICATION TO A SIGNIFICANT STRUCTURE

5.1 History

The tarsand industry has grown for four decades and will supply over 10% of North America's oil needs by the year 2010. Extraction of the oil from tarsand starts with the surface mining equipment. The boom of the heavy shovels used for excavation of tarsand (cable hoisted or hydraulically driven) is typically a heavy steel plate welded box girder structure. Fatigue cracking caused by cyclic loading leads to frequent shut down for maintenance and loss of production. Figure 5-1 shows an observed crack across the full width of the bottom flange moving up the inner web plate in the field. Maintenance budget in Syncrude alone is over 50 million a year. Therefore, an economical and reliable method for prediction of crack initiation and crack propagation life of the equipment is greatly in demand.

As mentioned before, the work carried out in this project forms a part of a larger study funded by NSERC and Syncrude Canada to predict fatigue crack propagation in the boom of these shovels. As part of the study, a crack propagation analysis is required to evaluate the stress intensity factors at the tip of a crack as it propagates.

The proposed material model was found to be capable of predicting the peak load and the response at crack initiation and stable crack propagation under monotonic loading in a test sample. When a part of the structure reaches its peak load, a material crack can be simulated and the instant of fracture initiation can be predicted. This model is established to deal with fracture problems and requires further improvement to deal with fatigue problems. In chapter 4, calibrated material properties and the prediction of fracture initiation were shown. In the following section, a numerical simulation of shovel boom will be carried out to illustrate an application for the strain softening material model based on those material properties.

57

5.2   Numerical Simulation

The commercial finite element program ABAQUS/Standard was used for the numerical simulation of the boom of a BE395 electric shovel, which is shown schematically in Figure 5-2. The analysis had three major components – the geometry of the structure, the material model and the boundary conditions. The schematic model and finite element model of half the shovel boom are shown in Figure 5-3 and Figure 5-4, respectively.

Geometry

The finite element mesh of the boom was prepared by the research team (Yin et al., 2004). Field studies carried out by the team had shown that out-of-plane torsional effects in the boom are negligible. Only in-plane loads were therefore considered in the analysis and thus half of the boom was sufficient for simulation. Shell elements S3R and S4R were used to model half portion of the boom. S3R is 3-node finite-strain, bilinear, shell element with reduced integration while element S4R is a finite-strain 4-node bilinear shell element with reduced integration. These elements should respond to the softening model in an identical manner to the element used in the previous chapter. Finer elements were used at the crack location are shown in Figure 5-5. The mesh size at these locations was 12.5 mm wide by 49 mm long, for which the aspect ratio was about one to four.

A crack was simulated by the proposed material model. Cracks were observed on the bottom flange of the shovel boom in the field. Elements at potential crack location II were replaced with hardening and softening elements, as shown in Figure 5-6. Two strips of softening elements along the bottom flange and web were assigned and bounded by the hardening elements. The width of these strips, which influence the degree of softening, will be discussed in later. The material crack was assumed to propagate perpendicular to the edge of the shell.

58

The boom was loaded until the deformation rate (wavefront speed) was higher than the predefined limit. During the analysis, it was expected that fracture initiation would occur and the stiffness of structure reduced by the softening elements. At the moment of fracture initiation, more softening elements reach the yield strength limit and begin to soften.

The modulus of elasticity and Poisson's ratio were required as input for the behaviour in the elastic range. Beyond the yield strength limit, cracking model was applied to describe the plastic range. Cracking model functions *BRITTLE CRACKING and *BRITTLE SHEAR could not be used for the softening elements with ABAQUS/Standard; therefore, functions *CONCRETE, *TENSION STIFFENING and *FAILURE RATIOS were used for the description of the softening model. Since the function *PLASTIC could not handle two different material behaviour; thus, functions *CONCRETE and *TENSION STIFFENING were used to describe the stress-strain profiles for tension and compression, respectively. Absolute values of compressive stress and plastic strains were required as input for function *CONCRETE. For *TENSION STIFFENING, fraction of the remaining stress at cracking followed by absolute value of the direct strain minus the direct strain at cracking were required as input. Moreover, function *FAILURE RATIOS stated the failure criterion of the material. Since the predefined values are for the application of concrete cracking, these values were modified for steel in the following analyses. The stress-strain profiles for functions *CONCRETE and *TENSION STIFFENING are shown in Table 5-1 and Table 5-2, respectively. The capacity of the structure was reduced due to the material crack extension till rupture.

For hardening elements, the function *PLASTIC was used for the description of stress-strain profile. The true stress and plastic strain were required as input, as shown in Table 5-1. The first data point input must be the yield strength and zero plastic strain. This function controlled the hardening behaviour due to both compressive and tensile stresses.

59

Boundary Conditions

Three pins, one each at points A, B, and E, were modelled using analytical rigid surfaces, as shown in Figure 5-7. The pin at A represents the point where the base of the boom structure is attached to the shovel. The pin at E corresponds to the tip of the boom supported by cables, whereas the pin at B corresponds to the location of the saddle block. Each rigid surface had its own reference node, which controlled the movement and rotation of the pin itself. Thus, all the loads and constraints on the pin would be applied on these reference nodes. The pin at location A was constrained as a fixed support. The pin at location E was allowed to move in 1-direction while movements in 1- and 2-directions were allowed for the pin at location B. Degrees of freedom of each pin were listed in Table 5-3, where "C" and "F" designate constrained and free movement or rotation, respectively. Since half portion of the boom was used, a parameter ZSYMM was assigned on the node set on the symmetry plane as boundary conditions.

5.3   Analysis Procedure

The program determines increments of load based on increments of time along the load versus displacement curve for the structure. The time increments are chosen by the program so that a convergent numerical solution is obtained. The boom was loaded in three different load cases as shown in Figure 5-7. The load versus global displacement response and the stress-strain curve for the softening and hardening elements were plotted and compared. Furthermore, the major principal stress and the axial stress contours in the exterior and interior web of shovel boom for each load case and for different width of softening strip are shown in Figure 5-9 to Figure 5-17. The loading cases were described in the following:

1) A concentrated load of 31000 kN in direction 1 applied at pinE and strain-softening elements at location II;

60

2) A concentrated load of 32000 kN in direction 1 applied at the pinB and strain-softening elements at location II;

3) A concentrated load of -8000 kN in direction 2 applied at the pinB and strain-softening elements at location II.

These loads were determined so that the structure first showed reduction in structure stiffness in load versus displacement curve.

A study of quantity of softening elements with respect to the degree of softening was investigated. Two element sets, S1 and S2, were applied on the boom. The finite element mesh was constant in all analyses. Hardening and softening elements description refers only to the material model used. A strip of elements was defined as a line of elements along either the flange or the web, as shown in Figure 5-6. The first set, S1, consists of two strips of softening elements and two adjacent strips of hardening elements. The second set, S2, consists of four strips of softening elements with two adjacent strips of hardening elements. Combinations of softening element sets and loading cases were examined. Load versus displacement curves and stress versus strain curves for strain-softening and hardening elements at the potential crack location II are presented in Figure 5-18 to Figure 5-29.

Data of axial stresses (S11) and strains (E11) of the elements in direction 1 were retrieved from the analysis and plotted. E is designated as element and is followed by the element number. In the load versus displacement curve, the load was directly determined from the concentrated load applied at the specific time. The displacement in direction 1 was calculated by the difference between two nodal points of softening elements at the potential crack location II, which was considered as the deformation due to the applied load. The deformation was expected to be little because the elements would not be separated. N is designated as node and is followed by the two node numbers, which are separated by a dash, for displacement difference.

61

5.4 Numerical Results

5.4.1 Fracture initiation in the boom

Two stages of fracture process – onset of ductile fracture and stable crack propagation under monotonic loading – were predicted by the numerical simulation. With the application of strain-softening elements, the simulation successfully showed the reduction in boom stiffness in the load versus displacement curves when the elements reached the yield strength. The reduction was assumed to be caused by the material crack on the structure, i.e., progression of strain softening.

A summary of load at fracture initiation with combination of load cases and softening element sets is shown in Table 5-4. In the table, L stands for the load followed by the case number and S stands for the element set followed by the set number. Load-displacement curves with different load cases and softening element sets are presented in Figure 5-22 to Figure 5-29. In these figures, it is shown that the applied load kept increasing; however, the stiffness of the structure was reduced (the slope of load-displacement was reduced). Most combination of loading cases and elements sets could predict the load at fracture initiation except for load case L2 with all element sets. The PinA was slipped away from the boom before any fracture initiation. Generally, the numerical simulation could predict the fracture process including the fracture initiation and the crack propagation shortly after. The softening elements successfully reduced the capacity of the structure.

The load versus displacement curve for case L1S1 and case L1S2 are shown in Figure 5-22 and Figure 5-23, respectively. Fracture initiation at section 1 under load case (L1S1) occurred at 25000 kN while it occurred at 26000 kN at section 2 for the same load case (L1S2). After the point of fracture initiation, the applied load increased slowly to about 31000 kN before the analysis was terminated. The termination was caused by excessive distortion of some elements with large aspect ratio. The final displacement for cases L1S1 and L1S2 were 0.024 and 0.029 mm, respectively.

62

The load versus displacement curve for case L3S1 and case L3S2 are shown in Figure 5-28 and Figure 5-29, respectively. Fracture initiation occurred at -6500 kN in both cases L3S1 and L3S2. After the point of fracture initiation, the applied load kept increasing slowly to about -8000 kN before the analysis was terminated. The final displacements for cases L3S1 and L3S2 were 0.028 and 0.026 mm, respectively.

A typical stress versus strain profile of softening elements in the boom is shown in Figure 5-19. When softening elements reached the yield strength, these elements were softened at a very slow rate. Element E7029 started to soften after 0.2% strain. Moreover, some elements such as E7030 experienced unloading before reaching the yield strength limit. It could be explained because some softening elements could reach the yield strength earlier than others. When these yielded elements softened, the elements that had not yielded had to be unloaded as they were adjacent to softening elements.

Effect of Quantity of Softening Elements

The effect of softening elements was studied and two sets of element arrangement at sections S1 and S2 were compared. The elements in Figure 5-18 and Figure 5-19 were assigned with softening property while those in Figure 5-20 and Figure 5-21 were assigned with hardening property. From the perspective of stress versus strain relationship, elements plotted in Figure 5-18 did not show obvious softening behaviour but slow-rate hardening. However, element E7030 showed reduction in stress with increasing strain in Figure 5-19. The other elements shown in Figure 5-19 experienced slow-rate hardening, which was not be observed in Figure 5-18. At the same time, hardening took place in both Figure 5-20 and Figure 5-21. Stress of elements increased with increasing strain; however, it was observed that the increment rate of stress was slow. It could be explained that stresses of hardening elements had to be reduced due to the adjacent softening elements. Therefore, these elements reached a plateau before further reduction in stress states.

63

From the perspective of load versus displacement response for softening element sets S1 and S2, softening elements work well and show the softening behaviour by changing the quantity of elements, as shown in Figure 5-22 and Figure 5-23. N is designated as node and is followed by the two node numbers. There is no difference in the curves N19-978 and N978-977 in both graphs but in curve N977-976. Curve N977-N976 does not show reduction in load with increasing displacement in Figure 5-22. Element set S2 showed better prediction of load-displacement curve than element set S1. Owing to these observations of the numerical results, it was shown that the quantity of softening elements was important to control the degree of softening.

Effect of Loading Cases

Effects of loading cases L1 and L3 on the softening elements were investigated. Load was applied on the structure in 1- and 2- direction in cases L1 and L3, respectively. It was necessary to study whether the behaviour of softening elements could be affected by the direction of applied load. From the point of view of stress-strain relationship, there is no effect that the softening behaviour is prohibited by the direction of applied loads. For instance, elements E7030 in case L1 and L3 showed softening behaviour in Figure 5-19 and Figure 5-25, respectively. On the other hand, those adjacent hardening elements experienced hardening after reaching the yield strength limit. No direct comparison could be made because two load cases were different situations but it could be concluded that the elements could experience softening with applied loads in parallel or perpendicular directions.

From the load-displacement curve it is evident that softening elements work well in both loading cases. Boom stiffness was reduced at the moment of fracture initiation in both curves, as shown in Figure 5-23 and Figure 5-29. From these results determined by the finite element analyses, it was found that these softening elements were capable of generating a material crack and reducing the capacity of structure.

64

Several locations were considered because material crack might initiate and propagate at these locations. These locations were: a) the exterior web; b) the interior web; and c) the exterior bottom flange. The crack could only be indirectly revealed from the stress state on the structure. The influence of crack could be observed from the stress state. Axial stress and maximum principal stress contour at fracture initiation are presented through Figure 5-8 to Figure 5-17. These contours show the crack initiation and propagation at the bottom flange of the boom.

There were only minor differences between the principal stresses and the axial stresses based on the comparison of figures a) with figures b) in Figure 5-8 to Figure 5-17. It is therefore noted that the stresses in the boom were primarily axial stresses. The locations of high stresses, indicated in dark colour, were in areas where cracks had been detected in the booms. The results might not be obvious for load case L1 as the elements at potential crack location II were under tensile forces. In Figure 5-9a, higher stress around the crack location could be observed rather than that in Figure 5-9b. In Figure 5-16 and Figure 5-17, the elements at potential crack location II experienced tension and compression. Yin et al. (2004) also pointed out that these stresses did not account for localized stress concentrations expected at the diaphragm welds. Further mesh refinement is suggested in order to assess these localized stresses.

However, distinctive features in stress state could be observed between Figure 5-13 and Figure 5-17. Stress concentration at stiffener location and onset of localization can be found in both figures. In Figure 5-17, the stress states of elements at which the onset of localization took place were reduced and surrounding elements were in higher stress state. The stress pattern at the crack location was different from that at the stiffener location.

5.4.2 Crack Propagation

The second stage of fracture process was also examined. The material model could only predict the crack propagation shortly after the fracture initiation. The boom was weakened by the softening elements at a point, as shown in Figure 5-23 and Figure 5-29. From these load-displacement curves, the applied load kept increasing and did not drop before the analyses were terminated.

From the perspective of stress-strain relationship, softening behaviour was shown in some elements after reaching the peak stress. However, the peak stress was not the same as the yield strength limit. Some softening elements even experienced slow-rate hardening before the analyses were terminated. The fracture strain was predicted when the stress of softening element was extrapolated to about 10 MPa, which was assumed to be rupture. The fracture strains were extrapolated to 0.026 and 0.015 in Figure 5-19 and Figure 5-25, respectively, which was determined to be 0.170 in previous chapter. The extrapolated values were quite different from the fracture strain used in the material model. It could be explained by two possible explanations. The first explanation was that the brittle fracture model was not the appropriate model to simulate the crack initiation and propagation for the boom. The observation of stress-strain relationship was similar to the proposed material model for ductile fracture, as shown in Figure 3-2. Load redistribution is assumed to take place in the boom structure when the first smear crack appears. The first smear crack has little influence on load reduction in the boom but not enough to greatly reduce the load carrying capacity. Several smear cracks on the boom are required in order to lead to complete breakdown. This assumption could be verified as limited experimental results were provided at that moment. The second explanation was that the softening elements did not reach the yield strength limit before softening, which was an assumption for the brittle model. Further investigations are required for the proposed material model for both brittle and ductile fracture.

5.5 Summary

With the aid of the proposed material model, the onset of ductile fracture and stable crack propagation under monotonic loading could be predicted. Softening element played an important role to simulate a material crack and to reduce the loading capacity of boom, which could be considered as an alternative to model the fracture behaviour. Nevertheless, such a model was incapable of predicting the deformation precisely around the desired crack location. No debonding between elements took place in analyses but the fracture behaviour was observed indirectly through the load versus displacement and stress versus strain curves.

The material model was a pilot model to predict the fracture initiation and there were two limitations on its application. First, for simplicity, crack was assumed to propagate perpendicular to the surface of shell elements (web or flange) of boom in all analyses. It is not necessarily true in the real structure. Therefore, the model should to be modified in order to simulate inclined crack propagation. Second, the effect of temperature and loading rate were not considered in the above analyses. Further investigations on these effects are required.

The effect of quantity of softening elements and loading cases were investigated. Softening elements were found to be critical to the softening process (or reduction of the boom stiffness generated by a material crack). Moreover, it was found that softening process could take place with different loading directions. The boom was expected to fail in brittle manner, instead it shows a ductile behaviour but is limited by the numerical demands of ABAQUS. This model was applicable to determine the moment of fracture initiation and some stable crack propagation with assigning the softening elements on the structure.

The proposed brittle and ductile fracture models were expected to illustrate a general picture of fracture behaviour and they required more experimental results to verify and calibrate the models. This report could briefly illustrate the application of these two models.

Table 5-1 Material properties used in ABAQUS analysis (*CONCRETE and *PLASTIC)

Elasticity of Modulus, E = 186300 MPa	Poisson Ratio, υ = 0.3
True Stress (MPa)	Plastic Strain
372.8	0.00000
418.6	0.02575
445.1	0.03369
473.0	0.04442
508.0	0.06259
541.4	0.09103
578.9	0.14117
1114.6	1.00000

Table 5-2 Material Properties used in ABAQUS analysis (*TENSION STIFFENING)

Remaining Direct Stress	Direct Cracking Strain
1.00	0.000
0.05	0.170
0.01	1.000

Table 5-3 Boundary Conditions at Pin locations

Pin Set	Displacement			Rotation		
	1 (x)	2 (y)	3 (z)	4 (x-axis)	5 (y-axis)	6 (z-axis)
PIN-A	C*	C	C	C	C	C
PIN-B	F**	F	C	C	C	C
PIN-E	F	C	C	C	C	C

*C = constrained, **F = free movement or rotation

Table 5-4 Load at Fracture Initiation

Load Case	Load at Fracture Initiation (kN)	Final Displacement (mm)	Loading Direction at Pin
L1S1	25000	0.024	1
L1S2	26000	0.029	1
L2S1	Not Available	Not Available	1
L2S2	Not Available	Not Available	1
L3S1	-6500	0.028	2
L3S2	-6500	0.026	2

68
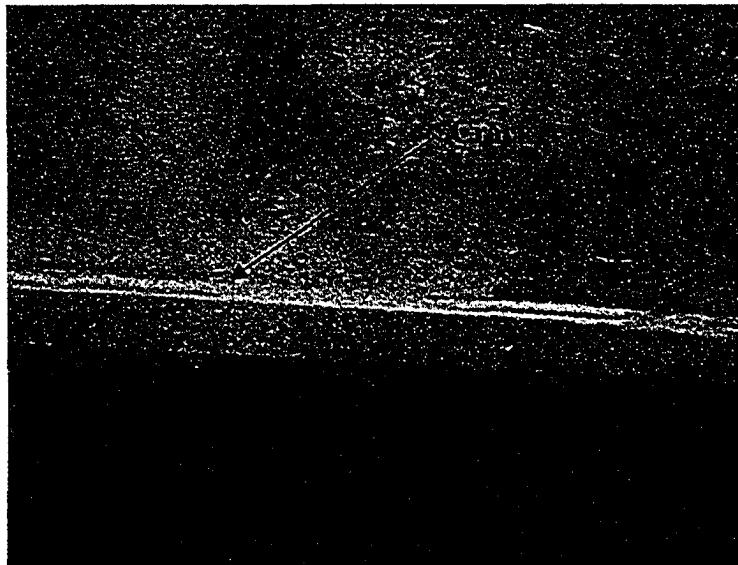
Figure 5-1 An Observed Crack Crossing the Bottom Flange Full Width and Moving up the Inner Web Plate (Yin et al., 2004)
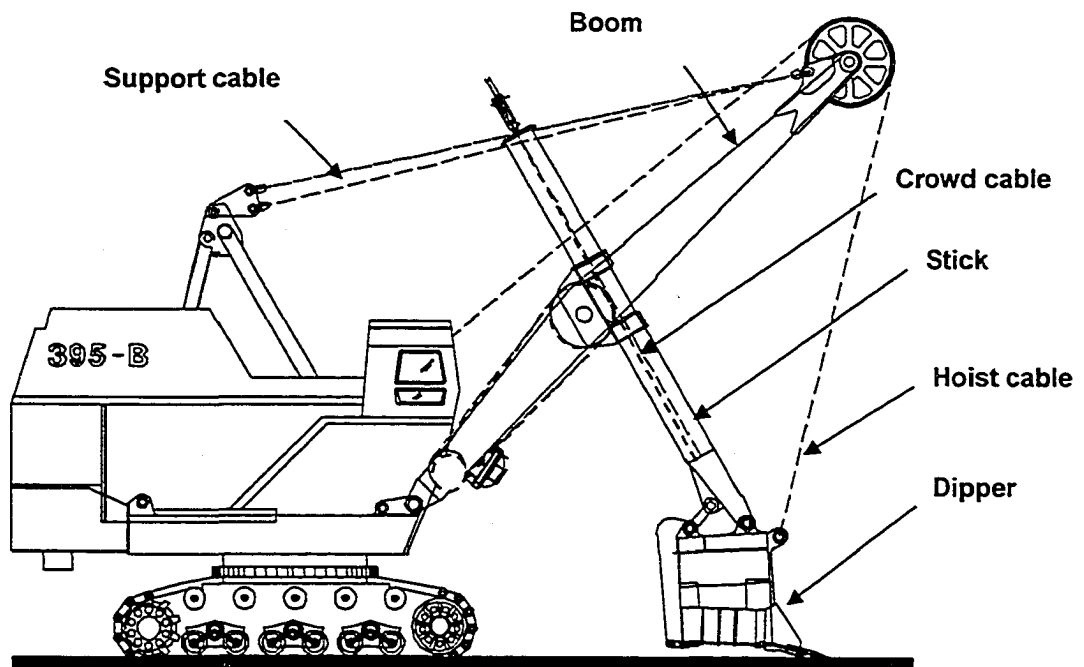
Figure 5-2 BE 395B Shovel (Yin et al., 2004)
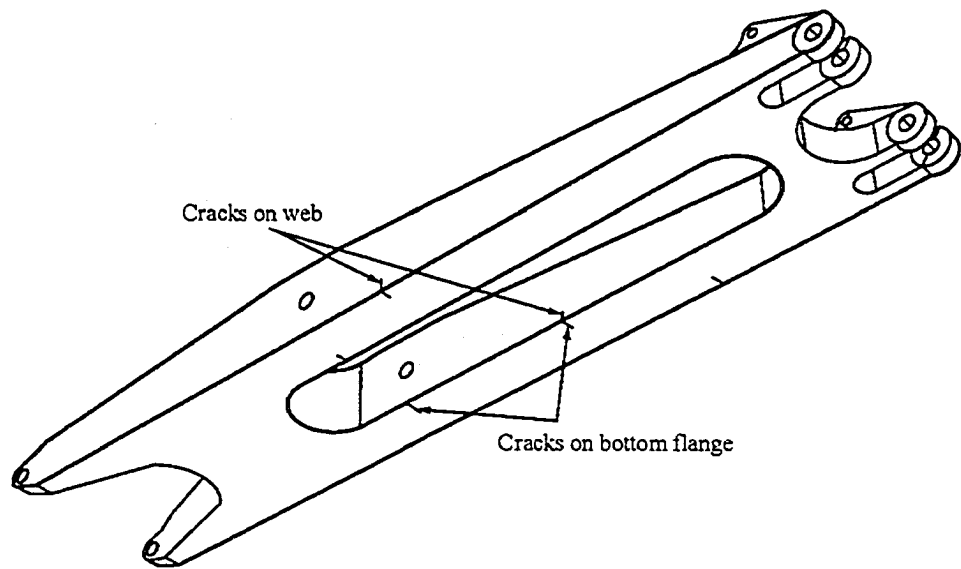
Figure 5-3 A Schematic of the Boom (Yin et al., 2004)
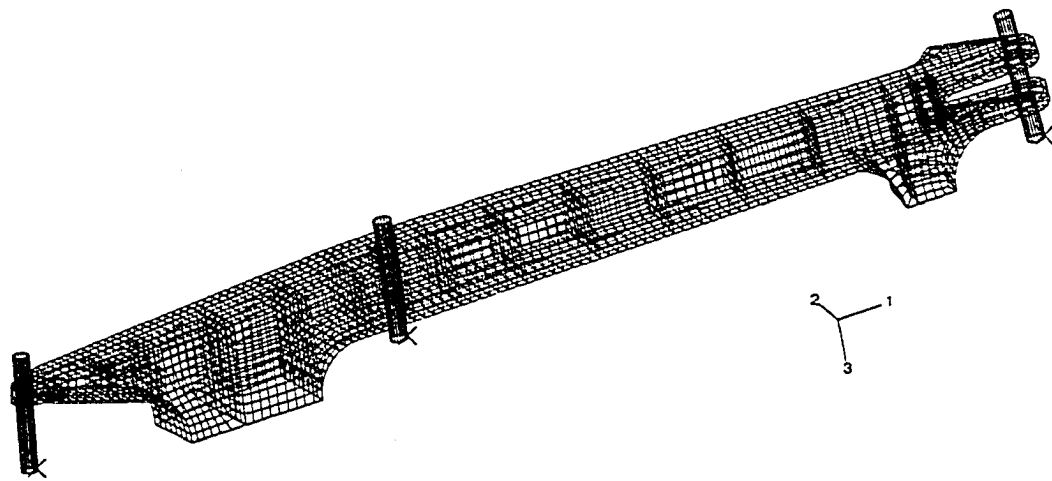
Figure 5-4 Finite Element Model of the Boom (Yin et al., 2004)

70
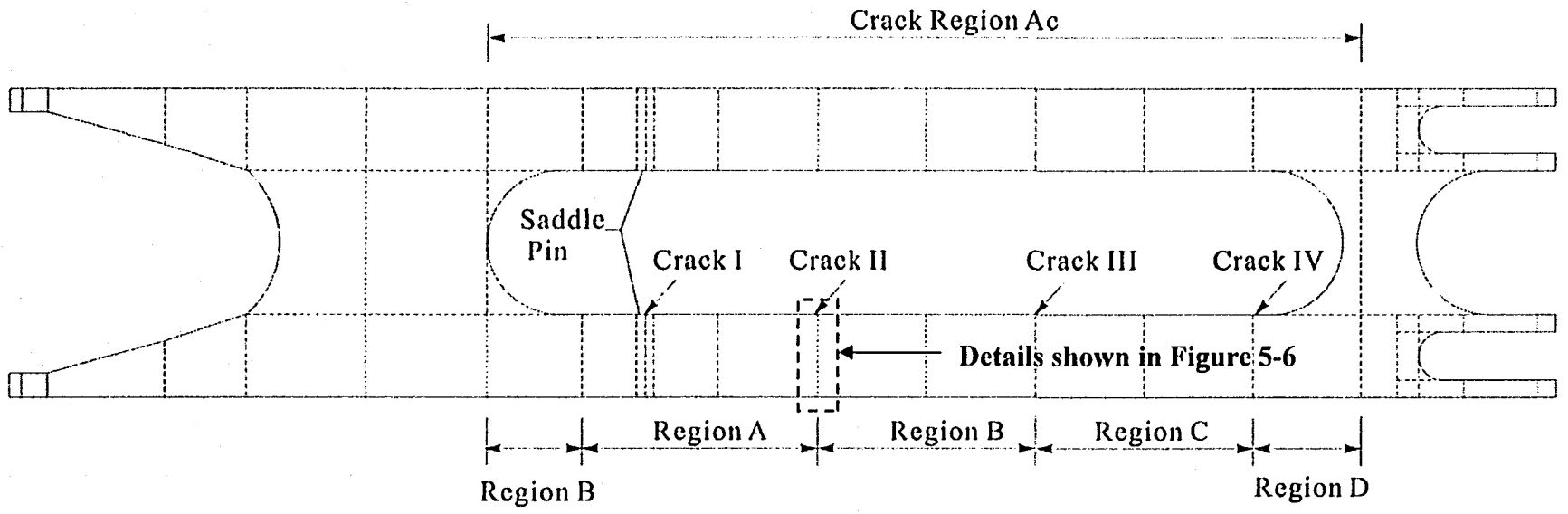
Figure 5-5 Potential Crack Zones on the Boom (Top view) (Yin et al., 2004)

71

(a) Element Set S1   (b) Element Set S2
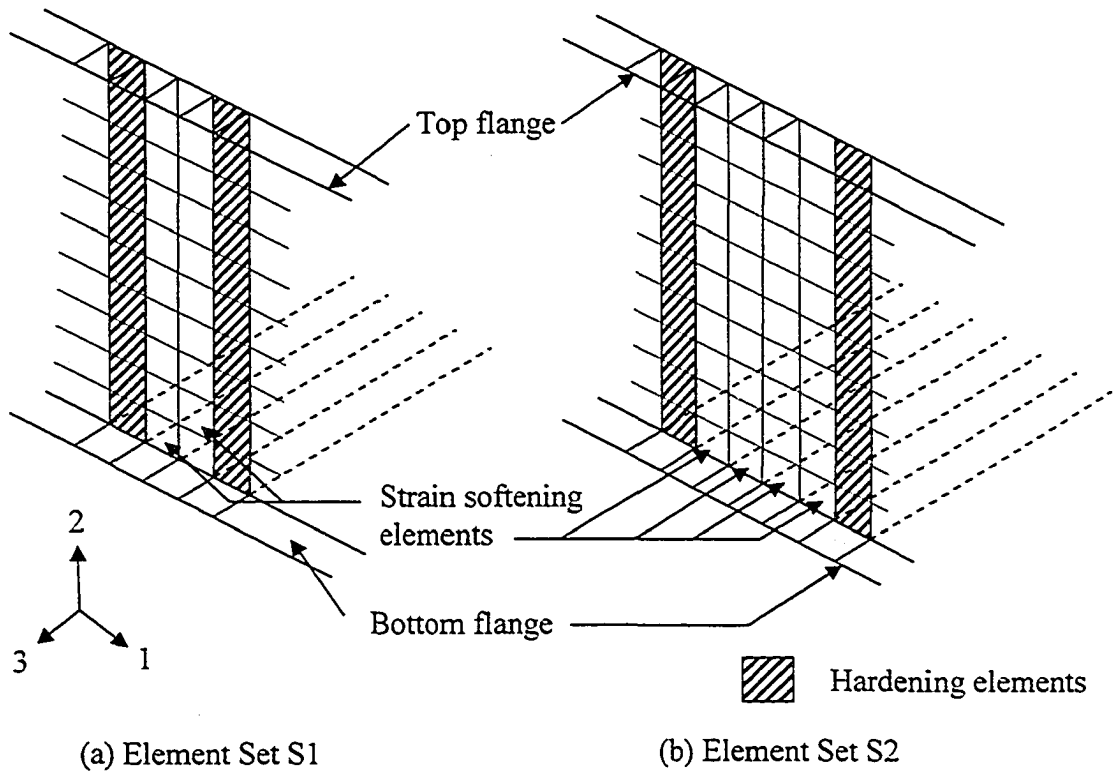
Figure 5-6 Application of Softening and Hardening Elements on the Boom

(a) Load Case 1   (a) Load Case 2   (a) Load Case 3
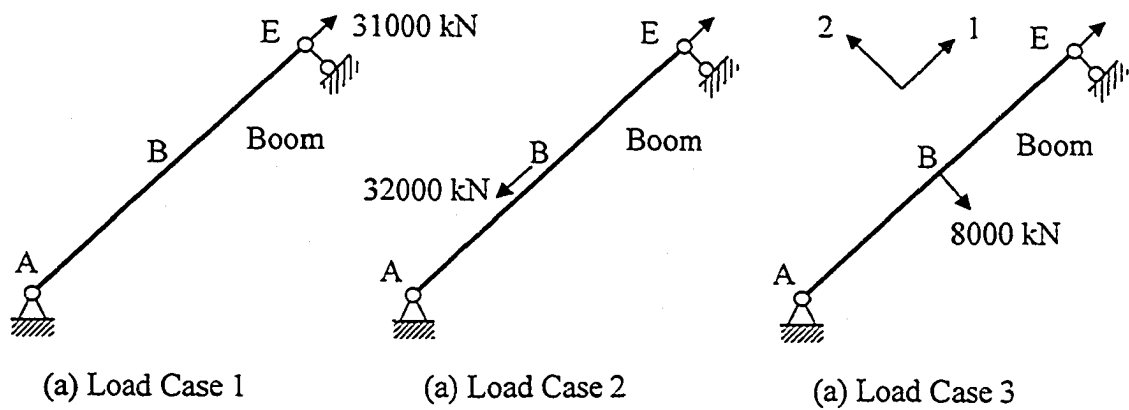
Figure 5-7 Basis Load Cases Considered

72
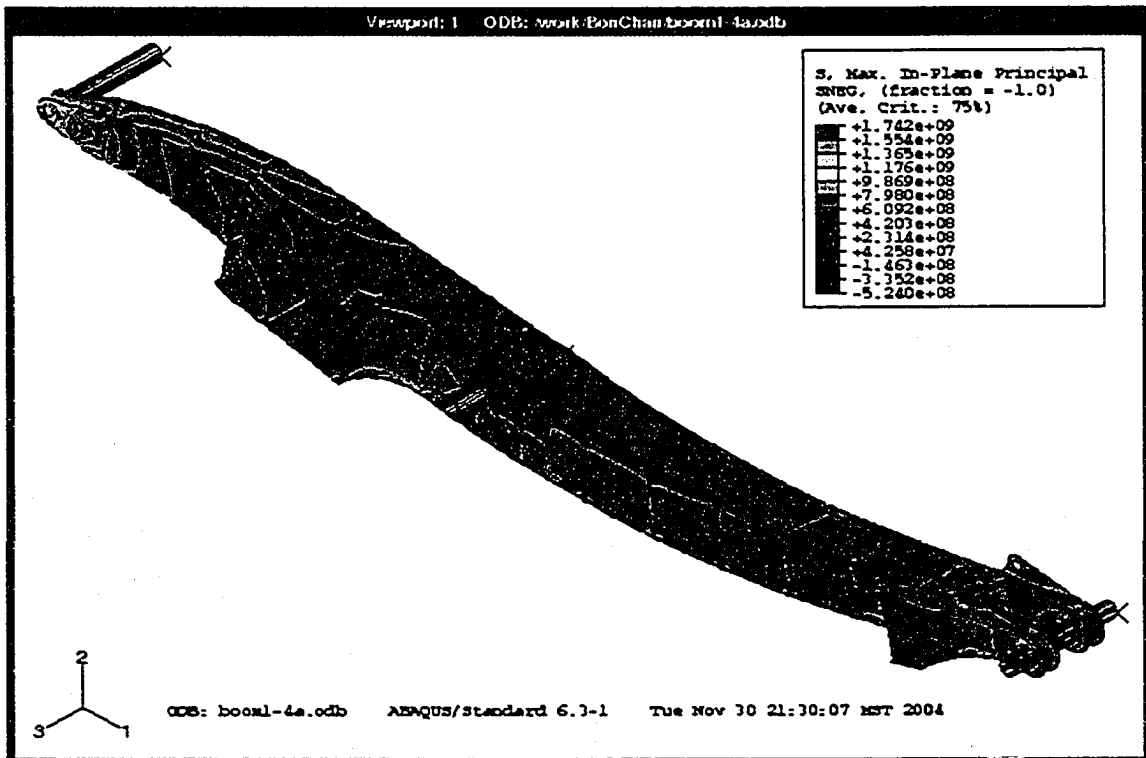
a) Maximum Principal Stresses
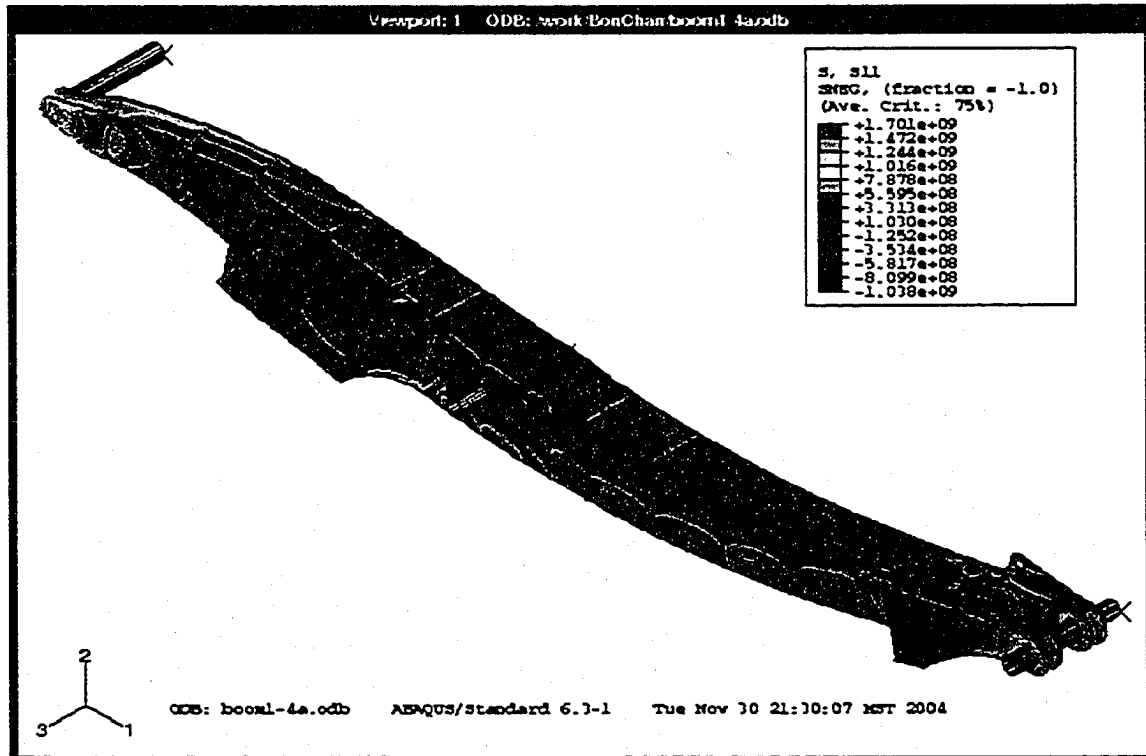
b) Axial Stresses

Figure 5-8 Stress Contour of Boom (Load Case 1 and Element Set S1)

73
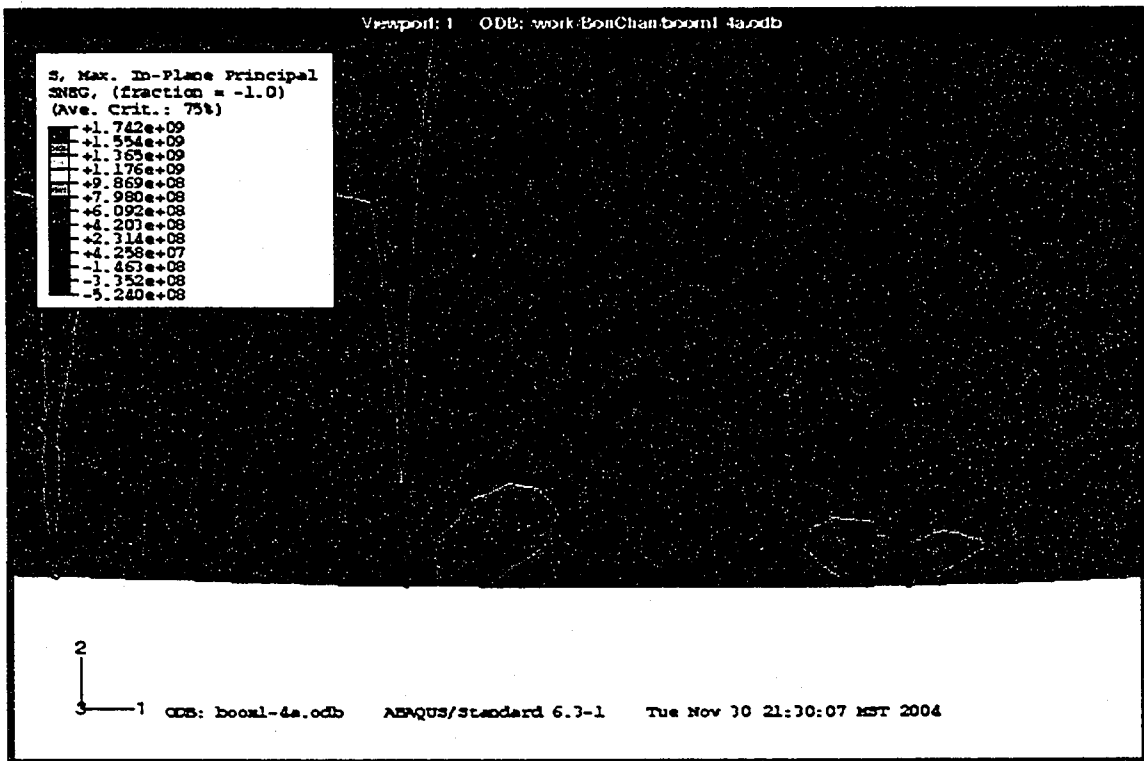
a) Major Principal Stresses
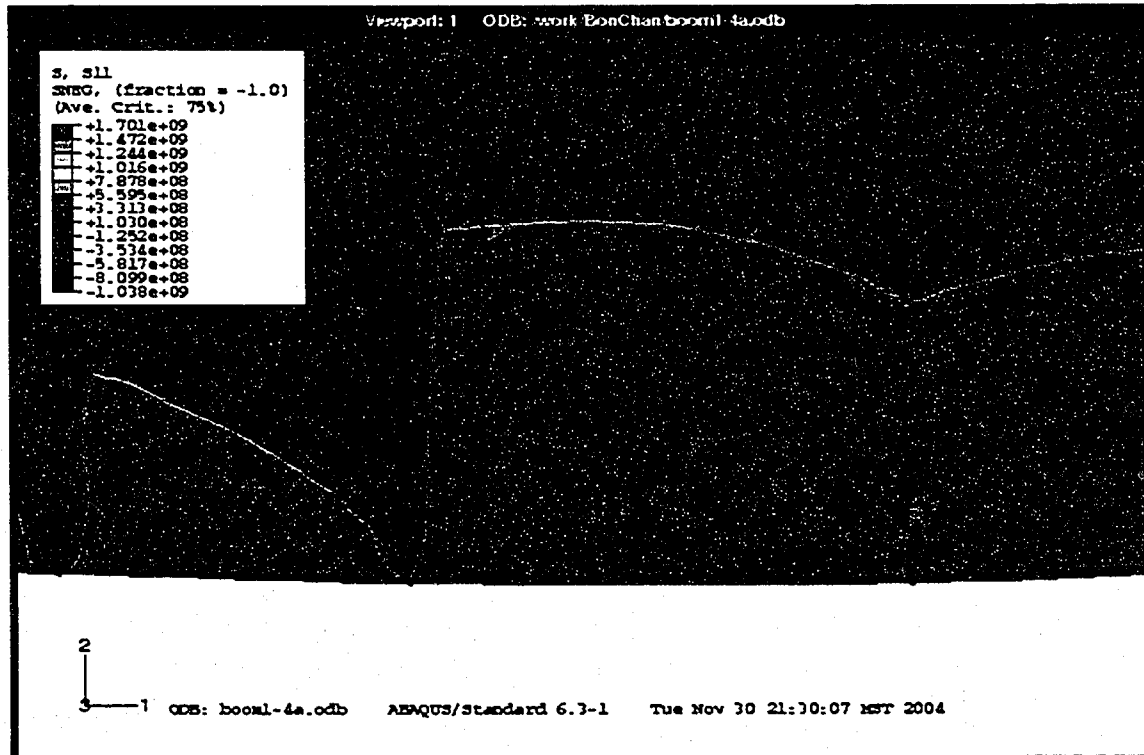
b) Axial Stresses

Figure 5-9 Stresses in the Interior Web of Shovel Boom (Load Case 1 and Element Set S1)

74
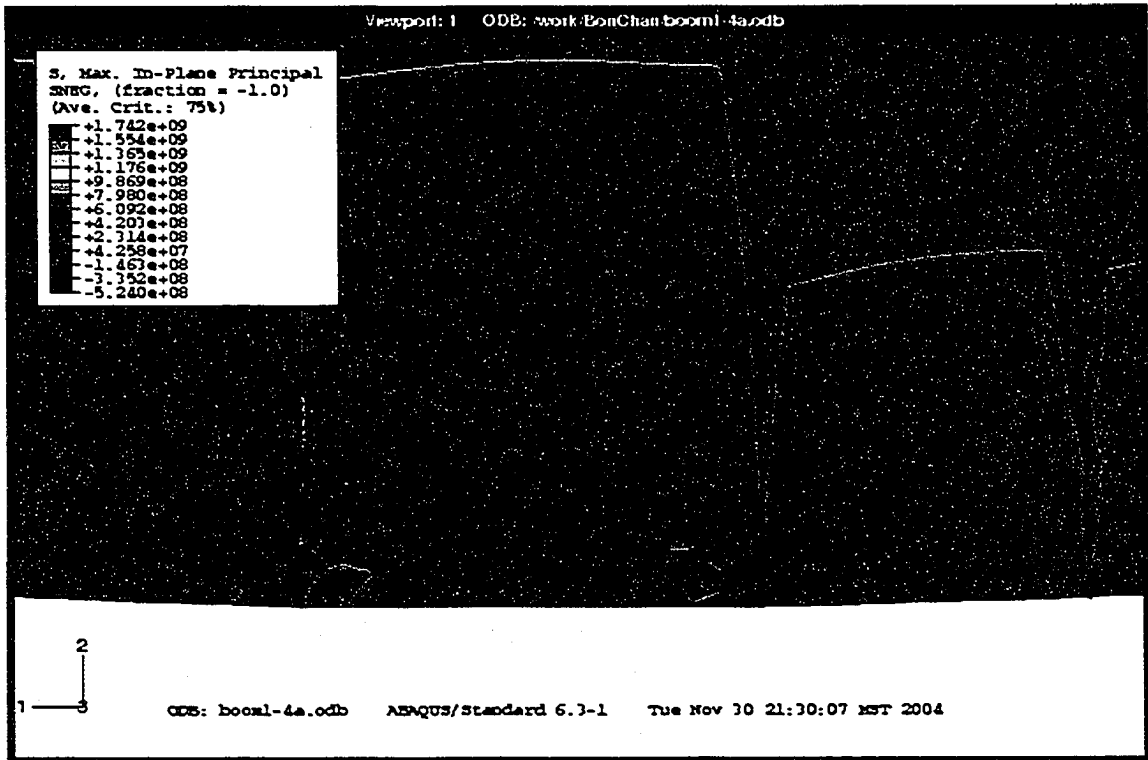
a) Major Principal Stresses
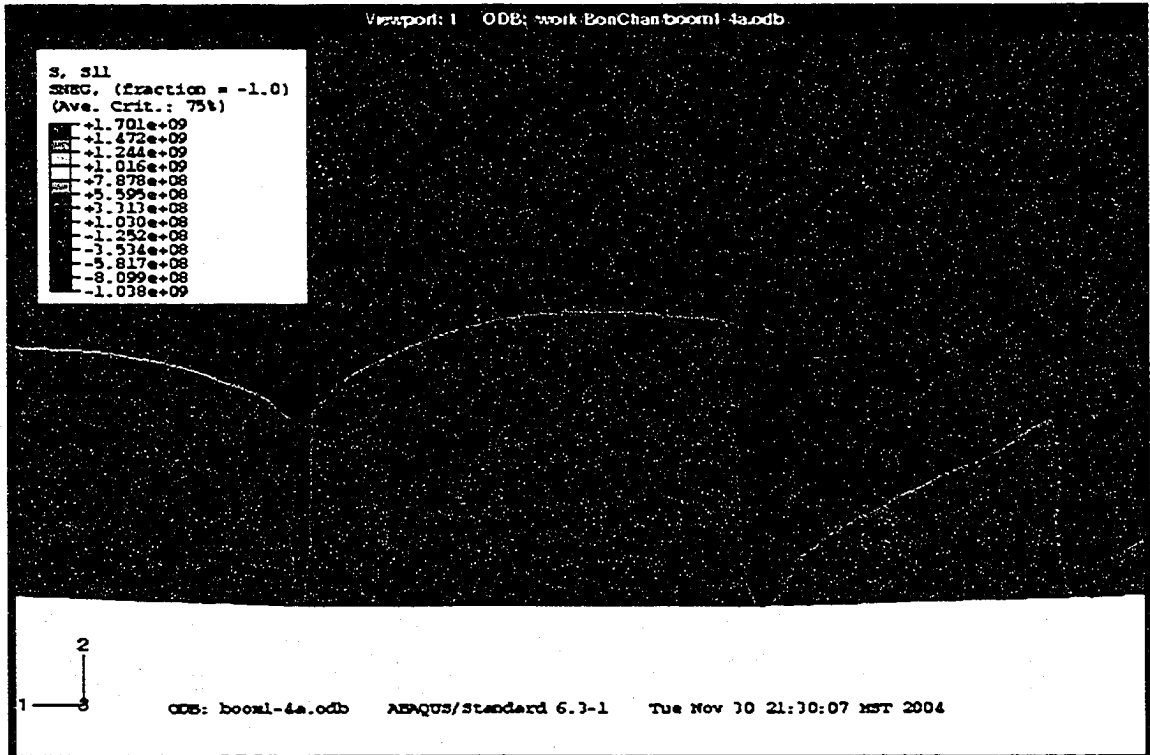
b) Axial Stresses

Figure 5-10 Stresses in the Exterior Web of Shovel Boom (Load Case 1 and Element Set S1)

75

S, Max. In-Plane Principal
SNEG, (fraction = -1.0)
(Ave. Crit.: 75%)
    +1.742e+09
    +1.554e+09
    +1.365e+09
    +1.176e+09
    +9.869e+08
    +7.980e+08
    +6.092e+08
    +4.203e+08
    +2.314e+08
    +4.258e+07
    -1.463e+08
    -3.352e+08
    -5.240e+08

3
|
2———1   ODB: booml-4a.odb   ABAQUS/Standard 6.3-1   Tue Nov 30 21:30:07 MST 2004

a) Maximum Principal Stresses

S, S11
SNEG, (fraction = -1.0)
(Ave. Crit.: 75%)
    +1.701e+09
    +1.472e+09
    +1.244e+09
    +1.016e+09
    +7.878e+08
    +5.595e+08
    +3.313e+08
    +1.030e+08
    -1.252e+08
    -3.534e+08
    -5.817e+08
    -8.099e+08
    -1.038e+09

3
|
2———1   ODB: booml-4a.odb   ABAQUS/Standard 6.3-1   Tue Nov 30 21:30:07 MST 2004
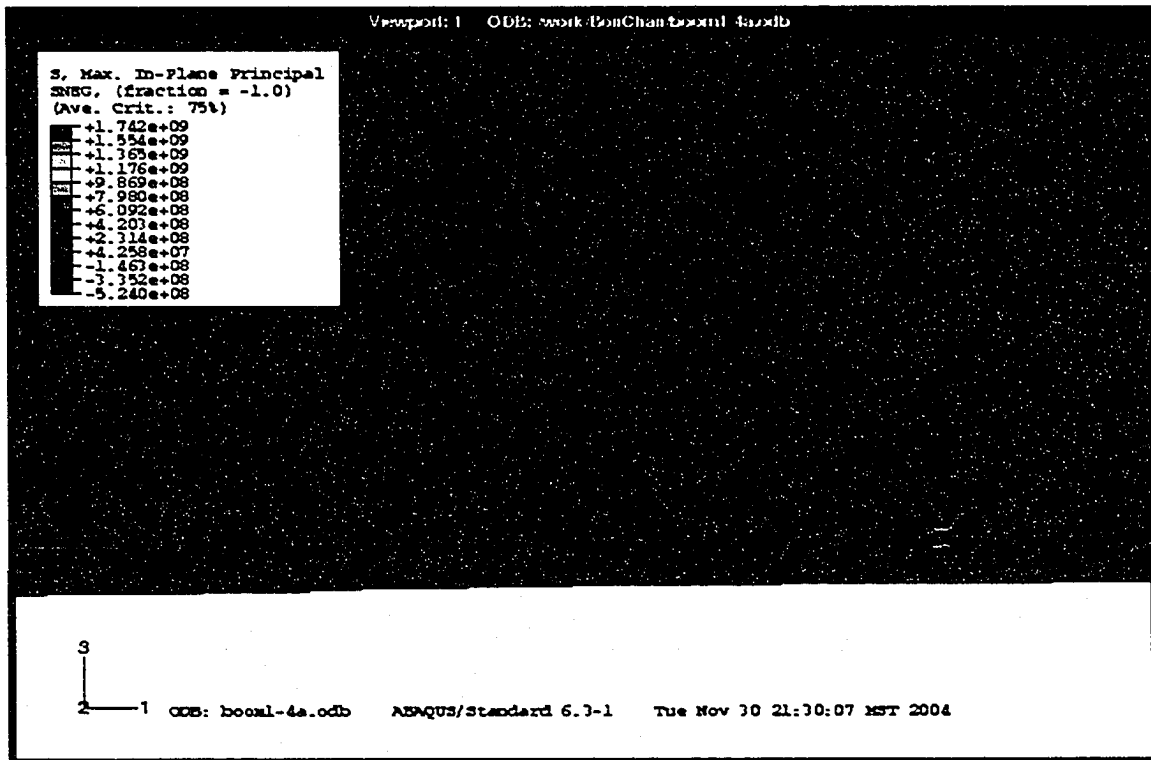
b) Axial Stresses

Figure 5-11 Stresses in the Exterior Bottom Flange of Shovel Boom (Load Case 1 and Element Set S1)
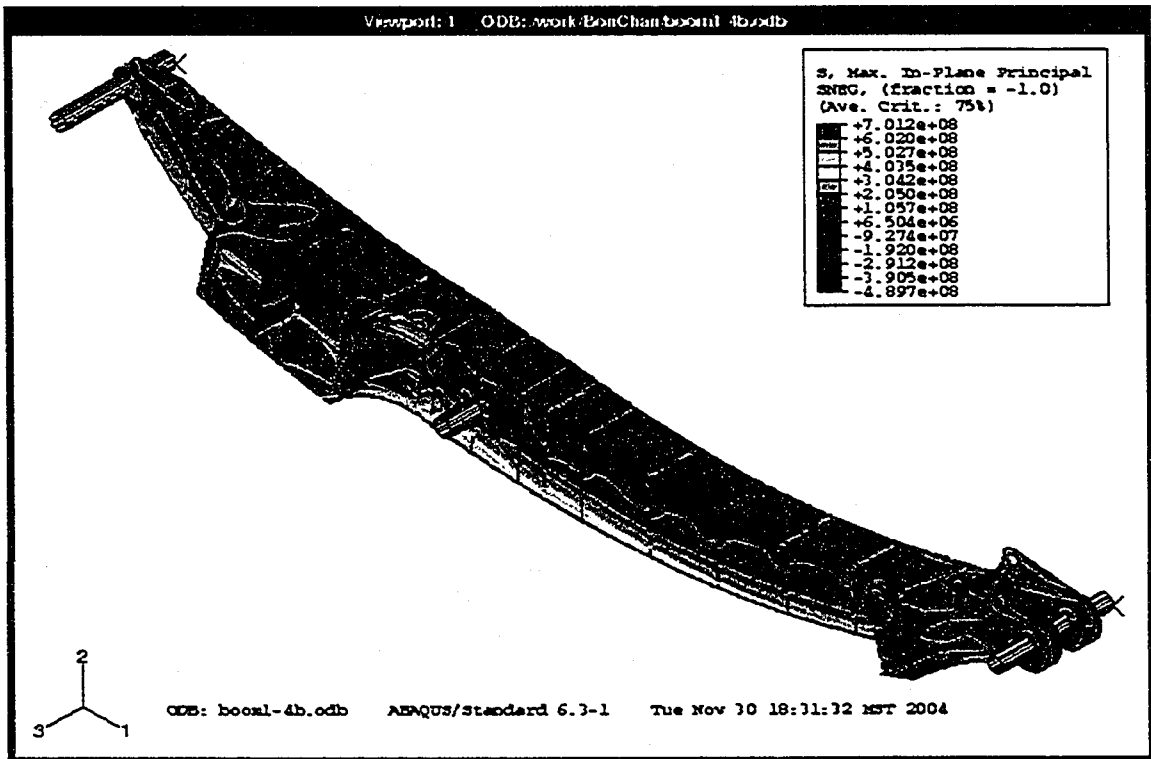
a) Maximum Principal Stresses
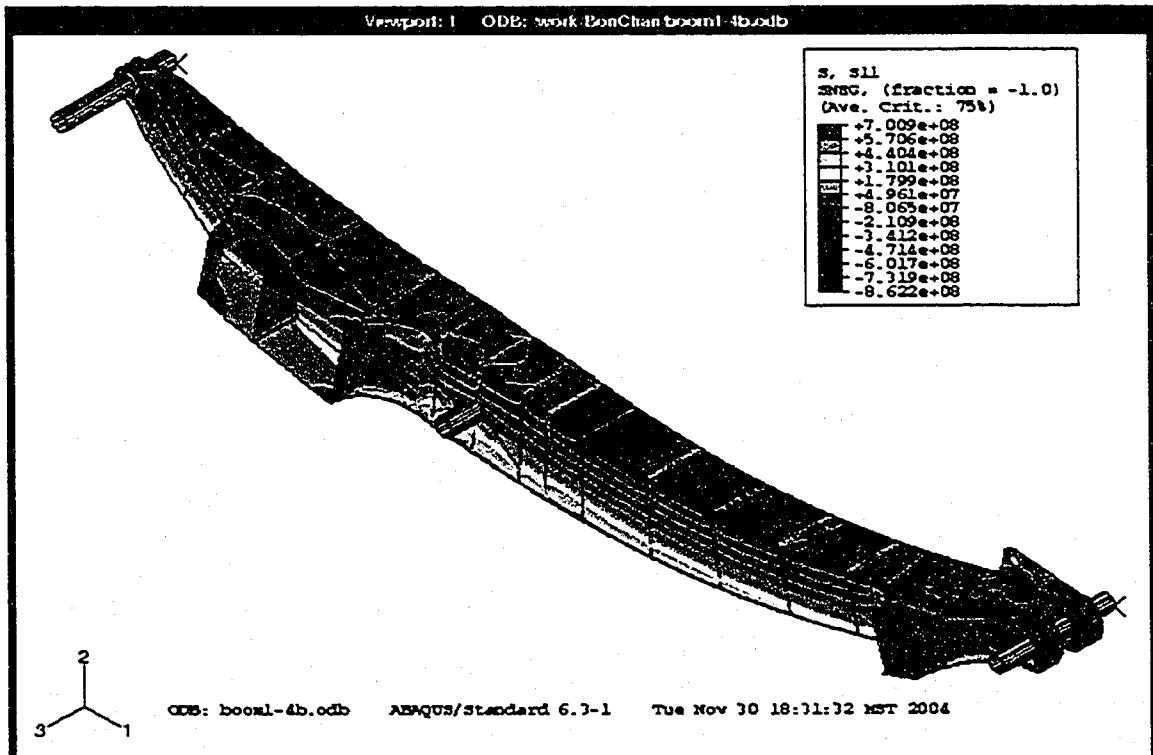
b) Axial Stresses

Figure 5-12 Stress Contour of Boom (Load Case 3 and Element Set S1)

77

a) Major Principal Stresses

Stress concentration at stiffener location

Onset of localization
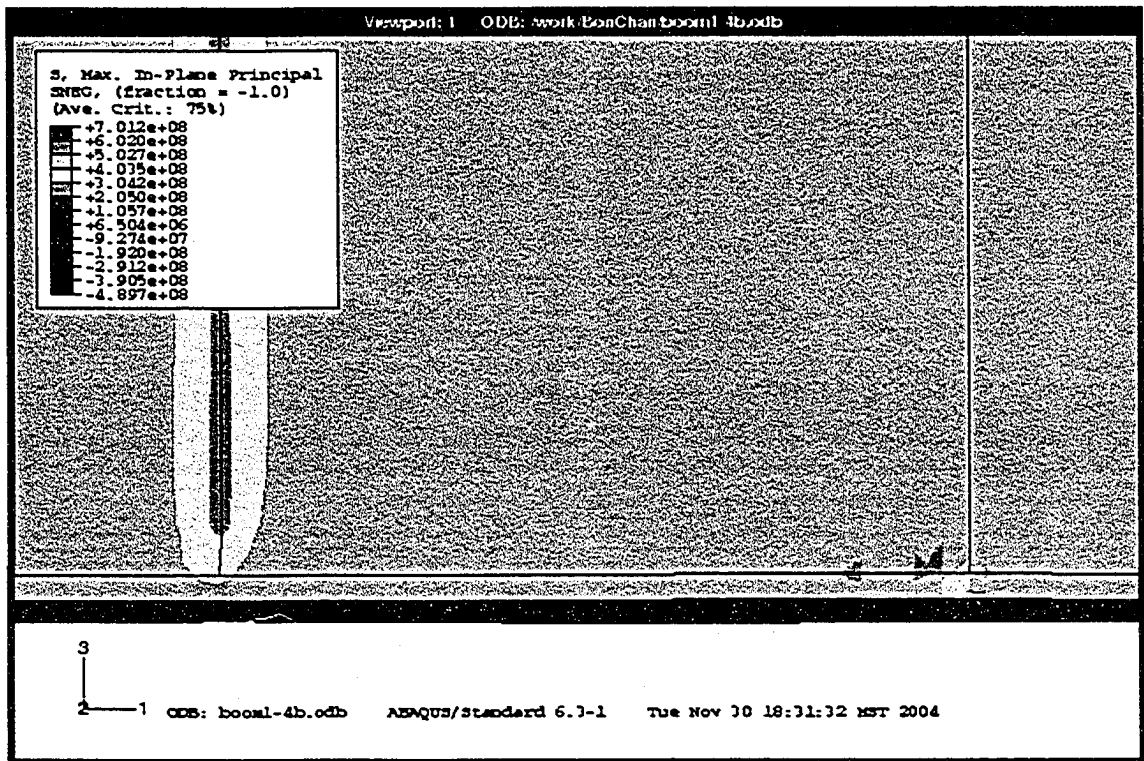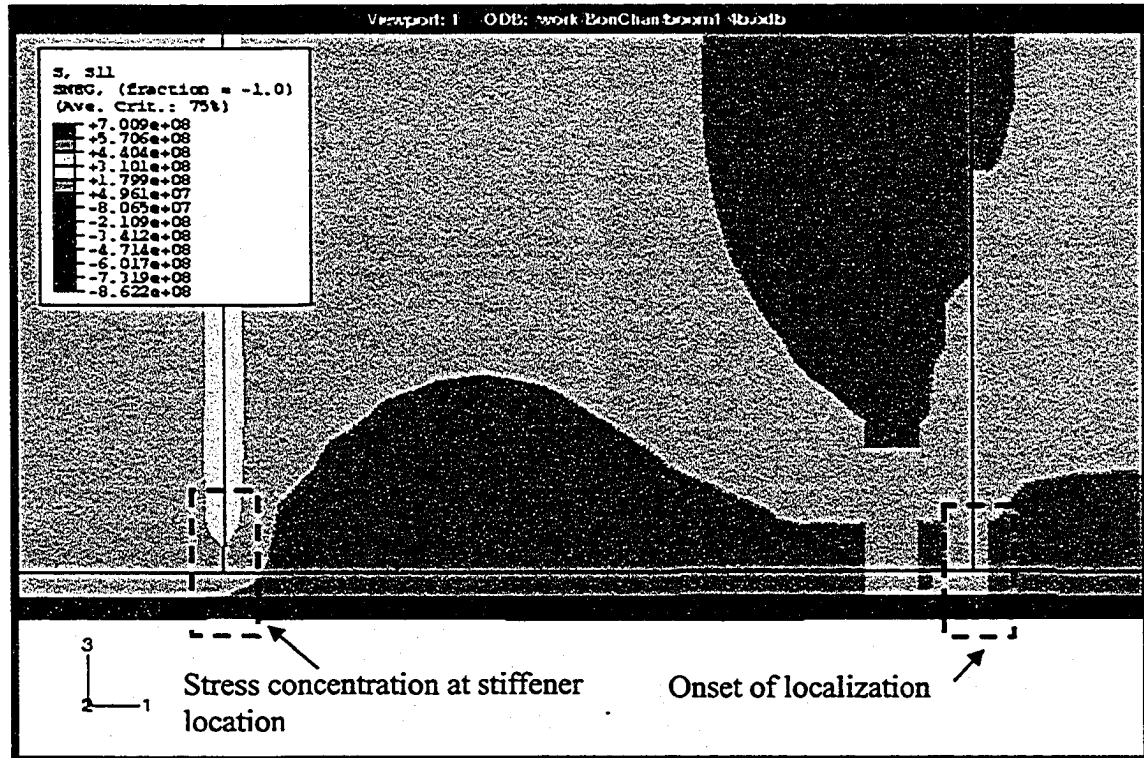
b) Axial Stresses

Figure 5-13 Stresses in the Exterior Bottom Flange of Shovel Boom (Load Case 3 and Element Set S1)

78
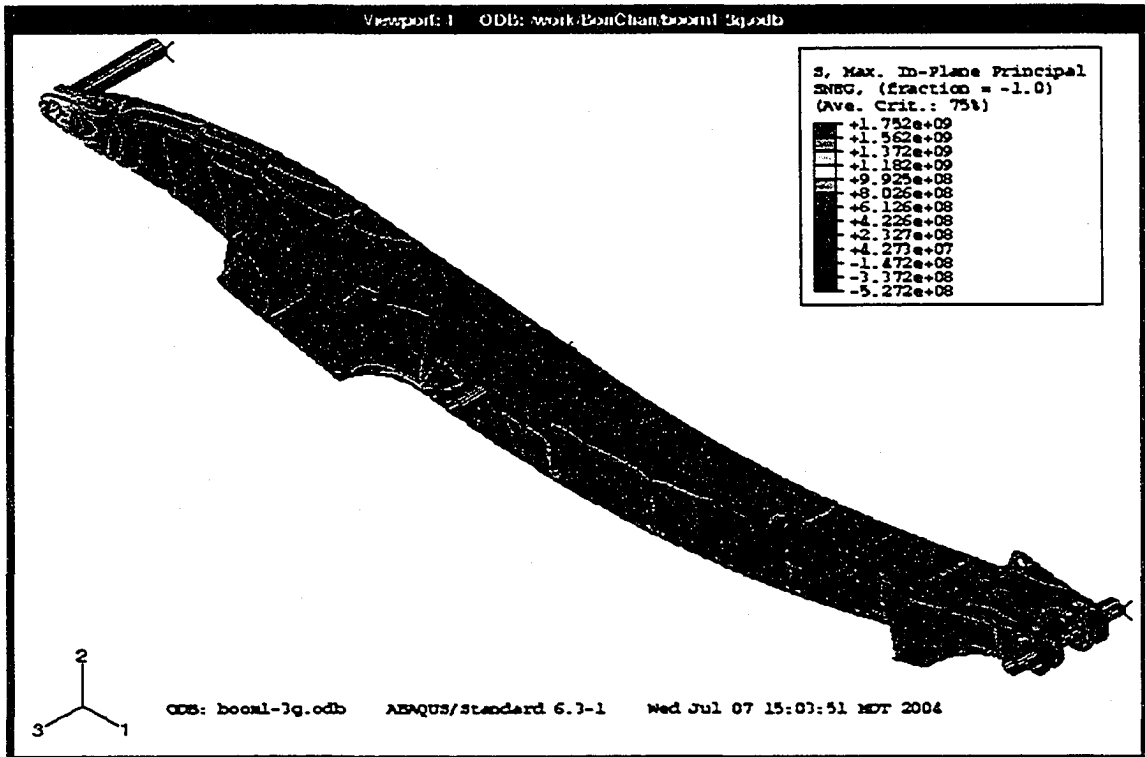
a) Maximum Principal Stresses
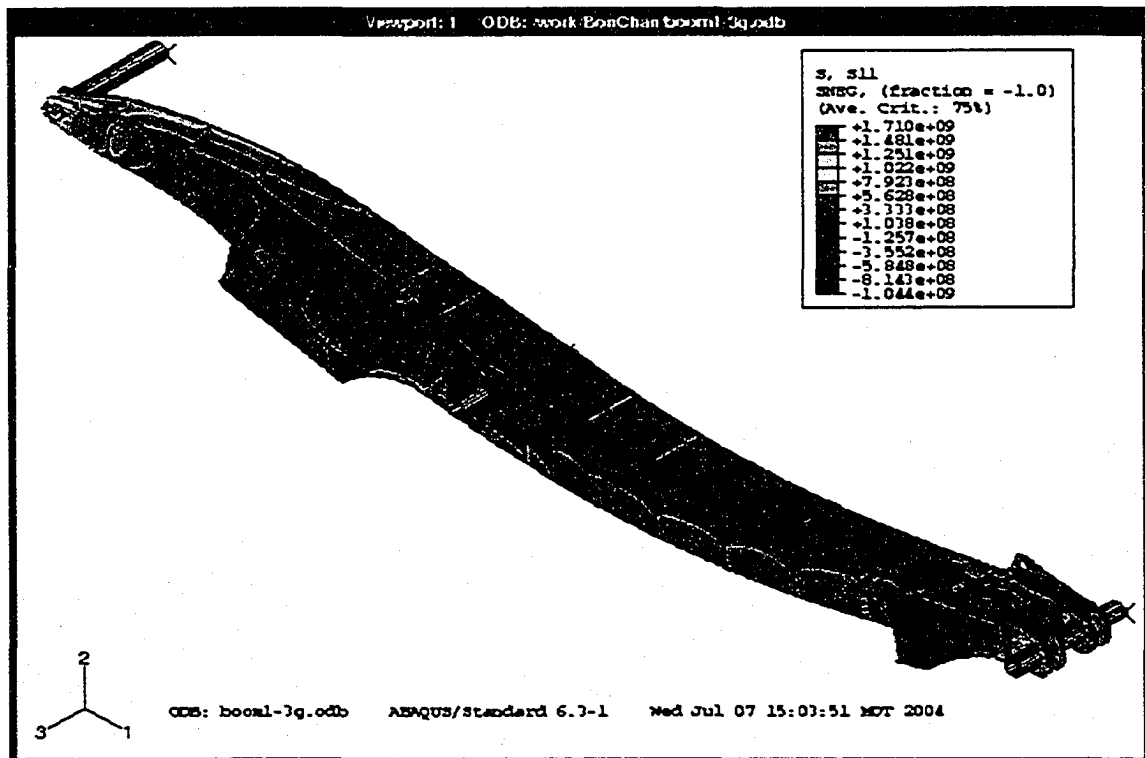
b) Axial Stresses

Figure 5-14 Stress Contour of Boom (Load Case 1 and Element Set S2)

79
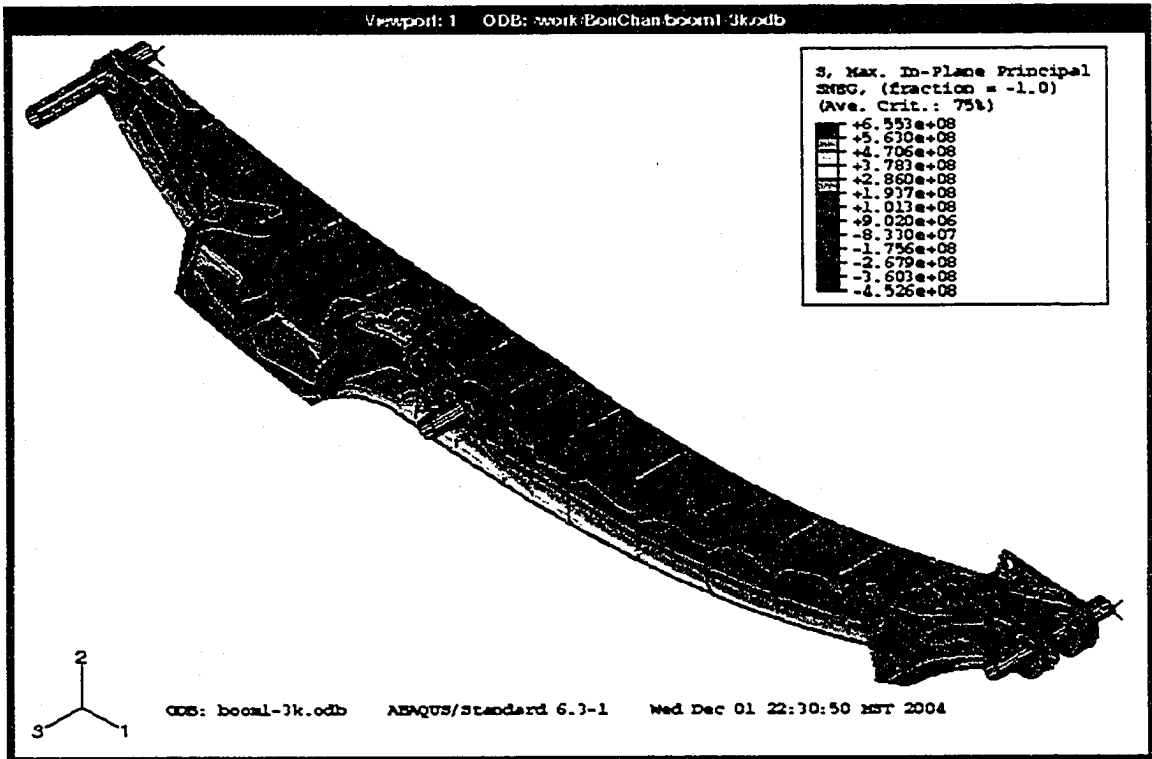
a) Maximum Principal Stresses

b) Axial Stresses

Figure 5-15 Stress Contour of Boom (Load Case 3 and Element Set S2)
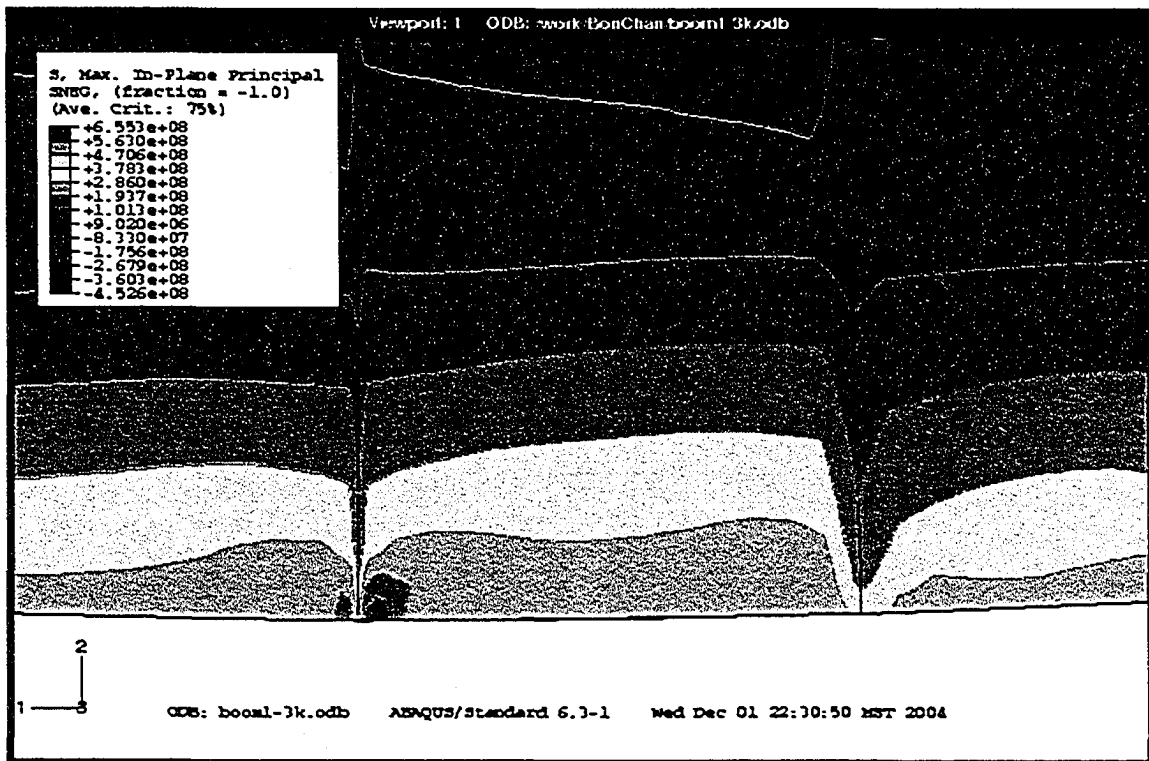
a) Maximum Principal Stresses
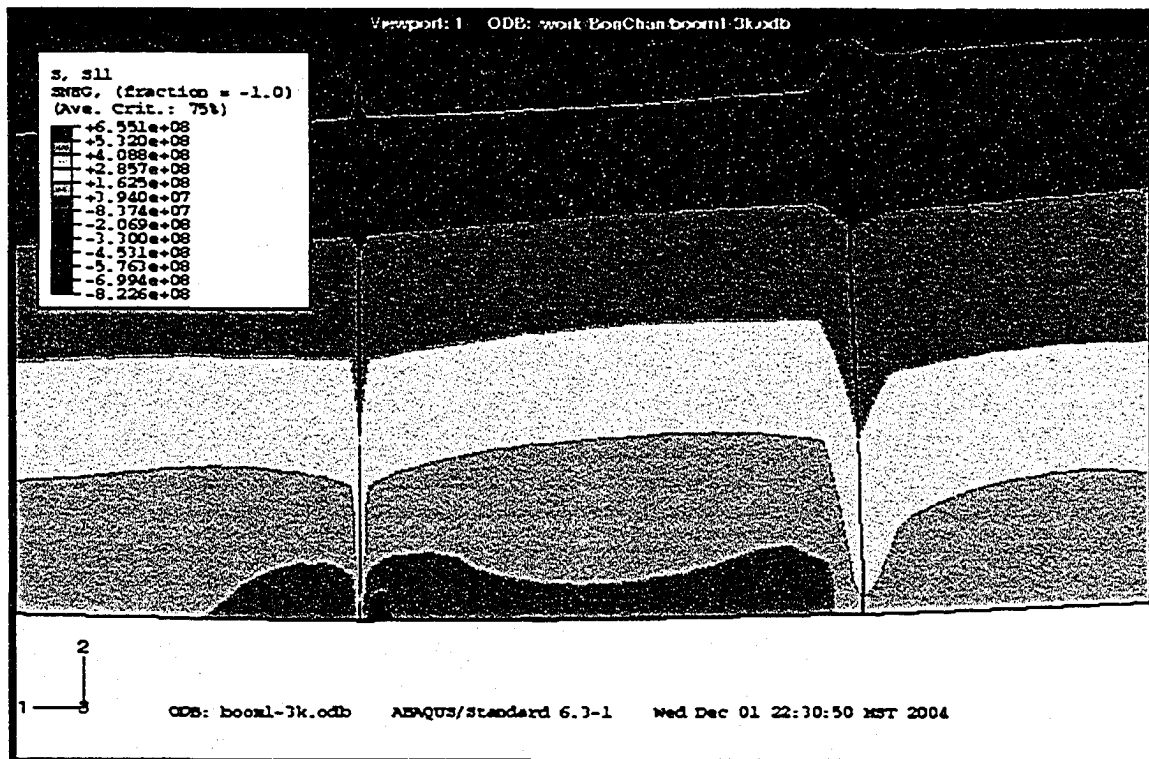
b) Axial Stresses

Figure 5-16 Stresses in the Exterior Web of Shovel Boom (Load Case 3 and Element Set S2)

81
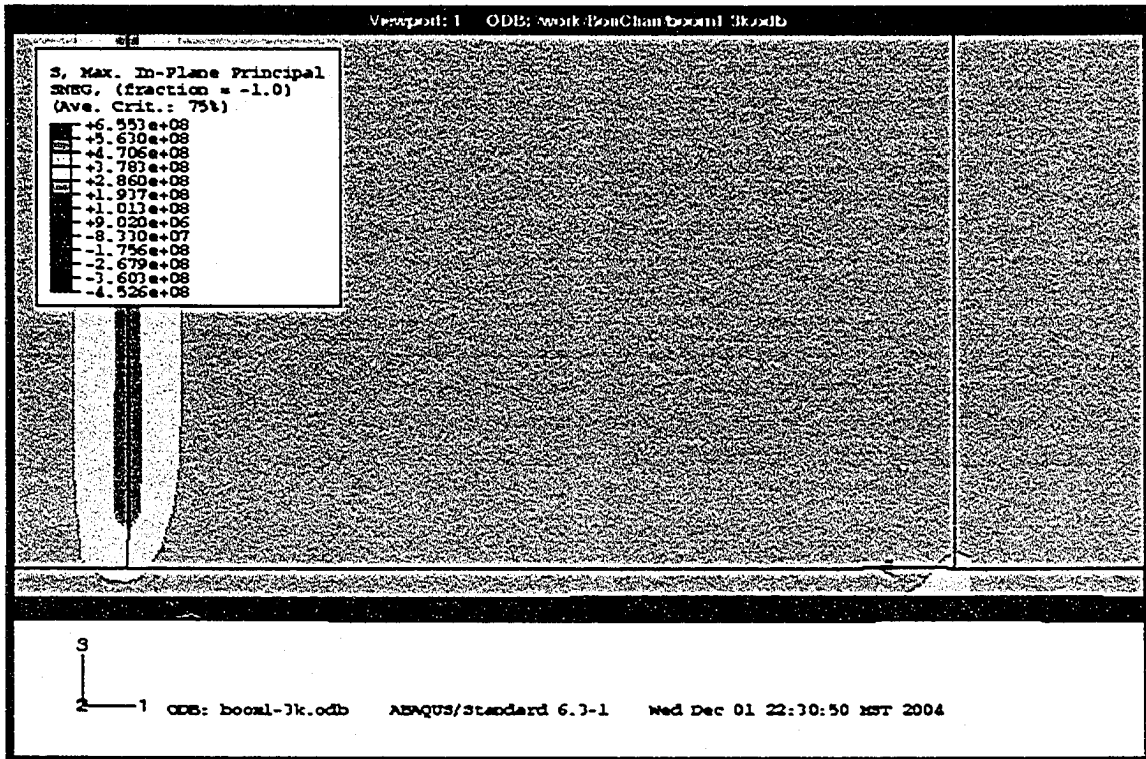
a) Maximum Principal Stresses
b)
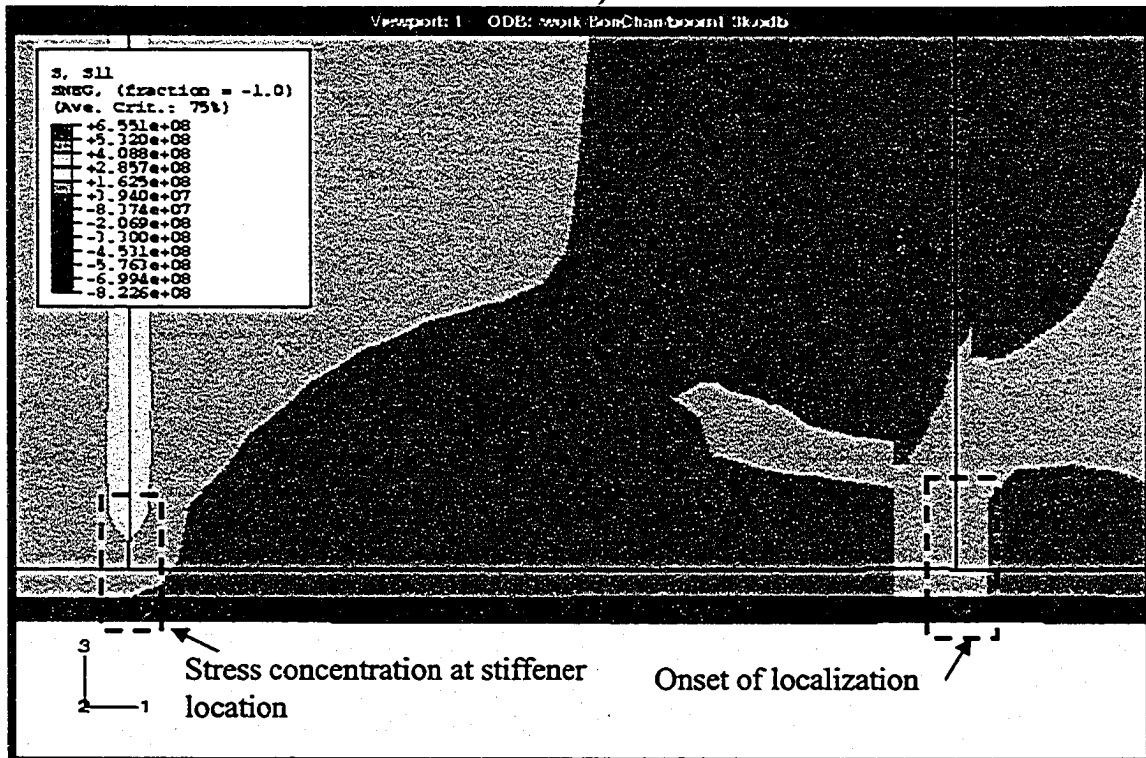
b) Axial Stresses

Figure 5-17 Stresses in the Exterior Bottom Flange of Shovel Boom (Load Case 3 and Element Set S2)

82
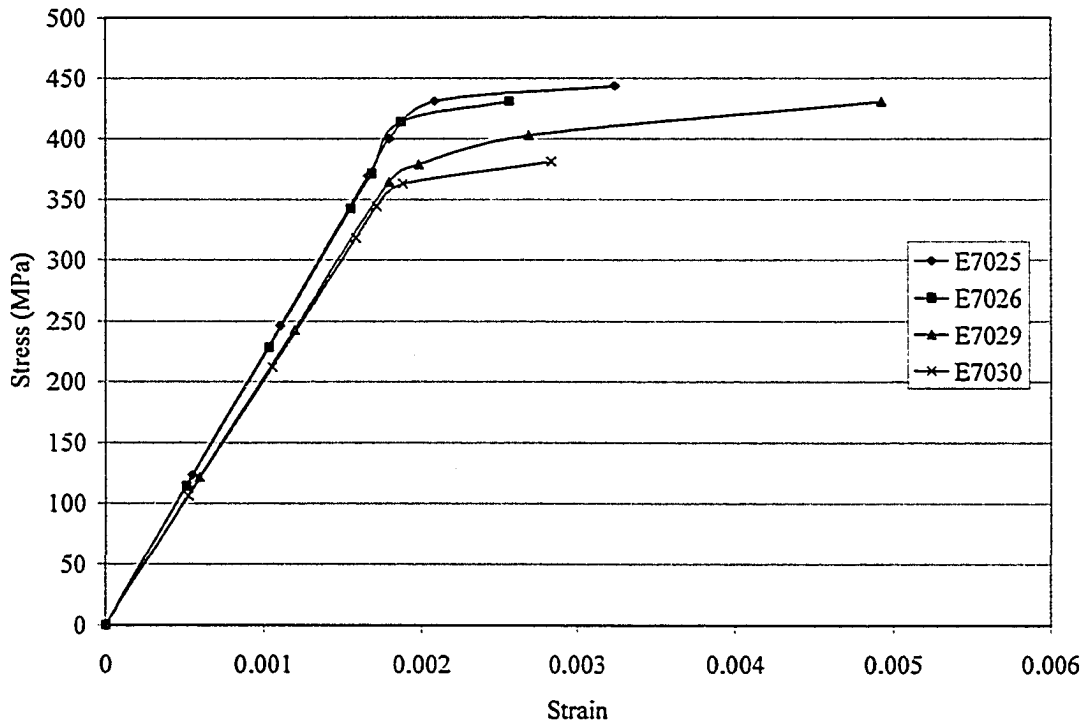
Figure 5-18 Response of Web Softening Elements at Potential Crack Location II (Load Case 1 and Element Set S1)
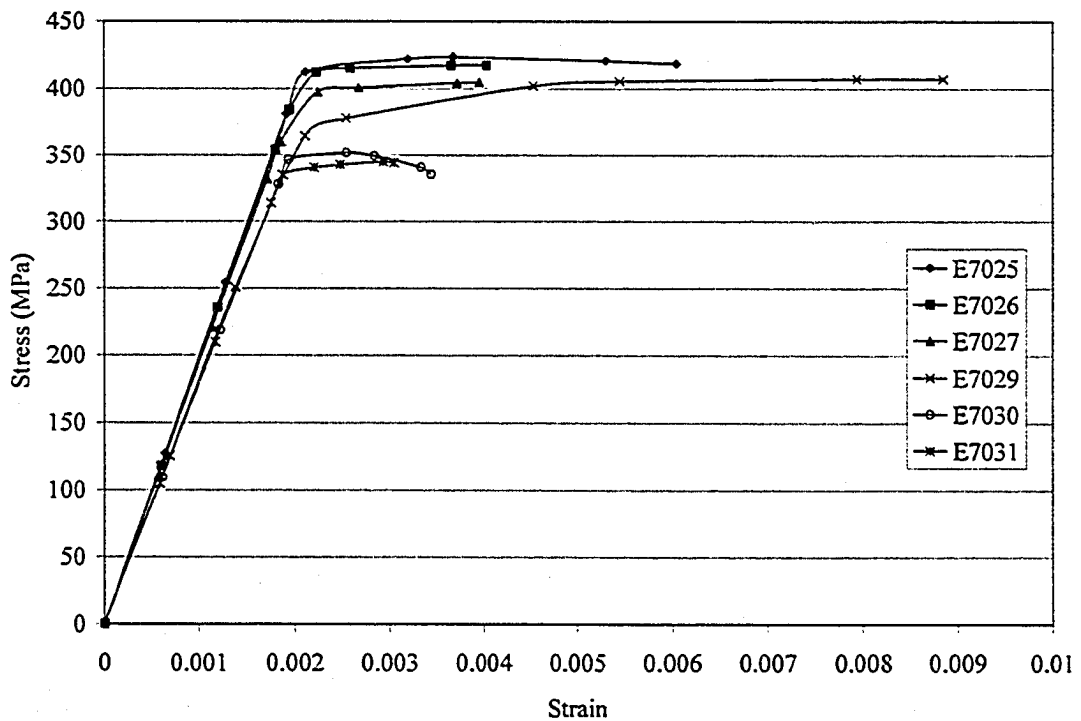
Figure 5-19 Response of Web Softening Elements at Potential Crack Location II (Load Case 1 and Element Set S2)

83
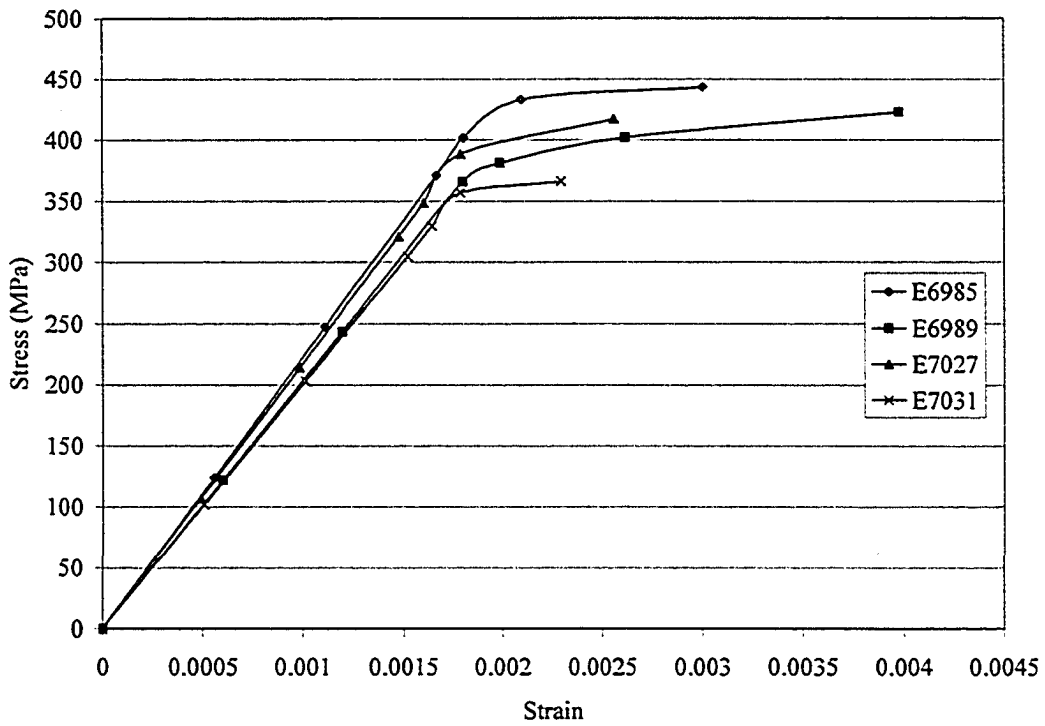
Figure 5-20 Response of Web Hardening Elements at Potential Crack Location II (Load Case 1 and Element Set S1)
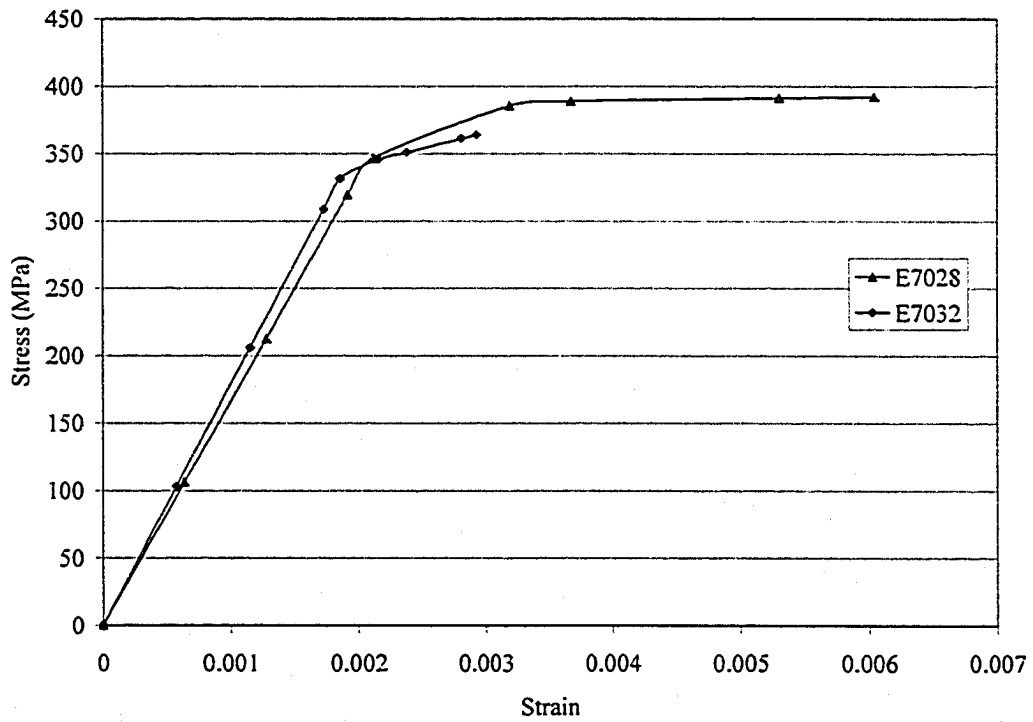
Figure 5-21 Response of Web Hardening Elements at Potential Crack Location II (Load Case 1 and Element Set S2)

84
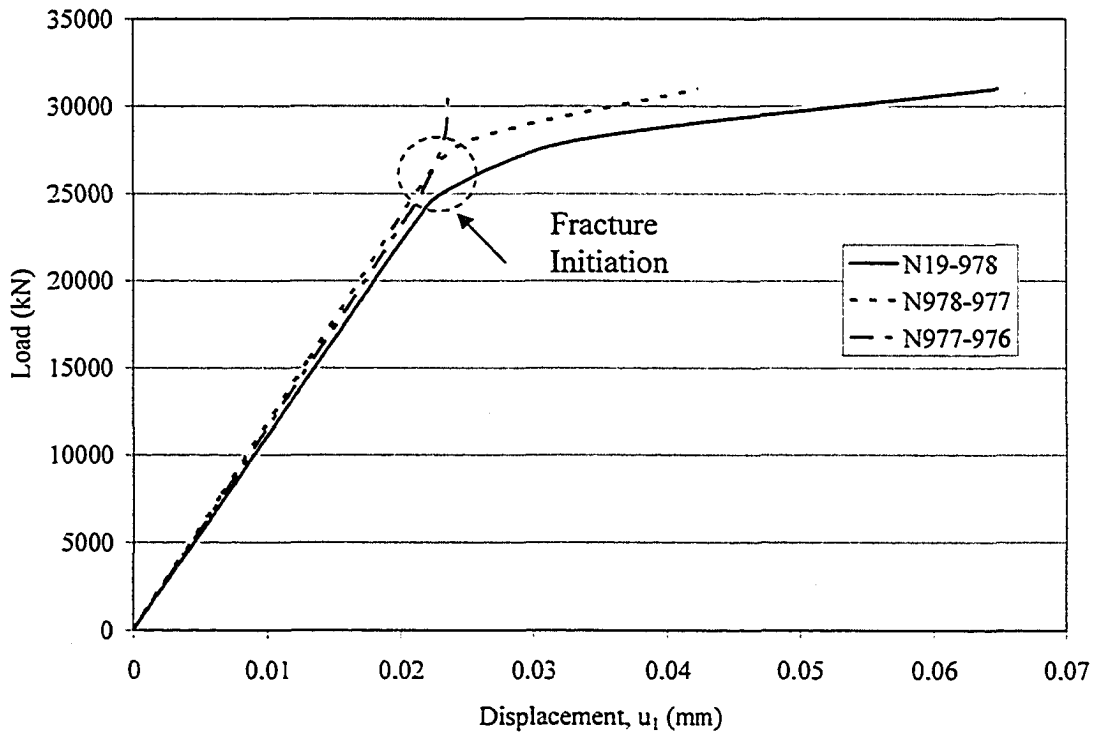
Figure 5-22 Load versus Displacement Curve of Boom (Load Case 1 and Element Set S1)
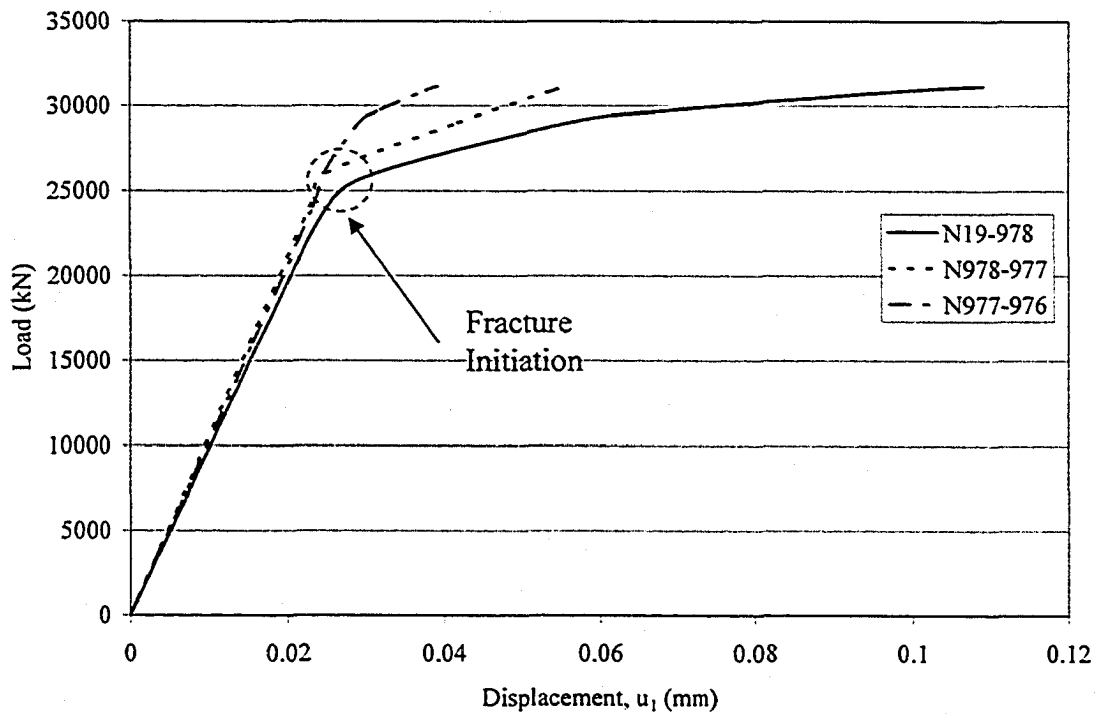
Figure 5-23 Load versus Displacement Curve of Boom (Load Case 1 and Element Set S2)

85
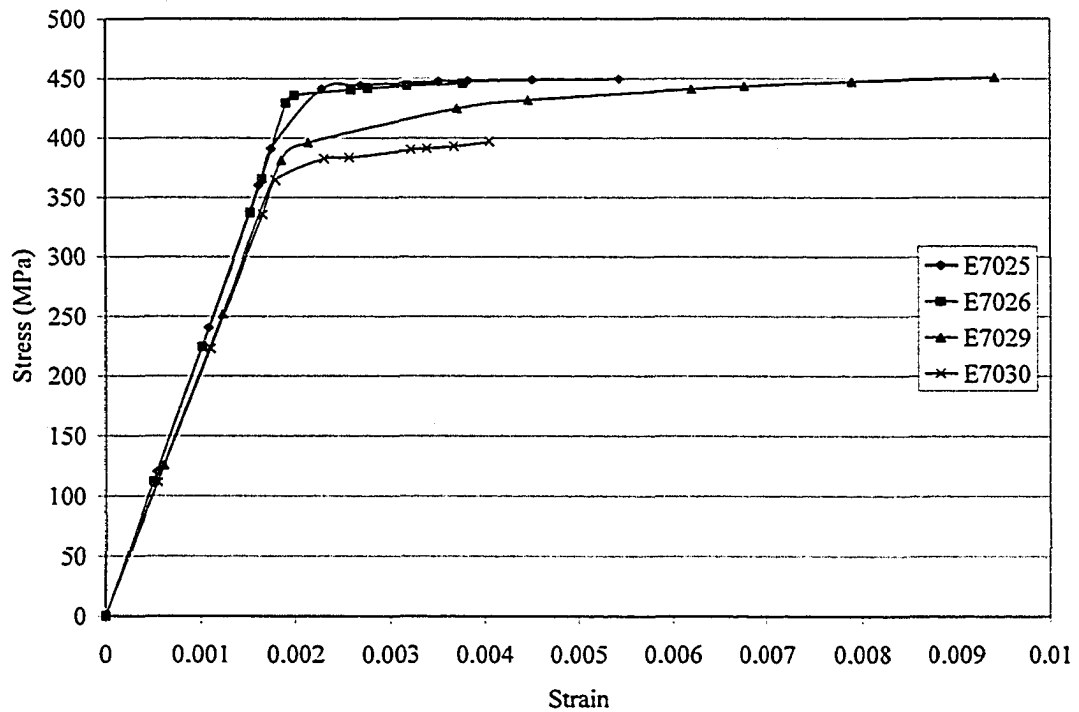
Figure 5-24 Response of Web Softening Elements at Potential Crack Location II (Load Case 3 and Element Set S1)
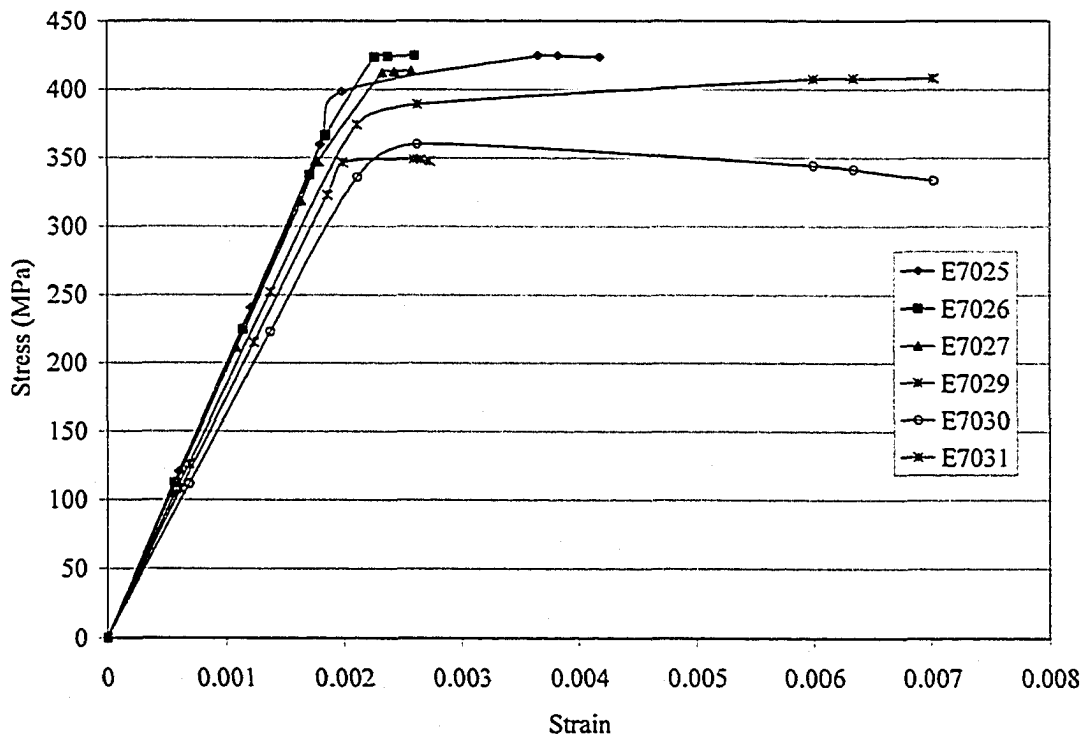
Figure 5-25 Response of Web Softening Elements at Potential Crack Location II (Load Case 3 and Element Set S2)

86
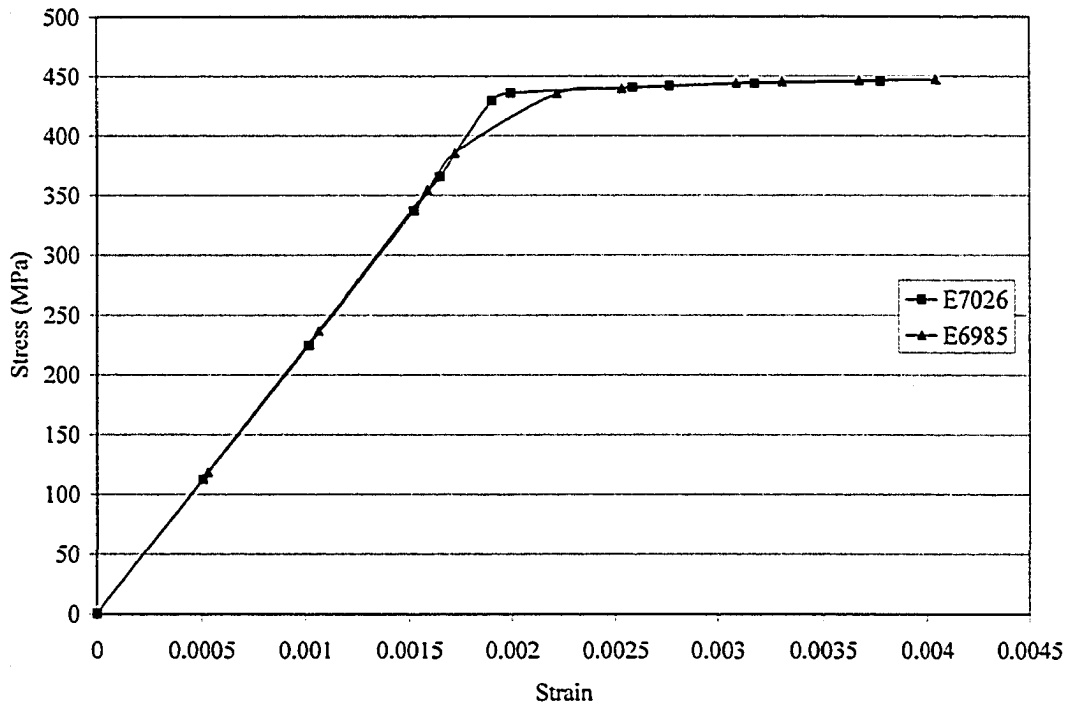
Figure 5-26 Response of Web Hardening Elements at Potential Crack Location II (Load Case 3 and Element Set S1)
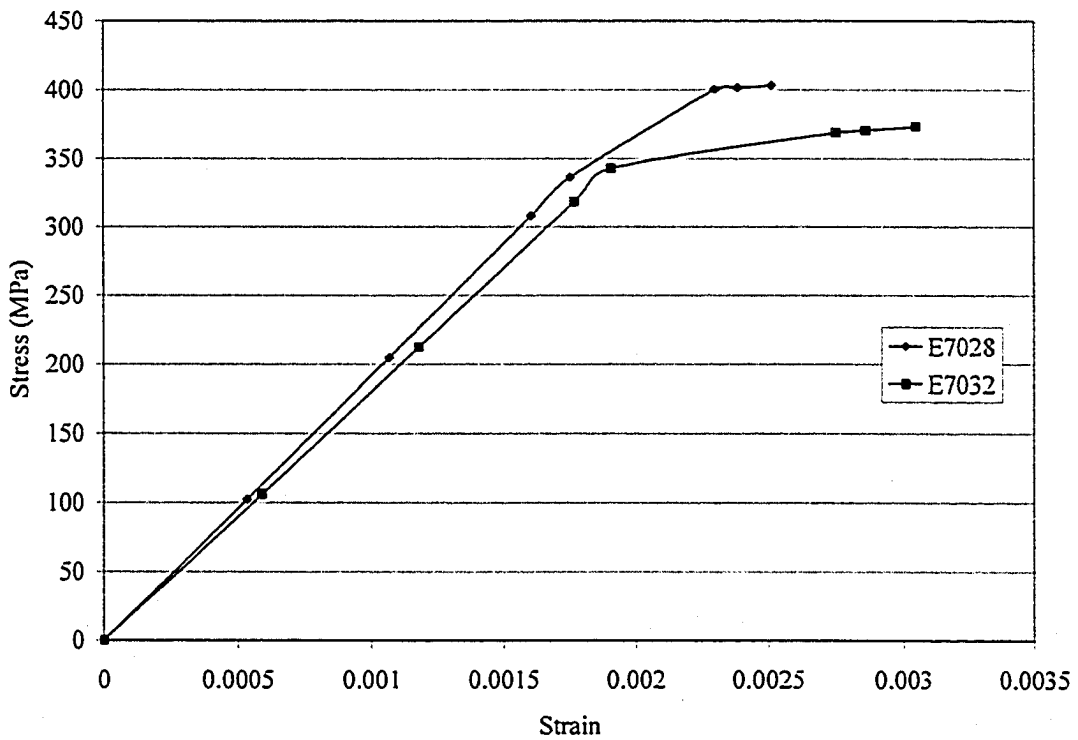
Figure 5-27 Response of Web Hardening Elements at Potential Crack Location II (Load Case 3 and Element Set S2)

87
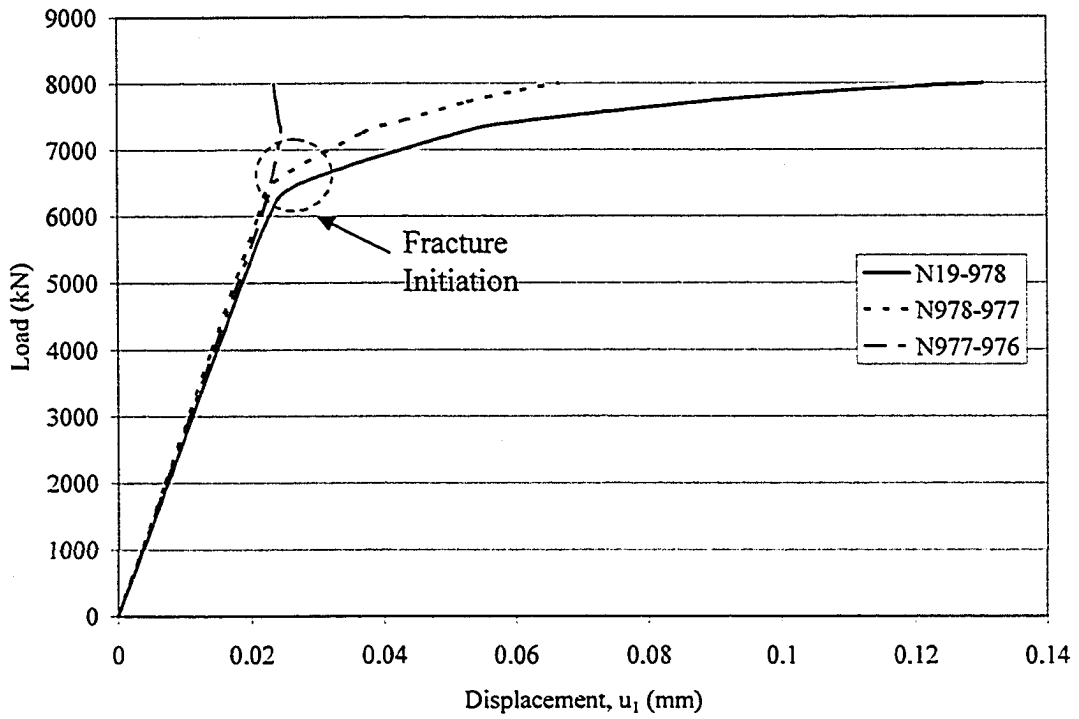
Figure 5-28 Load versus Displacement Curve of Boom at Potential Crack Location II (Load Case 3 and Element Set S1)
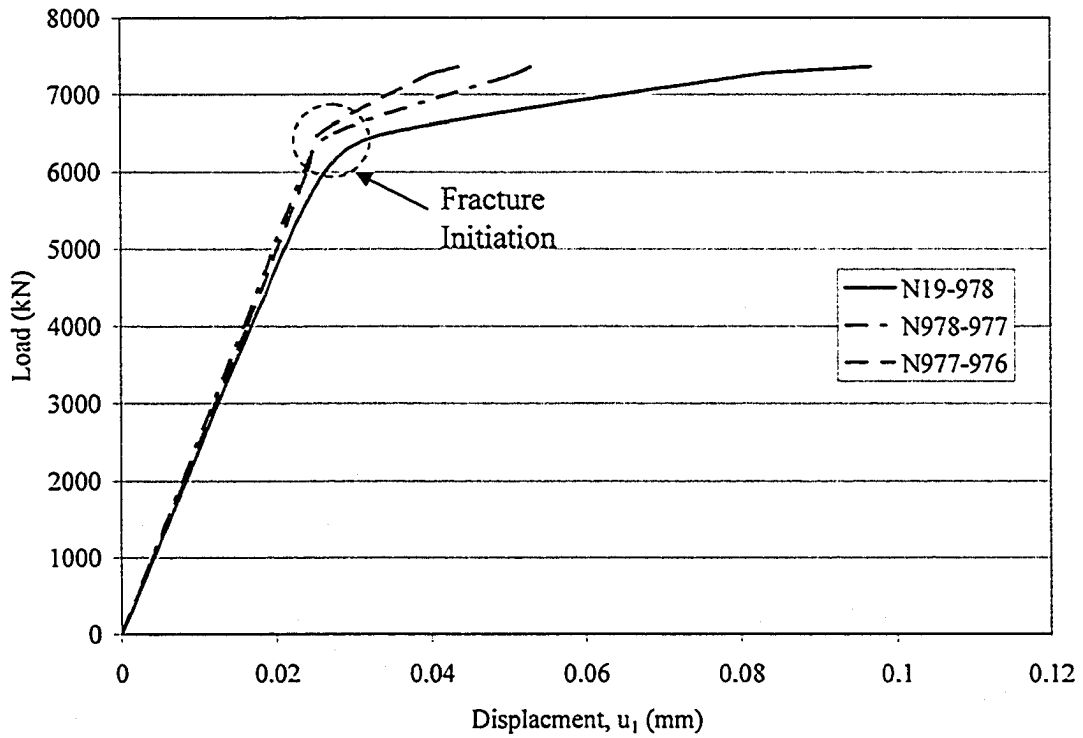
Figure 5-29 Load versus Displacement Curve of Boom at Potential Crack Location II (Load Case 3 and Element Set S2)

88

6. SUMMARY, CONCLUSIONS AND RECOMMENDATIONS

6.1   Summary

Recent developments in material fracture criteria were reviewed in Chapter 2. A variety of approaches have been proposed to model ductile fracture according to the observed physical process. In order to predict the crack initiation and propagation, several parameters including the critical damage state in a continuum damage mechanics model, the critical void volume fraction and the critical void growth rate in the void growth model, and the absorbed energy to fracture (ASPEF), were employed. Most of the abovementioned constitutive models are still under modification and extension so that the fracture behaviour of solids can be fully described.

An innovative material model is proposed based on the concept of ASPEF and the smeared crack model for the prediction of fracture in steel plate. The model consists of two submodels to deal with brittle and ductile fracture. A cracking model from the finite element program ABAQUS was modified and used to carry out the numerical analysis. Brittle fracture model is applied in this report. Brittle fracture is assumed to occur when any element in the structure reaches its peak stress, which is assumed to be the yield strength. Softening elements were introduced for the simulation of a material crack in the structure. These elements were basically governed by three parameters: the yield strength limit, the crack opening strain and the maximum shear crack opening strain. The material crack was initiated to reduce the capacity of structure when the part of the structure reached its critical capacity. The crack propagation was also simulated by softening at the Potential Crack Locations.

Brittle fracture model was selected as the reference model to carry out all the analyses in this report, which was verified and calibrated by the experimental results from tension coupon tests and fracture toughness tests afterward. Tension coupon tests were carried out to obtain the engineering stress versus engineering strain curve. Later, it was converted to true stress versus true plastic strain and used to calibrate the material

properties for numerical simulation. Four fracture toughness tests under different temperature carried out by others were used to calibrate two parameters, the crack opening strain and the maximum shear crack opening strain, required as input for the model. Load versus displacement (deflection) and load versus clip-gauge displacement curves were plotted according to the fracture toughness tests and verified with the numerical solutions.

With the application of softening elements, a good prediction on the load at fracture initiation and fracture toughness parameters could be achieved. Without any debonding between elements, these elements could reduce the capacity of the structure due to crack initiation and propagation. The application of elements was further implemented on the BE 395 shovel boom to simulate cracking on the structure. The load-displacement curves for the boom under different load cases and stress-strain curves of softening and hardening elements were plotted. The maximum principal stresses and axial stresses contours of the boom were shown as well. These contours illustrate the utilization of material crack at the potential crack location II. Loads at fracture initiation at different load scenarios were predicted and the numerical results were discussed.

6.2   Conclusions

A number of significant conclusions have been drawn based on the experimental and numerical results:

1) The proposed materiel model presented can simulate the crack initiation and propagation in terms of softening behaviour controlled by the softening elements. The numerical simulation gives a good prediction of the load-displacement (deflection) of the three-point bending specimen and the moment when fracture initiation takes place. Since no debonding between elements at the notch of bending specimen is simulated, its deformation cannot be predicted accurately.

90

Nevertheless, the constitutive model can predict the fracture initiation and reduce the capacity of structure due to the crack extension.

2) It was found that the model works better with ABAQUS/Explicit than with ABAQUS/Standard. Since the material model consists of a portion of stress-strain curve with negative slope, the convergence of numerical solutions cannot be easily achieved with ABAQUS/Standard.

3) This material model can indicate the crack initiation without any debonding between elements. The crack initiation and propagation are revealed indirectly through the changes in stress-strain relationship. To deal with the problems of fracture mechanics, the mesh allocation is no longer valid after large deformation. The approach presented in this report saves the effort of remeshing.

4) The numerical model requires the true stress versus true strain curve and the calibration of parameters crack opening strain, e_{nn}^{ck}, and maximum shear crack opening strain, ε_{max}^{ck}, in order to achieve a good prediction of fracture initiation and propagation. The crack opening strain has influence on the peak stress and the strain when the rupture occurs. Meanwhile, the maximum shear crack opening strain control the slope of the stress-strain curve of softening elements.

5) In the numerical simulations of a large shovel boom, the proposed model is able to give prediction of the load-deformation response and the instant of fracture at the desired cracking location. However, the accuracy of prediction cannot be examined due to lack of field data.

6) This material model can serve as an alternative to deal with the crack problems in steel plate without inserting any notch or initial crack by simply changing the material properties. This approach can further extend to the evaluation of connections and maintenance method.

6.3 Recommendations

1) Limited experimental results were available to verify the proposed material model. It is strongly recommended that more fracture toughness tests be conducted to

91

establish a general procedure in application of strain-softening model to simulate brittle and ductile fracture.

2) Parametric studies are required for both brittle and ductile fracture submodels. Effect of temperature and loading rate should also be taken into account for the modified model in the future.

3) Crack in the model was assumed to propagate along a straight line, which does not necessarily happen in reality. Therefore, the model should be modified in order to deal with the case of crack propagation in various orientations.

4) The proposed model cannot predict and represent the actual deformation due to the crack initiation and propagation; therefore, it is necessary to improve the deformed shape predicted by finite element program. Furthermore, the usage of the strain-softening model can possibly extend to deal with the fatigue problem.

5) The model presented in this report cannot simulate the entire loading history to rupture. It is recommended to execute the non-linear finite element analyses with ABAQUS/Explicit rather than Standard. Simulation of crack propagation was terminated soon after the fracture initiation. Even though the centre difference method employed by Explicit increases the computation time, it can simulate the whole history of structure.

6) The application of strain softening model can be extended to the generation of the microflaws on the steel plate structure. The softening model is governed by the equivalent stress on the element under cyclic loading and other factors. The fracture process will be complete with combination of the proposed material model.

LIST OF REFERENCES

ABAQUS Version 6.3 (2002). *ABAQUS/ Standard User's Manual: Volume 1, 2 and 3*, Hibbitt, Karlsson & Sorensen Inc.

ASTM (1997). *Standard Test Methods and Definitions for mechanical Testing of Steel Products, A370-97a*, American Society for Testing and Materials, Philadelphia, PA.

ASTM (1999). *Standard Test Methods for Measurement of Fracture Toughness, E1820-99a*, American Society for Testing and Materials, West Conshohocken, PA.

Barenblatt, G. I. (1962). *The Mathematical Theory of Equilibrium of Cracks in Brittle Fracture*, Advances in Applied Mechanics, Vol. 7, pp. 55-129.

Bažant, Z. P. & Planas, J. (1998). *Fracture and Size Effect in Concrete and other Quasibrittle Materials*, CRC Press, Boca Raton, FL.

Chaouadi, R., de Meester, P. & Vandermeulen, W. (1994). *Damage Work as Ductile Fracture Criterion*, International Journal of Fracture, Vol. 66, pp. 155-164.

Czoboly, E., Havas, I. and Gillemot, F. (1980). *The Absorbed Specific Energy Till Fracture as a Measure of the Toughness of Metals*, Proceedings of an International Symposium on Absorbed Specific Energy and/or Strain Energy Density Criterion, (Edited by G.C. Sih, E. Czoboly and Gillemot, F.), Budapest, Hungary, Martinus Nijhoff Publishers, pp. 107-129.

DeGiorgi, V. G., Kirby, G. C. III & Jolles, M. I. (1989). *Prediction of Classical Fracture Initiation Toughness*, Engineering Fracture Mechanics, Vol. 33, No. 5, pp. 773-785.

Dodd, B. and Bai, Y.L. (1987). *Ductile Fracture and Ductility – with Application to Metalworking*, Academic Press, London.

Dugdale, D. S. (1960). *Yielding of Steel Sheets Containing Slits*, Journal of the Mechanics and Physics of Solids, Vol. 8, pp. 100-108.

Elfgren, L. (1989). *Fracture Mechanics of Concrete Structures – from theory to applications*. Chapman and Hall Ltd., New York.

Gillemot, L.F. (1976). *Criterion of Crack Initiation and Spreading*, Engineering Fracture Mechanics, Vol. 8, pp. 239-253.

Hillerborg, A. (1983). *Analysis of One Single Crack*, Fracture Mechanics of Concrete (Edited by F. H. Wittmann). Amsterdam: Elsevier Science, pp. 223-49.

Kachanov, L. M. (1986). *Introduction to Continuum Damage Mechanics*, Matrinus Nihjoff Publishers, Dordrecht.

Khoo, H. A., Cheng, J.J.R. & Hrudey, T.M. (2000). *Ductile Fracture of Steel*, Structural Engineering Report No. 232. University of Alberta.

Lemaitre, J. (1985). *A Continuous Damage Mechanics Model for Ductile Fracture*, Journal of Engineering Materials and Technology, Vol. 107, pp. 83- 89.

Matic, P. (1985). *Numerically Predicting Ductile Material Bahavior from Tensile Specimen Response*, Theoretical and Applied Fracture Mechanics, Volume 4, pp. 13-28.

Matic, P., Kirby III, G. C. & Jolles, M. I. (1987). *The Relationship of Tensile Specimen Size and Geometry Effects to Unique Constitutive Parameters for Ductile Materials*, NRL Memorandum Report 5936. Naval Research Laboratory.

Matic, P. & Jolles, M. I. (1989). *Defect, Constitutive Behavior, and Continuum Toughness Considerations for Weld Integrity Analysis*, Nonlinear Fracture Mechanics: Volume II - Elastic Plastic Fracture, ASTM STP995, pp. 82-92.

McClintock, F. A. & Argon, A. S. (1966). *Mechanical Behaviour of Materials*, Addison-Wesley Publishing Company, Inc., New York.

Rashid, Y. R. (1968). *Analysis of Prestressed Concrete Pressure Vessels*, Nuclear Engineering Des., Volume 7, No. 4, pp. 334-355.

Rice, J. R. (1976). *Elastic-Plastic Fracture Mechanics*, The Mechanics of Fracture presented at ASME winter annual meeting, New York, N.Y., December 5-10, 1976. (Edited by F. Erdogen). New York: The American Society of Mechanical Engineers.

Rolfe, S. T. & Barsom, J . M. (1977). *Fracture and Fatigue Control in Structures – application of fracture mechanics*, Prentice Hall Inc., Englewood Cliffs, New Jersey.

Schindler, H. J. (2001). *Strain energy density as the link between global and local approach to fracture*, Proceeding of 10th International Conference on Fracture, Honolulu, Edited K. Ravi-Chandar, et al., Pergamon, 2001 (on CD).

Shah, S. P. & John, R. (1986). Strain Rate Effects on Mode I Crack Propagation in Concrete. Fracture Mechanics and Fracture Energy of Concrete (Edited by F. H. Wittmann). Amsterdam: Elsevier Science, pp. 453-465.

Sih, G. C. & Ditommaso, A. (1985). *Fracture Mechanics of Concrete*. Martinus Nijhoff Publishers, Dordrecht, Netherlands.

Sluys, L. J. (1998). *Computational Modelling of Localisation and Fracture, Localization and Fracture Phenomena in Inelastic Solids - CISM Courses and Lecture No. 386*. International Centre for Mechanical Sciences. (Edited by Piotr Perzyna), pp. 244- 299.

Yin, Y., Grondin, G. Y., Elwi, A. E. & Obaia, K. H. (2004). *Fatigue Crack Management in Heavy Mining Equipment*, Final Research Report submitted to Syncrude Canada Limited, August, 79 pp.

Zheng, C. Q., Zhou, L. & Liu, J. M. (1986). *Fracture Behaviour of Ductile Steels under Triaxial Stress*. The proceedings of the 9th Congress on Material Testing, Budapest, 29 September - 3 October, 1986 (Edited by Czoboly.) Budapest: GTE (Gépipari Tudományos Egyesület), pp. 86-91.

APPENDIX A

ABAQUS FILE FOR NOTCH BEAM

96

APPENDIX A – ABAQUS FILE FOR NOTCH BEAM

```
*HEADING
 2d CPS4R Beam. Three-points bending test with Notched Specimen.
(07May04)
 S.I. Units (minimetres, Newtons, sec, tonnes, MPa, mJ)
**
** Nodal coordinates
**
*NODE
 1, 0.0, 0.0
 2, 0.0, 4.0
 .........
 .........
 3333, 186.5, 73.0
 3334, 186.5, 74.5
** NODES OF SUPPORTS AND LOADS
*NSET, NSET=SUPP
 201, 4901
*NSET, NSET=CGD
 2501, 2601
**
** Element connectivity
**
*ELEMENT, TYPE=CPS4R, ELSET=PLATEA
 1, 1, 101, 102, 2
*ELGEN, ELSET=PLATEA
 1, 17, 1, 1, 17, 100, 100
*ELEMENT, TYPE=CPS4R, ELSET=PLATEB
 3201, 3401, 3501, 3502, 3402
*ELGEN, ELSET=PLATEB
 3201, 17, 1, 1, 17, 100, 100
*ELEMENT, TYPE=CPS4R, ELSET=PLATEA
 1801, 1701, 1801, 1802, 1702
 1802, 1901, 1902, 1801, 1701
 .........
 .........
 2002, 1951, 2185, 2186, 1952
*ELEMENT, TYPE=CPS4R, ELSET=PPLATEA
 2101, 2101, 2301, 2302, 2102
 2102, 2102, 2302, 2303, 2103
 .........
 .........
 2189, 2185, 2387, 2388, 2186
*ELEMENT, TYPE=CPS4R, ELSET=PPLATE1
 2201, 2202, 2321, 2322, 2203
 2202, 2203, 2322, 2323, 2204
 .........
 .........
 2751, 2871, 2952, 2953, 2872
*ELEMENT, TYPE=CPS4R, ELSET=PPLATEB
 2801, 2801, 3001, 3002, 2802
 2802, 2802, 3002, 3003, 2803
 .........
 .........
```

97

```
 2889, 2887, 3085, 3086, 2888
*ELEMENT, TYPE=CPS4R, ELSET=PLATEB
 2901, 3001, 3201, 3202, 3002
 2902, 3002, 3202, 3203, 3003

 ........

 ........
 3168, 3251, 3334, 3418, 3252
*ELSET, ELSET=EPLATE
 PLATEA, PLATEB
*ELSET, ELSET=PPLATE2
 PPLATEA, PPLATEB
*ELSET, ELSET=EL-MID
 PPLATE1, PPLATE2
*ELSET, ELSET=ALLPLATE
 EPLATE, EL-MID
**
************** END OF MESH GENERATION COMMANDS ******************
**
** Physical and material properties
**
*SOLID SECTION, ELSET=EPLATE, MATERIAL=MAT1
 38.1
*MATERIAL, NAME=MAT1
*ELASTIC, TYPE=ISOTROPIC
 186300, 0.3
*DENSITY
 7.85E-9
*SOLID SECTION, ELSET=PPLATE1, MATERIAL=MAT2
 38.1
*MATERIAL, NAME=MAT2
*ELASTIC
 186300, 0.3
*DENSITY
 7.85E-9
*BRITTLE CRACKING
 386.5, 0.0
 10.0, 0.170
 1.0, 1.000
*BRITTLE SHEAR, TYPE=POWER LAW
 0.05, 1
*SOLID SECTION, ELSET=PPLATE2, MATERIAL=MAT3
 38.1
*MATERIAL, NAME=MAT3
*ELASTIC
 186300, 0.3
*DENSITY
 7.85E-9
*PLASTIC
  386.5, 0.00000
  418.6, 0.02575
  445.1, 0.03369
  473.0, 0.04442
  508.0, 0.06259
  541.4, 0.09103
  578.9, 0.14117
 1114.6, 1.00000
**
```

98

```
******************************************
** Loading nodes
**
*NSET, NSET=ALLNODES, ELSET=ALLPLATE
*AMPLITUDE, NAME=RAMP-L
 0.0, 0.0, 4.0, 1.0
**
** Boundary Conditions
**
*BOUNDARY
 201, 2, 2, 0.0
 4901, 2, 2, 0.0
 2587, 1, 1, 0.0
**
** History data -- End of Model data --
**
*STEP, NLGEOM=YES
 STEP 1 - Concentrated load in the midspan
*DYNAMIC, EXPLICIT
 ,4.0
**
*FIXED MASS SCALING, FACTOR=17500
*FIXED MASS SCALING, FACTOR=35000, ELSET=EL-MID
**
*BOUNDARY, TYPE=VELOCITY, AMPLITUDE=RAMP-L
 2587, 2, 2, -1.0
** Output Requests
**
*OUTPUT, FIELD, NUMBER INTERVALS=20
*NODE OUTPUT, NSET=SUPP
 RF
*NODE OUTPUT, NSET=CGD
 U
*OUTPUT, FIELD, NUMBER INTERVALS=20
*ELEMENT OUTPUT, ELSET=PPLATE1
 S, LE
*ELEMENT OUTPUT, ELSET=PPLATE2
 S, LE
*RESTART, WRITE
*END STEP
```